

EXPERIMENTAL AND THEORETICAL STUDIES ON WATER

by

CHUL HEE CHO, B.S., M.S.

A DISSERTATION

IN

CHEMISTRY

Submitted to the Graduate Faculty  
of Texas Tech University in  
Partial Fulfillment of  
the Requirements for  
the Degree of

DOCTOR OF PHILOSOPHY

Approved

Accepted

May, 1997

"  
391  
T3  
1997  
No. 48  
C.2

AKT3478

## ACKNOWLEDGEMENTS

I cannot express my thank with any word to Professor G. Wilse Robinson for his patient guidance and encouragement during my doctoral program. I am also greatly indebted to him for considerable supports financially and mentally. As my mentor, he has given me an inspiration and a new insight of the study of the water problem.

I want to give my deepest appreciation to Dr. Surjit Singh for his tremendous help and advise during the program. His instruction for any subject has always given me spiritual support and a sense of the adventure for science.

I would like to acknowledge Professor Edward L. Quitevis, Professor Richard L. Redington, Professor Richard E. Wilde and Professor Allan D. Headley for their many valuable comments, guidance, and encouragement throughout the program.

I wish to express my thanks to colleagues, Dr. Mary S. Vedamuthu and Mr. Jacob Urquidi for their help and cooperation I have received. I also appreciate my former colleagues, Dr. Ningyi Luo and Mr. J.-B. Zhu particularly for their help with the laser experiment.

I am especially indebted to my parents, brothers, sisters, and friends for their steady love and continued support which led to the completion of my school years. I dedicate this dissertation to my loving wife, Seounghee Rhee, and our children, Wilse Kyuhyoung and Robin Kwanghyoung. Without their endless love, patience and understanding, I would never have been able to complete this study.

## TABLE OF CONTENTS

ACKNOWLEDGMENTS .....	ii
ABSTRACT .....	vii
LIST OF TABLES .....	ix
LIST OF FIGURES .....	x
CHAPTER	
I. INTRODUCTION .....	1
1.1 Experimental Studies on Interfacial Water .....	2
1.1.1 Importance of Liquid Water in Biological Systems .....	2
1.1.2 Interfacial Water .....	4
1.1.3 Reverse Micelle .....	7
1.1.4 Fluorescent Probe Molecules .....	12
1.1.5 Contents of Present Work .....	17
1.2 Computer Simulation of Liquid Water .....	19
PART I. STUDIES OF THE PROPERTIES OF LIQUID WATER IN REVERSE MICELLES USING AN ULTRAFAST LASER .....	26
II. SINGLE PHOTON COUNTING LIFETIME MEASUREMENT .....	27
2.1 Introduction .....	27
2.2 TCSPC System .....	28
2.2.1 The Excitation Source .....	30
2.2.2 Photon Detectors .....	34

2.2.3	Timing Electronics and Data Acquisition	-----37
2.3	Analysis Method of TCSPC Decay Data	-----43
III.	EXPERIMENTAL STUDIES OF THE PROPERTIES OF AN INTERFACIAL WATER	-----47
3.1	Experimental Materials	-----48
3.2	Preparation of Reverse Micelle Solution	-----49
3.3	Results	-----50
3.3.1	Decay Profiles from the ANS(II) Molecules	-----55
3.3.2	Decay Profiles from the ANS(I) Molecules	-----60
3.4	Discussion	-----68
IV.	ANALYTICAL METHOD FOR INTERPRETING THE PROPERTIES OF AN INTERFACIAL WATER	-----72
4.1	Reverse Micelle Structure	-----73
4.2	Probability Kinetics	-----78
4.3	Fitting Procedures	-----83
4.4	Results	-----86
4.5	Discussion	-----95
V.	CONCLUSIONS	-----98
PART II.	NOVEL POTENTIAL FUNCTIONS OF WATER FOR COMPUTER SIMULATIONS	----- 101
VI.	ONE-DIMENSIONAL FLUID MODEL	----- 102
6.1	Takahashi Model	----- 103
6.2	Simple Potential Functions	----- 107

6.3 The Double Well Potential Function-----	110
VII. THREE-DIMENSIONAL POTENTIAL FOR WATER-----	117
7.1 The New Potential Function of Water-----	118
7.2 The NVE MD Simulation -----	135
7.2.1 Equations of Motion -----	136
7.2.2 The Gear Predictor-Corrector Algorithm-----	139
7.2.3 The Initial Conditions-----	141
7.2.4 Thermodynamic Quantities of Interest-----	142
7.3 Results and Discussion -----	144
REFERENCES -----	149

## ABSTRACT

The properties of water near surfaces or in confined volumes are not well understood. Here, the biologically relevant system chosen for studying the behavior of water near a surface is composed of small water pools encapsulated within sodium bis (2-ethylhexyl) sulfosuccinate (AOT) reverse micelles (RM's), whose surfaces are highly hydrophilic. The time-correlated single-photon counting technique together with an ultrafast laser system was employed to measure the fluorescence lifetimes of the probe molecule ANS within various RM sizes. The resulting decay data were interpreted by using the analytical method and the non-linear least squares fitting technique in order to seek a relationship between diffusion of the probe and a fast nonradiative event. By discovering these trends, information about water properties within different regions of the aqueous core of the RM can be obtained as a function of distance from a surface. The ability of the probe to undergo the fast nonradiative process depends on a reorientational relaxation time of the water solvent, which may become orders of magnitude slower for water near a surface. Perturbations on the translational velocity autocorrelation function of the probe, as measured by the diffusion fluxes, are very large, extending nearly to the center of the largest RM studied (radius  $\sim 55$  Å). On the other hand, perturbations on the orientation relaxation of the solvent, as measured by the probe lifetimes, were found to extend no more than  $\sim 10-15$  Å from the surface of any of the RM's studied.

An explanation of the density maximum in water near  $4$  °C can be described in terms of a dense second-neighbor structure obtained from the bending of hydrogen bonds.

The analytical and computational models of water, which provide an explanation of this anomaly, are proposed. In these models, the water-water potential is altered to include more realistic interactions in the second-neighbor shell. Support for this idea is provided here by considering the exactly soluble one-dimensional Takahashi fluid model and then by an NVE molecular dynamics simulation for a realistic water model.

## LIST OF TABLES

1.1. Acid Fluorescent Probe Molecules and Their Diffusion Constants in Pure Water ---	14
3.1. Absorption and Emission Maxima, Quantum Yields, Lifetimes, and Radiative and Nonradiative Rates of 1,8-ANS at 25 °C -----	52
3.2. Single Exponential Fitting Parameter for Emission at 560 nm, Attributed to the ANS(II) -----	61
3.3. Double Exponential Fitting Parameters for Emission at 460 nm, Attributed to the ANS(I) -----	61
4.1. Some Physical Properties of the Reverse Micelles Used in This Work -----	77
4.2. Diffusion and Lifetime Parameters Employed for the Analysis -----	87
7.1. The Parameters of the GWR Potential for Liquid Water -----	122

## LIST OF FIGURES

1.1. The chemical structure and the symbolic representative of an AOT molecule -----	8
1.2. The schematic view of reverse micelle structure formed by water and AOT in heptane solution -----	10
2.1. Block diagram of apparatus for the measurement of lifetime -----	29
2.2. Schematic representation of the dumping pulse train of the dye laser output to excite a sample -----	33
2.3. Schematic timing diagram showing the function of TAC -----	40
3.1. The absorption spectrum of ANS in pure water at 25 °C -----	51
3.2. Fluorescence decay profile with single exponential fit, attributed to the ANS(II) in pure water -----	54
3.3. Fluorescence decay profile with single exponential fit, attributed to the ANS(II) for $w_0 = 4.1$ at 560 nm -----	56
3.4. Fluorescence decay profile with single exponential fit, attributed to the ANS(II) for $w_0 = 8.2$ at 560 nm -----	57
3.5. Fluorescence decay profile with single exponential fit, attributed to the ANS(II) for $w_0 = 16.4$ at 560 nm -----	58
3.6. Fluorescence decay profile with single exponential fit, attributed to the ANS(II) for $w_0 = 32.9$ at 560 nm -----	59
3.7. Fluorescence decay profile with double exponential fit, attributed to the ANS(I) for $w_0 = 4.1$ at 460 nm -----	63
3.8. Fluorescence decay profile with double exponential fit, attributed to the ANS(I) for $w_0 = 8.2$ at 460 nm -----	64
3.9. Fluorescence decay profile with double exponential fit, attributed to the ANS(I) for $w_0 = 16.4$ at 460 nm -----	65
3.10. Fluorescence decay profile with double exponential fit, attributed to the ANS(I) for $w_0 = 32.9$ at 460 nm -----	66

4.1. Schematic cross-sectional diagram of the reverse micelle of AOT	75
4.2. The theoretical fit to the experimental decay profile for $r_w = 10.0 \text{ \AA}$ RM	88
4.3. The theoretical fit to the experimental decay profile for $r_w = 16.5 \text{ \AA}$ RM	89
4.4. The theoretical fit to the experimental decay profile for $r_w = 29.5 \text{ \AA}$ RM	90
4.5. The theoretical fit to the experimental decay profile for $r_w = 55.2 \text{ \AA}$ RM	91
4.6. Diffusion relationships of ANS(I) for the various reverse micelle sizes	93
4.7. Lifetime relationships of ANS(I) for the various reverse micelle sizes	94
6.1. The reduced density $\rho^*$ as a function of reduced temperature $T^*$ for $\lambda = 10$ and $P^* = 10$ for the 1-D double well potential model	115
6.2. The variation of densities with respect to temperature at various pressures	116
7.1. The coordinate system used to the water dimer interaction	120
7.2. The comparison of the GWR potential with the SPC/E potential	123
7.3. The angular dependent potentials of water molecule 1 and 2 rotated around x-axis at $2.8 \text{ \AA}$	125
7.4. The angular dependent potentials of water molecule 1 or 2 rotated around y-axis at $2.8 \text{ \AA}$	126
7.5. The angular dependent potentials of water molecule 1 rotated around z-axis at $2.8 \text{ \AA}$	127
7.6. The angular dependent potentials of water molecule 2 rotated around z-axis at $2.8 \text{ \AA}$	128
7.7. The angular dependent potentials of water molecule 1 rotated around x-axis at $3.8 \text{ \AA}$	129
7.8. The angular dependent potentials of water molecule 2 rotated around x-axis at $3.8 \text{ \AA}$	130
7.9. The angular dependent potentials of water molecule 1 or 2 rotated around	

y-axis at 3.8 Å -----	131
7.10. The angular dependent potentials of water molecule 1 rotated around z-axis at 3.8 Å -----	132
7.11. The angular dependent potentials of water molecule 2 rotated around z-axis at 3.8 Å -----	133
7.12. The radial distribution functions of liquid water at 298 K -----	146
7.13. The pressure variation as a function of temperature -----	147

# CHAPTER I

## INTRODUCTION

Water is undoubtedly the most abundant and the most extensively discussed of all chemical compounds on our planet. It is said to be the only inorganic liquid which occurs naturally on earth and the only chemical compound that possess all three physical states, e.g., solid, liquid, and vapor, in its natural state [1]. It transforms readily from the liquid state to the solid and gaseous. This aspect of water has always attracted philosophical interest from the ancient times, let alone the modern scientific interest. Water, it seems safe to say, is virtually the basis of everything, including life itself.

One should not underestimate the importance of water for sustaining life on earth. From a physicochemical point of view, water is an efficient and a universal solvent, that behaves in a manner far from what we call normal, because of its high dielectric constant and very strong solvating power [1,2]. Moreover, the properties of liquid water as a solvent have potent effects over the many biochemical and physiological processes that are involved in the sustenance and perpetuation of living organisms. The significance of water and its peculiar properties has generated a constant and persistent interest in the study of this substance [3].

We have gained a thorough knowledge of most properties of pure-state water, but we know little about the properties of water which interacts with other chemical or biological substances. The water contained in cells and at biological membranes cannot be treated as the same water we use so generously everyday [4]. It has been difficult to

unravel the microscopic properties of water near biological environments, such as a protein surface, by direct experiments. During the past decades, the properties of water near surfaces or in confined volumes has been of interest in a number of research problems.

In this work, the biologically relevant system chosen for studying the behavior of water near an interface is composed of small pools of water encapsulated within reverse micelles which are aggregates formed from amphiphilic molecules. Water in these systems is thought to mimic water close to biological membranes or proteins, which are composed largely of lipids [5]. The chemical and physical properties of interfacial water in this system can then be studied using a fluorescent probe molecule within the reverse micelles by means of ultrafast laser spectroscopy.

## 1.1 Experimental Studies on Interfacial Water

### 1.1.1 Importance of Liquid Water in Biological Systems

The importance of water in biological systems is apparent, since it constitutes more than 70 % of the mass in most forms of life [6]. We also recognize that water is a most attractive biological substance that is deeply involved in the subtle mechanisms of life. Besides the most important constituent of the cell, it has other significant functions. For instance, it is needed to dissolve and transport nutrients, other vital substances, and wastes in an organism. Therefore, we believe that it is one of the most valuable subjects that requires study in depth.

Water is an essential solvent as well as a substrate for many cellular reactions. The macromolecular components of cells, such as proteins, carbohydrates, lipids and nucleic acids, interact extensively with water, and much of the metabolic activities of cells operate in an aqueous environment because water acts simultaneously as a medium and a direct participant in biochemical reactions [7,8]. Consequently, small amounts of liquid water may profoundly affect ionic and molecular transport, reaction equilibria and kinetics, etc. Although the physical and chemical properties of water play a dominant role in many biological processes, the structure and function of this simple molecule in a biological system is not yet completely understood in spite of its fundamental importance [3].

There are several critical biological consequences for unique and unusual properties of liquid water, which make it a stable environment for living organisms [9]. Water participates in various specific functions such as enzyme catalysis and channels for the passage of ions or molecules.

One of the most well known properties of water is that liquid water at 4 °C is more dense than ice. Thus, a layer of ice on a lake or a river insulates the creatures below from extreme cold because ice floats and water freezes from the surface down.

The high specific heat and the high thermal conductivity of water are important to biological systems because metabolic activity generates large amounts of heat, which is readily absorbed and distributed by water through the system. Thus, water helps regulate and stabilize metabolism, helping to maintain a relatively constant temperature throughout. This factor is especially important for enzymes which function effectively only within narrow temperature ranges [7].

Like its high specific heat, the high heat of vaporization of water also serves to moderate environmental temperature changes. Because the evaporation of water absorbs so much heat, sweating and perspiration are an effective mechanism for dissipating body heat.

Water plays an active role in certain biochemical reactions, such as hydration, within a narrow temperature. Water surrounds most cells in our body and diffuses freely through the cell membrane. Many substances vital to cells are dissolved in water because of its high polarity. Cells are then affected by the diffusion of these substances. Much of the other remarkable characteristics in biological systems can be explained in conjunction with the unique properties of water.

These important biological activities take place in the region near cellular membranes, where the water properties may not be consistent with those of bulk water. It is greatly required to understand the nature of the interactions of this interfacial water with cell membranes. However, it is very difficult to study directly the physical and chemical properties of any real biological system because of its complex environment. In order to get some insight into its properties, it is necessary to use models.

### 1.1.2 Interfacial Water

Interfacial water, lying between a bulk liquid water phase and an adjoining phase, occurs in many situations of physical, chemical, and biological interest. For example, cell surfaces and bubbles consist of a water/membrane and a water/air interface, respectively. Interfacial water is present when liquid water is in molecular contact with surfaces of ice,

quartz, oil or metals. It can play a dominant and fundamental role as the medium that controls structure, function, dynamics, and thermodynamics near interfaces and surfaces or in other confined regions of space.

A knowledge of the properties of interfacial water is of great importance for a full understanding of the stability and behavior of proteins, membranes, and in some natural homogenous substances. The unusual physical properties of interfacial water have received the attention of many investigations since interfaces are of fundamental scientific, environmental, and medical importance [10]. However, the highly complex nature of water structure at interfaces or surfaces has somewhat prevented a good understanding of its chemical and physical properties when confined within very small volumes.

It is believed that water close to ions, interfaces, or biopolymers is more structured than bulk water [11]. Water is easily perturbed at a surface or an interface, causing it to have abnormal properties. Strong structural perturbations at a surface are inconsistent with the ordinary directional bonding between water molecules in the bulk liquid. These perturbations are induced to form a partially ordered arrangement of water by interaction with the surface. Therefore, the perturbation of liquid water structure and dynamics at interfaces could modify normal properties of bulk water and exert a significant influence on chemical reactions, such as acid-base equilibria, and on phenomena that take place in biological systems. In order to obtain some properties of interfacial water, its structure and dynamics have been investigated both theoretically and experimentally using various models. However, questions [4,12] still abound as to the distance these perturbations extend from the surface.

The availability of large scale computers has provided a new way of investigating aqueous solutions, that is, by computer simulation. The study of structural and dynamical properties of aqueous solutions using computer simulations started with the pioneering work of Rahman and Stillinger [13]. Using computer simulations with the molecular dynamics (MD) or the Monte Carlo (MC) method, the study of liquid water near various surfaces or interfaces has been performed in detail in recent years. The system of surfaces considered includes a layer of liquid water confined between two solid surfaces [14,15], liquid-filled pores [16], the water liquid/vapor interface [17,18], the ice/water interface [19], a self-supporting thin film [20], ionic interfaces [21,22], the water/apolar solid interface [23], and strong laser fields [24]. MD simulations are now being widely used as a tool to understand the physico-chemical behaviors of the biological macromolecules [25].

From MD simulations, microscopic quantities of interest in the interface that have been studied, include the density profile, surface tension, surface potential, molecular orientational and translational order, the rate of molecular diffusion and thermodynamic quantities such as heat capacity, compressibility and expandability. Most of these simulations have come to this conclusion: the properties of liquid water at a surface or an interface are generally quite different from their bulk properties and agree with the presence of mild perturbation.

In contrast to theoretical work, very few detailed experimental investigations of interfacial water have been carried out. It has proven difficult experimentally to elucidate the liquid structure of water at a general surface. Most of the experimental information

concerning the structure of interfacial water is derived from nuclear magnetic resonance (NMR) spectroscopy [26,27], ultrafast lasers [28], neutron scattering [29], and X-ray diffraction [30]. These techniques have provided some details of the properties of the confined water phases.

Direct measurements by ultrafast laser experiments have been performed by Robinson et al. [11,31] in order to study dynamic properties such as diffusion of the perturbed water in various interfaces and confined volumes. Recent experimental studies using optical second harmonic generation (SHG) methods have been developed to probe the molecular arrangement and the orientational order at the water liquid/vapor interface [32] and to study the photochemical and photophysical processes at various liquid interfaces [33].

### 1.1.3 Reverse Micelle

There exist many sources available for interfaces and confined volumes for the study of surface-perturbed water [27]. One type of system employs amphiphilic molecules, or “amphiphiles.” The term amphiphilic comes from the Greek, meaning “loving both sides.” The amphiphilic substances like detergents or surfactants possess two parts: the polar head group is said to be “hydrophilic,” or water loving, and the nonpolar hydrocarbon tail group to be “hydrophobic,” or water fearing. Many kinds of amphiphiles form molecular aggregates which are called “micelles.” In this research, we use the amphiphilic molecule as surfactant Aerosol-OT (AOT) or sodium bis (2-ethylhexyl) sulfosuccinate, whose molecular structure is depicted in Figure 1.1. The AOT molecule

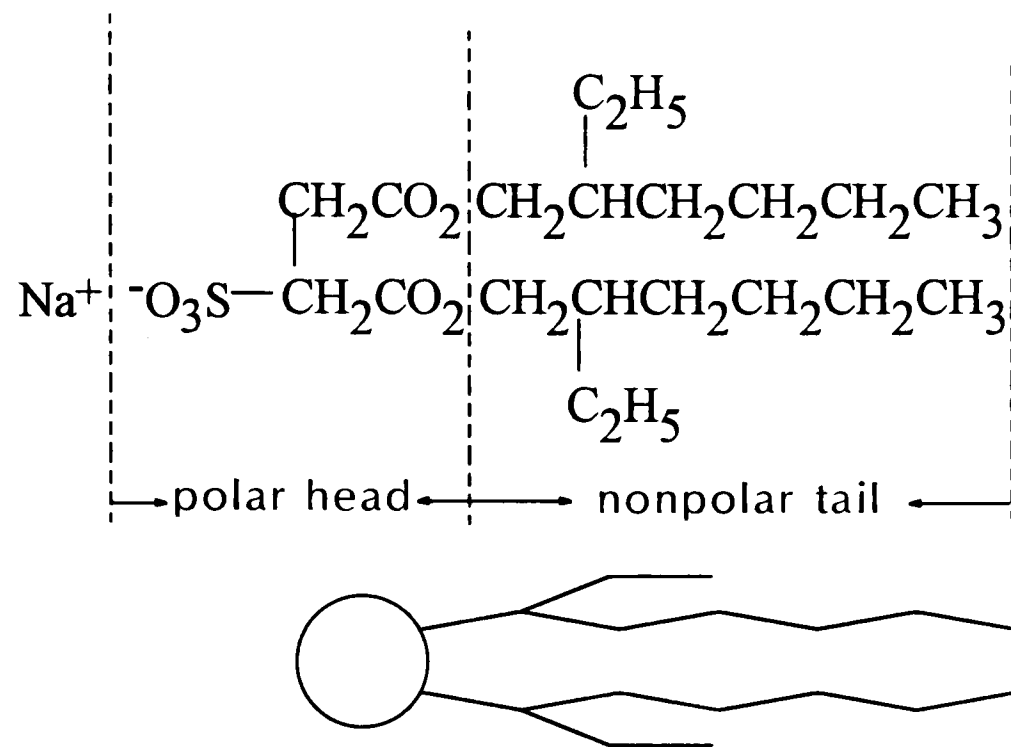


Figure 1.1. The chemical structure (above) and the symbolic representative (below) of an AOT molecule showing the twin hydrophobic tail groups to the right and the hydrophilic head group to the left.

structure is composed of three parts: a sodium ion, a hydrophilic sulfonate head group, and two hydrophobic alkyl chain tails.

The reverse micelles (RM) can be present in the solutions of various amphiphiles with small amount of water in apolar organic solvents. When such molecules are added to an apolar solvent such as heptane, their hydrophilic heads tend to cluster together hiding themselves from the heptane medium. On the other hand, the hydrophobic tails want to make contact with the heptane solvent, forming bilayers, microemulsions or micelles [5]. Water added to this mixture seeks out the hydrophilic region of the amphiphile mosaic, and “reverse micelles” (water on the inside) are formed as shown schematically in Figure 1.2. The sodium ions from the AOT molecules may dissociate into the water, leaving behind negatively charged heads.

AOT reverse micelles are of great interest because they are relatively easy to make and are representative of many biological systems such as naturally occurring phospholipid membranes [5]. If AOT is added with a primary hydrocarbon solvent, together with a little water, spherically shaped reverse micelles containing small pools of water can be formed [34-38]. The RM's size is primarily controlled by the molar ratio of water to surfactant AOT,  $w_0 = [\text{H}_2\text{O}]/[\text{AOT}]$ . So, this system is often used as models of water pockets because it is well-defined in size, shape and aggregation number. The RM structure is capable of forming a sphere of pre-determined size containing up to 70,000 water molecules [34]. Thus, the RM structure provides an opportunity to investigate the properties of water within a confined volume.

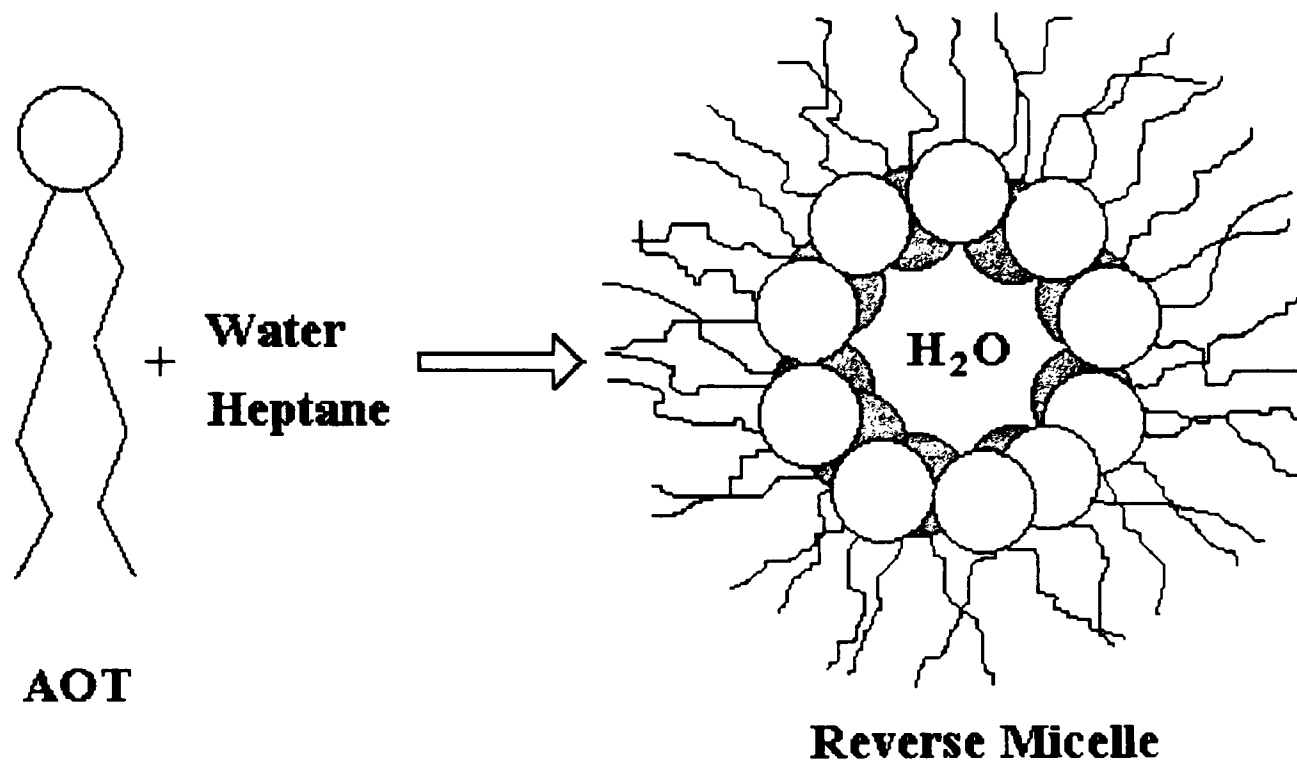


Figure 1.2. The schematic view of reverse micelle structure formed by water and AOT in heptane solution.

Besides the biological relevance of the reverse micelle, knowledge about micelles and microemulsions composed of amphiphilic molecules is important from a technological point of view [39]. It is important in the study of tertiary oil recovery in the petroleum industry, surfactants and detergents, dye solubilization, catalysis, food technology, liquid-liquid extraction of minerals from ores, photographic emulsions, lubricants and corrosion inhibition.

These reverse micelles have already been the subject of much experimental work. Aggregational parameters of reverse micelles, including their size, have been determined by various experimental techniques such as nuclear magnetic resonance (NMR) [34,35], small-angle neutron scattering (SANS) [36,38], small-angle X-ray scattering [40], time-resolved fluorescence methods [41,42], infrared spectroscopy [43] and many other techniques [37]. It is concluded that the micelle size depends primarily on the molar concentration ratio of water to surfactant.

Since the water inside reverse micelle seems to have properties quite similar to the water adjacent to an interface, it is interesting to investigate how the presence of perturbations modifies the chemical and physical properties of the liquid water. The perturbations induced by these surfaces can arise either from direct chemical interactions or from effects that may afford information on the dynamic properties of the system.

There has been concern over the role and properties of water molecule bound to the AOT interface and those free to move and rotate in the center of the pools. Two or more types of water have been observed with different mobility characteristics, one more organized tightly associated with polar heads and the other relatively free, but still

markedly different from bulk water [44,45]. Determinations of deuterium relaxation times have shown that the two water populations are in slow exchange [44].

#### 1.1.4 Fluorescent Probe Molecules

To study water properties in reverse micelles, a fluorescent probe molecule must be added to the RM solution. If sufficiently small concentrations of probe molecules are used, all water pools statistically contain either one probe molecule or none, thus avoiding possible complications from multiple occupancy. In order to measure the light emission from such a tiny sample size, a very sensitive detection technique, such as time-correlated single photon counting (TCSPC) [46], must be employed and is detailed in Chapter II. The probe molecule in this RM system is excited by an ultrafast laser and the detected decay profile then allow us to investigate certain physical and chemical properties of liquid water near biological interfaces.

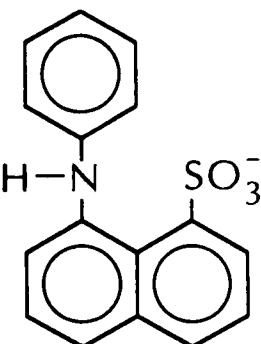
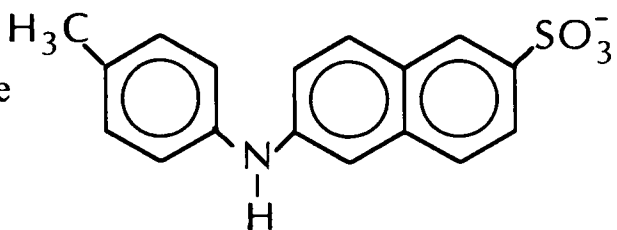
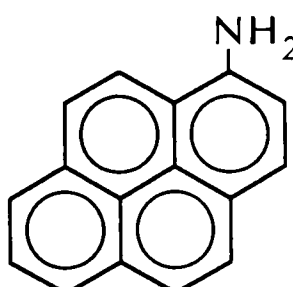
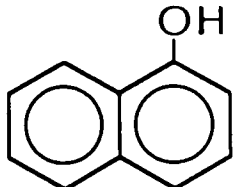
Since interfacial water appears to be more structured and orientationally stiffer than bulk water [11], ultrafast ionic reactions can be slowed by orders of magnitude in interfacial water. Fluorescence probe molecules whose characteristics depend on these ionic reactions can distinguish these different forms of water. Because of a photon-induced charge-transfer-to-solvent (CTTS) process, its rate is changed in a stiff water environment where orientational freedom of the solvent is modified [47]. Therefore, we will use the ultrafast laser methods to learn about the translational diffusion and the charge transfer profiles as a function of distance from the interface of the RM.

Since one of the purposes of this study is to attempt to measure diffusion rates in confined water, probe molecules with fast decay time [48] are required. The diffusion coefficient  $\mathcal{D}$  for a moderately large organic hydrophile, such as 1-naphthol, is about  $0.67 \times 10^{-5} \text{ cm}^2/\text{s}$  ( $0.067 \text{ \AA}^2/\text{ps}$ ) at  $20^\circ\text{C}$  in pure bulk-state water, which is estimated using the Hayduk and Laudie method [49]. We will see later that the diffusion coefficient in confined water can be much less than this. However, if it is initially assumed that in the reverse micelle the diffusion coefficient of the dissolved probe molecule had the same value as it does in bulk water, the average time  $\langle \tau \rangle$  for diffusion ( $\langle r^2 \rangle = 6\mathcal{D}\langle \tau \rangle$ ) of such a molecule from the center of the RM to the interface in a  $50 \text{ \AA}$  radius water pool would be about 6 ns; while the average time  $\langle t \rangle$  to diffuse  $10 \text{ \AA}$  in a direction normal to the surface ( $\langle z^2 \rangle = 2\mathcal{D}\langle t \rangle$ ) is 0.8 ns [50]. Any detection technique with response time longer than 6 ns would tend to average out the diffusion process, and detailed information about the properties of water in different regions of the micelle would be lost.

Fortunately, many subnanosecond probe molecules, whose excited state lifetimes are strongly perturbed in confined water, do exist. A few examples are sodium salts of 8-1 anilino-naphthalene sulfonate (ANS) [51], 6-2 toluidinyl-naphthalene sulfonate (TNS) [52], 1-aminopyrene [53] and 1-naphthol [54], but all of these are not equally well-studied for the AOT RM studies. The structure formulas of these probe molecules are given in Table 1.1 together with their diffusion coefficients  $\mathcal{D}$  in pure water at  $20^\circ\text{C}$ .

One advantage of the proposed technique is that, near a surface, perturbations slow the competing nonradiative charge transfer, leading to a much higher fluorescence

Table 1.1. Acid Fluorescent Probe Molecules and Their Diffusion Constants in Pure Water.

Name	Formula	$D$ ( $10^{-5} \text{cm}^2/\text{s}$ ) <sup>a</sup>
8-1 Anilino-naphthalene sulfonate (ANS)		0.46
6-2 Toluidinyl-naphthalene sulfonate (TNS)		0.46
1-Aminopyrene		0.54
1-Naphthol		0.67

<sup>a</sup> The diffusion coefficients are calculated using Hayduk and Laudie method [49].

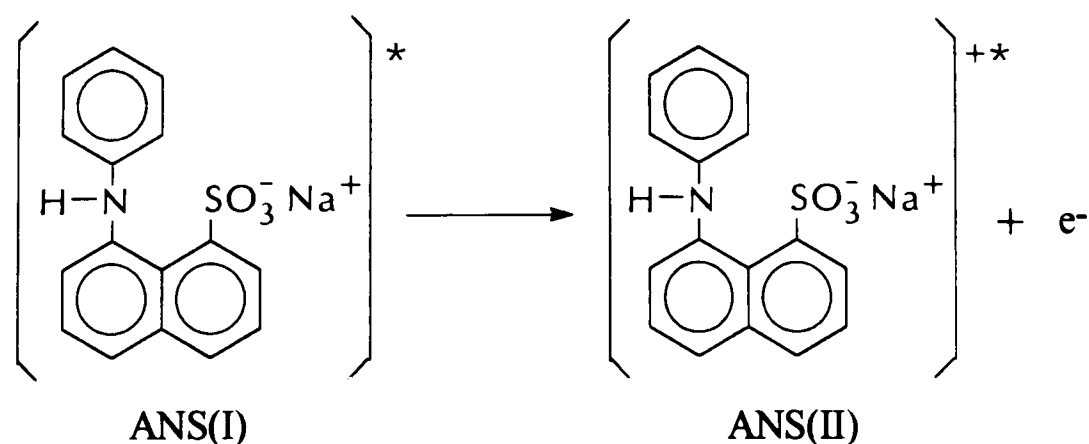
quantum yield than in regions far from the surface. Close to the surface, therefore, for the small, but most crucial, and most interesting, regions of perturbation, photon signals are relatively much more intense than those from the more bulk-like, less interesting regions of the sample. An advantage specifically of ANS (or TNS) is that there is apparently no effect of dissolved cations on the photophysics. Free  $\text{Na}^+$  lengthens the lifetime of 1-naphthol considerably [55], but seems to have no effect whatsoever on the lifetime of 1,8-ANS [56].

A more severe problem for the study of AOT reverse micelles is posed by solubility characteristics: the probe molecule must of course be soluble in water, but it must also be insoluble to a very high degree in the primary hydrocarbon solvent. Sensitive TCSPC monitoring of their fluorescence [56] has confirmed that ANS and TNS are virtually insoluble in n-heptane, so that these probe molecule and primary solvent combinations are ideal for the present studies. Unfortunately, though it has been used in other confined water experiments [11], in the case of the simple and relatively well understood [54] 60 ps probe molecule, 1-naphthol, excessive solubility in all known primary hydrocarbon solvents prevents it from being used in the AOT reverse micelle studies. The large amount of background fluorescence from 1-naphthol in the primary solvent overwhelms the desired fluorescence from the minute reverse micelle volumes.

The probe molecule ANS has been the subject of considerable interest ever since Weber and Laurence recognized the sensitivity of its fluorescence to solvent polarity [57]. For many years, it has been also used as a probe for the delineation of water-like versus non-water-like regions in biological systems in two ways [58]. The first is through

fluorescence quantum yield measurements [51], which show over a two-order-of-magnitude decrease in the yield as the environment changes from a solvent such as ethanol to a pure water environment. The second is through fluorescence lifetime determinations, which show greatly abbreviated lifetimes in the pure water environment, 280 ps in water compared with  $\sim 8.6$  ns in ethanol. While the understanding of this effect is not yet entirely complete, the combined lifetime and quantum yield data do show clearly that, in competition with the relatively slow light emission process, a much faster nonradiative decay of the electronically excited ANS molecule is promoted in a sufficiently water-like environment. The fast decay, whatever its nature, can take place only if some  $\text{H}_2\text{O}$  or  $\text{D}_2\text{O}$  is present. Quantum yield studies [51,56] have shown that highly polar solvents such as ethanol or acetonitrile are inert as far as promotion of the fast decay event is concerned. Thus, solvent structure is implicated here, rather than solvent polarity.

A more specific view concerning the nature of the fast decay process in these types of probe molecules has been suggested through pure and mixed solvent experiments in our laboratory [51,59,60]. This idea is that the fast decay transition in ANS in a liquid water environment is electron dissociation following one-photon excitation. This transition in the excited state is represented in the following scheme with molecular formulas:



The transient appearance [56] of an absorption resembling the finger print 700 nm [61] absorption of the hydrated electron tends to support this view. The rapid rate of this process in normal bulk water is very likely caused by a fast reorientation time for the water molecules to accommodate the newly formed electron, combined with a low activation free energy for the overall process, which undoubtedly would have to involve tunneling of the electron.

Mixed water/alcohol solvent studies [59,60] have further shown that the liquid water environment can be suitably emulated by a local solvent structure containing about four water molecules. While this structural requirement is local, the reorientation time needed to attain this structure depends on longer range phenomena, such as the Debye relaxation time (solvent dynamic parameter), or collective dipole moment relaxation time,  $\tau_D$  (298 K, H<sub>2</sub>O)  $\approx$  7.0 ps.

Therefore, the picture that emerges is one where hydrogen bonding of the local solvent molecules to the solvated electron is required, but where the time to produce the overall solvent structure depends on rotational reconfigurations over a large volume. Even through the long-time equilibrium structures may have similar aspects, this production time is much faster in a group of water molecules than when more slowly rotating, alcohol molecules are present.

#### 1.1.5 Contents of Present Work

The main aim of this study is to understand how much the properties of water change near an interface. One of the most direct approaches to the study of water

properties on the hydrophilic surfaces is to analyze the lifetimes of the probe molecule. Not only does the decay of probe molecule tell us what solvent molecules are on the surface but it also tells us something about the nature of the bonding to the surface. We are assuming that the probe molecules have a statistical distribution throughout the RM. This work is intended to present a relatively complete description for experimental and analytical studies of interfacial water using an ultrafast laser spectroscopy.

We introduce a powerful scheme of experimental techniques that can be applied to study the properties of water in biological environments. We also present a new methodology for analyzing certain chemical and physical properties of liquid water near an interface. Much of the theoretical work has been directed to study interfacial water in various biological systems and to proceed towards a molecular-level understanding of water models [25,62-64]. However, except for a relatively brief review article [65], there has been no recent detailed experimental study concentrating on water. The recent monograph [3] by Robinson et al. for water extensively reviews recent progress in computer and experimental studies of water at macroscopic interfaces.

Following this Introduction, the rest of the PART I is organized into two subjects, namely the experimental (Chapters II and III) and the analytical (Chapter IV) parts. Chapter II presents the experimental lifetime measurement, TCSPC technique, and is also devoted to a detailed description of the general concepts for the experimental apparatuses for studying interfacial water systems. Chapter III presents useful decay data obtained from experiments, not only for the bulk phase, but also for water in various RM sizes. Chapter IV, on the other hand, describes in detail the new analytical method to explain

certain properties of interfacial water. Using this method, we analyze the decay data obtained from our RM model and present the results for some properties of interfacial water. Finally, the results of this work are briefly summarized and a conclusion is given in Chapter V.

## 1.2 Computer Simulation of Liquid Water

We have gained much knowledge of pure liquid water experimentally such as its remarkable chemical and physical properties. However, we still find many unsolved mysteries among the anomalous properties of liquid water [66,67]. We do not know how to explain such anomalous properties [68-71] by the theoretical descriptions.

Most of these anomalous properties of liquid water, including transport properties and heat capacities [67], the density maxima [72,73] near 4 °C (H<sub>2</sub>O) and 11 °C (D<sub>2</sub>O), and the minimum in the isothermal compressibility near 50 °C (H<sub>2</sub>O) [74], are explained by its hydrogen bonding characteristics in textbooks: for example, the density of water increases as the liquid cools until it reaches a maximum at 4 °C. However, as the temperature drops below 4 °C, the density of water decreases unlike most substances leading to an expansion. This expansion is believed to be caused by the formation and the disruption of the hydrogen-bonded structure. What are the entities of the hydrogen-bonded structures? How can they have an effect on the properties of water?

The first explanation of this phenomenon was suggested by Röntgen in 1891 [75]. He proposed the first mixture model for liquid water in which water consists of an aggregate of two types of differently constructed molecules. This idea was followed by

Bernal and Fowler [76], Kamb [77], and more recently Robinson [67,72-74]. The anomalous density maximum can be explained through recognition of the importance of second-neighbor structures derived from the bending, rather than the breaking, of hydrogen bonds, a type of bonding that is already known to exist in the more stable higher density ice forms [77]. This analysis has in fact indicated the disappearance with increasing temperature of open intermolecular tetrahedral bonding (ice-I-type) having a density similar to that of ordinary ice, in favor of compactly bonded regions (ice-II-type) with a density near that of the dense ice polymorphs, ice-II and -III, particularly, but also ice-V and -VI. The densities in these low- and high-density types of ice are bunched near  $0.92 \text{ g/cm}^3$  and  $1.2 \text{ g/cm}^3$ , respectively. Since the absolute structure of liquid water has not been determined, one cannot be sure. However, it is believed that the hydrogen-bonding pattern of liquid water is more irregular than that of ice.

There is an increasing awareness that understanding this one property will reveal the origins of all the other anomalous properties of water, and thus will provide a complete molecular-level description of this most important liquid in its bulk phase, as well as in the interfacial states of this substance. However, currently popular computational models of water are simply unable to reproduce this anomaly, as so aptly stressed in the abstracts of two very recent papers [78,79]. It would seem that, if a model does not possess this basic property of the real liquid, it cannot provide any sort of an accurate picture in biological, chemical or geophysical applications, on which an ever increasing amount of computational effort is now being spent.

Motivations and precepts for developing a much better molecular-level picture of liquid water, from the experimental, theoretical and computational points of view, are clear. First of all, one would like to make predictions with regard to properties that either have never been considered experimentally or that have been difficult to measure in the laboratory. This requires that the theoretical model be capable of appropriately reproducing all the known phenomena, particularly the density maximum and other key anomalies. Furthermore, any model claiming to represent real water must correctly reflect variations in its most important properties over wide ranges of temperature, pressure, surface perturbations, etc. Unfortunately, none of the existing models has yet come close to reaching this goal [65,78-81], though a few attempts [82-85] to develop a model that reproduces some properties of water from the gas to condensed phases have been made.

Recent experimental investigations have suggested important avenues of approach towards the ultimate resolution of this problem. For example, vibrational Raman data [86] over a range of temperatures from the supercooled region indicate a mixture of resonances, one exhibiting strong hydrogen bonding as in normal ice, the other having a lower degree of such bonding. This picture has been carried farther by Vedamuthu, et al., where it was found to be quantitatively consistent [72] with a number of experimental properties of water: the temperature-dependent density of H<sub>2</sub>O from about -30 °C to +40 °C to the five-decimal-place precision of the experimental data [87]; the temperature-dependent density [73] of D<sub>2</sub>O to its four-decimal-place precision [88]; the density [89] of T<sub>2</sub>O [90]; and the isothermal compressibility of H<sub>2</sub>O, including its minimum [74], to the three- to four-decimal-place precision of its measurement [87]. Recently, based on the

same type of considerations, a "thermal lag effect" has been employed [90], which normalizes the structural properties of H<sub>2</sub>O, D<sub>2</sub>O, and T<sub>2</sub>O. Only in this way was it found that isotope effects for a variety of dynamic properties, including the viscosity and self-diffusion coefficients, be accurately assessed. Surprisingly, in the past, isotope effects in water were not found to fit any sensible pattern [91].

Still more revealing are isochoric differential x-ray scattering data for liquid D<sub>2</sub>O [92,93], again spanning both supercooled and normal temperature ranges. These data reveal a pronounced radial distribution function peak near 3.35 Å in liquid water that does not occur in the low density ices. This peak coincides with the second-neighbor non-hydrogen-bonded O···O distance in the dense ice forms mentioned above [94]. In addition to the 3.35 Å ice-II-type peak, which grows in with increasing temperature, the differential x-ray scattering data also show that the ice-I-type second-neighbor O···O peak near 4.5 Å decreases in intensity with increasing temperature. Because it does not occur in the dense polymorphs, this 4.5 Å distance, rather than the approximate 2.8 Å distance, which occurs in every known form of ice, acts as a "fingerprint" for the presence of the open tetrahedral bonding in liquid water. These experimental results therefore provide direct experimental evidence, not only for the presence of both the open ice-I-type and the more dense ice-II-type bonding in the liquid, but also for the transformation of the open form to the dense form with rising temperature. Based on earlier x-ray scattering studies, Kamb [77] reached a similar conclusion about these mixed density forms in liquid water. A most important feature of this variable bonding concept, since it is completely foreign to current thinking about liquid water, must continually be emphasized: these bonding variations are not at the

nearest-neighbor level, but instead occur in the outlying non-hydrogen-bonded second-neighbor O···O structure.

From the early crystallographic work [76,94] it is already well known that changes in the crystal structures of the various ice polymorphs always occur outside the first-neighbor shell. Going to the second shell in normal ice-Ih, the oxygen-oxygen distance is the continuation of the open tetrahedral network structure at  $\sim 4.5$  Å. However, in the higher density ( $\rho > 1.15$  g/cm<sup>3</sup>) crystalline ice polymorphs, hydrogen bonds that form the second-neighbor shell are bent [77], creating condensed oxygen-oxygen distances. In fact, in the most stable moderately dense forms of ice, this second-neighbor distance lies near 3.4 Å. In a recent paper on neutron diffraction studies [95] of liquid D<sub>2</sub>O under pressure down to temperatures of  $\sim 65$  °C, bond bending is again suggested, “The effect of pressure is subtle in the sense that it does not change substantially the number of hydrogen bonds, but the O···O···O angles are modified (p. 3734).” This is exactly what happens when the open oxygen-oxygen bonding in the second-neighbor shell changes over to the more dense structure at 3.4 Å. All these structural features in the liquid and in the crystalline polymorphs of water provide a picture that is in perfect concordance with the differential x-ray diffraction results [92] for the liquid, and help to identify the new neighbors as a structure already inherent in condensed phases of water. It seems clear then that the water-water potential in computational models should be modified in such a way that it can provide a subsidiary second-neighbor oxygen-oxygen minimum near 3.4 Å, while keeping intact under appropriate thermodynamic conditions the open tetrahedral structure.

In this study, the feasibility of the above idea is tested with an exactly solvable analytical model. In order to carry out this analysis, we must consider only second neighbors in liquid water, ignoring the first neighbors altogether. The justification for this simplification rests on two experimental properties: (1) the number density and structure in the first shell of the liquid are not strongly affected by temperature [92], and (2) the oxygen-oxygen nearest-neighbor distances in all forms of the liquid and ice are the same,  $\sim 2.8 \text{ \AA}$  [77,92,94]. For these reasons, nearest neighbors cannot play a significant role in determining thermally induced or pressure induced density variations in liquid water, except weakly through ordinary compressibility and thermal expansion. The nearest neighbors can be considered as part of an invariant inner "core." One might then expect that the second-neighbor structure determines the density. This structure is seen to depend on two minima, a close-in metastable one near  $3.4 \text{ \AA}$  and a farther-out deeper minimum at  $\sim 4.5 \text{ \AA}$ . The shallower minimum may not be evident from quantum calculations on small water clusters, particularly the dimer.

The purpose of the present study is twofold. The first is to report some analytical results on an exactly soluble one-dimensional fluid model of liquid water [96,97]. This model very simply illustrates the origin of the density maximum and its pressure dependence. The second purpose is to present the preliminary studies on an NVE molecular dynamics simulation for a realistic water model, whose potential is augmented with a second-neighbor potential, as a further step in the development of a water-water model that gives rise to the known anomalies.

The contents of the PART II are divided into two chapters. In Chapter VI, the one-dimensional fluid model will be fully described and tested with simple potential functions. Using information provided by simple potentials, it will construct the double well potential, which gives a density maximum. Some useful results will be given together with providing a realistic explanation of the density maximum for water.

Combined with the ideas as explained above and the results of Chapter VI, Chapter VII proposes a new potential function of water which is a three-dimensional form, not only with distance dependence, but also depending on the angles. To test the new potential, we will first employ an NVE molecular dynamics simulations and will describe it, followed by the results and discussion.

PART I

STUDIES OF THE PROPERTIES OF LIQUID WATER  
IN REVERSE MICELLES USING AN ULTRAFAST LASER

## CHAPTER II

### SINGLE PHOTON COUNTING LIFETIME MEASUREMENT

#### 2.1 Introduction

The early lifetime measurement techniques provided a direct method to measure the fluorescence decay of a molecule with only a few microseconds [98]. The accessible lifetime time range has been extended now to sub-picoseconds by the improvements of powerful excitation sources, fast detector, data analysis etc. The time-correlated single-photon counting (TCSPC) method has now become an increasingly valuable technique in a wide variety of fields such as chemistry, biology, and physics because it can measure the lifetime of a short-lived excited compound in a complex system, which helps in the investigation of the chemical and photophysical processes in the excited state.

To study the structure and dynamic behavior of water at an interface, the probe molecules in a confined biological system are excited, and the induced fluorescence is detected by the TCSPC technique. If the lifetime of the probe molecule is long enough for the excited probe to interact with its immediate environment, it gives direct information on dynamic processes and photochemical reactions in a picosecond time region.

The techniques and the instrumentation of the TCSPC method are well discussed in detail in the monograph by O'Connor and Phillips [46]. The TCSPC is a statistical technique used to measure the time profile of the emission of a sample after excitation by a short light pulse. The basic concept of acquiring TCSPC data depends on measuring the time difference between the excitation pulse and the occurrence of the emission of a

photon from the sample. By accumulating many such events in a histogram, the probability distribution yields the time profile for the emission of sample.

## 2.2 TCSPC System

The TCSPC system employed here can be divided into four fundamental elements: the laser excitation source, the detector system, the timing electronics, and data acquisition. The major advance in the TCSPC instrumentation has been particularly rapid over the years since the pulsed laser excitation with sub-picosecond high repetition rate and the microchannel plate photomultiplier detector have been developed [99-102]. A typical experimental set-up which is used for lifetime measurements is shown schematically in Figure 2.1.

With aid in Figure 2.1, the overall operational principle is briefly described as follows: The excitation source is split into two optical pulses by the ultraviolet (UV) pass filter. One of the optical pulses excites the sample which subsequently fluoresces, and the photomultiplier tube (PMT) detects at most one photon through a monochromator. This is accomplished by adjusting an aperture or inserting a diffuser. The electric signal resulting from this photon supplies the start signal of the time-to-amplitude converter (TAC), which initiates charging of a capacitor, through an amplifier and a constant fraction discriminator (CFD). In the meantime, the other beam is detected by a photodiode which generates the electrical pulse at a time exactly correlated with the time generation of the excitation pulse. This trigger pulse is used as the reference timing pulse.

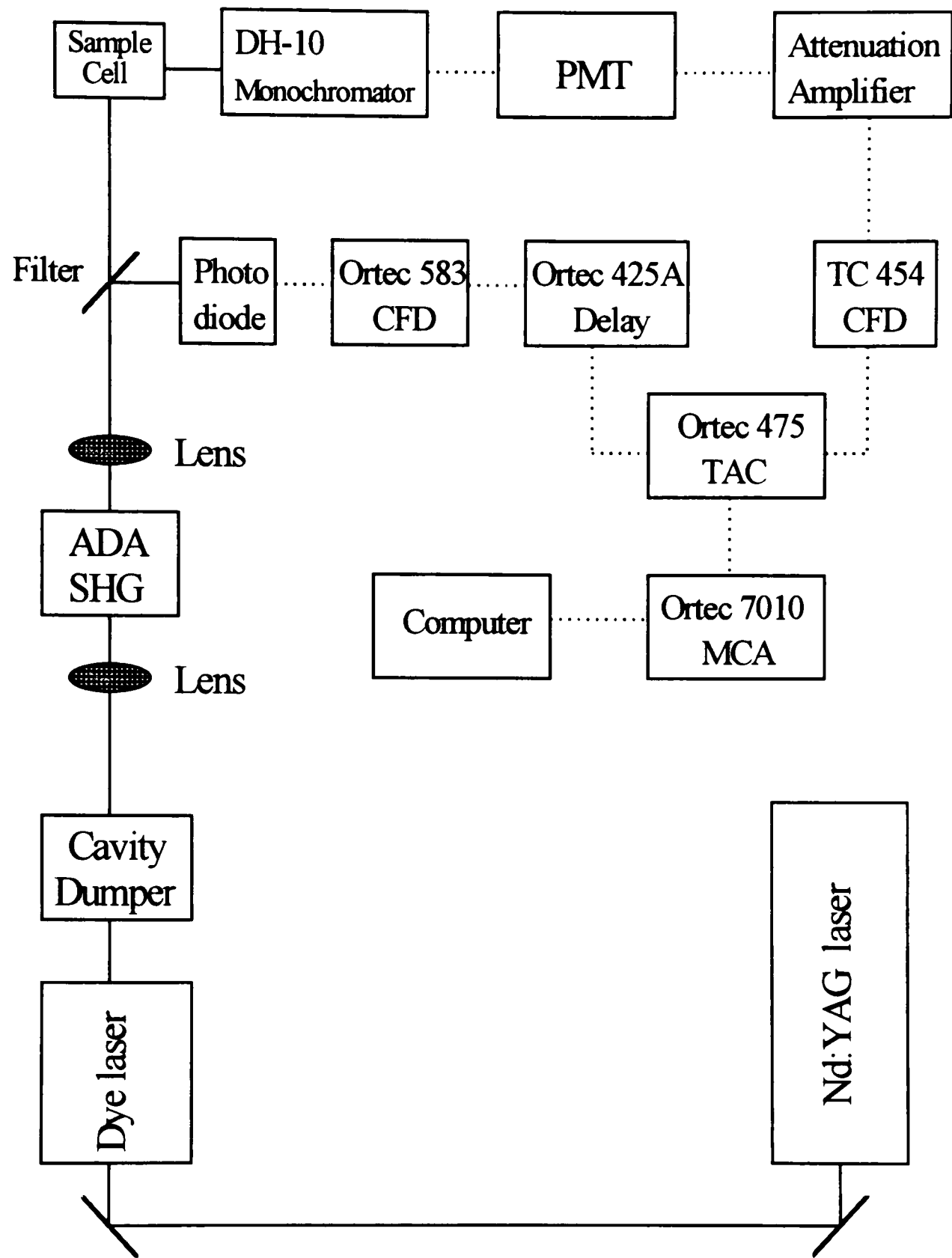


Figure 2.1. Block diagram of apparatus for the measurement of lifetime: ADA, frequency doubling crystal; SHG, second harmonic generator; PMT, photomultiplier tube; CFD, constant fraction discriminator; TAC, time-to-amplitude converter; MCA, multichannel analyzer. The solid and the dotted lines represent an optical and an electric signal, respectively.

It is routed to the CFD through a delay unit and then stops the charging ramp in the TAC. The time difference between the start and the stop pulses is proportional to the charge in the capacitor. The positive output pulses from the TAC are then scaled and are given a numerical value in the analogue-to-digital converter (ADC). A count is accumulated by a multichannel analyzer (MCA), which is interfaced to a computer. The experimental data are stored and analyzed on this computer.

### 2.2.1 The Excitation Source

A Nd:YAG laser, a dye laser and a second harmonic generator (SHG) are used to excite the sample. The dye laser is pumped by the beam of the actively mode-locked and frequency doubled Nd:YAG laser with mode locker and stabilizer. The radiation of the dye laser is frequency doubled by means of ADA ( $\text{NH}_4\text{H}_2\text{AsO}_4$ ) crystal used as SHG. If the cavity length of the dye laser is matched to that of the pumping mode locked Nd:YAG laser, the dye laser is said to be synchronously pumped.

The active medium of the Nd:YAG laser (Coherent Antares 76-s) is a solid consisting of  $\text{Nd}^{+3}$  ions in the form of impurity in a crystal of yttrium aluminum garnet (YAG). The Nd:YAG crystal is then optically pumped by high pressure krypton arc lamps and emits at the main wavelength of 1064 nm with 100 ps pulses. This fundamental pulse at 1064 nm of the Nd:YAG laser is converted to a second harmonic pulse of half the wavelength at 532 nm using a KDP ( $\text{KH}_2\text{PO}_4$ ) crystal as SHG. The final output of the Nd:YAG laser produces a pulse of width 70 ps with the mode-locking frequency 76 MHz

and has an average output power of approximately 1.5 W at 532 nm. This green laser beam is used to synchronously pump the dye laser.

The dye laser used in this system consists of two components; the continuous wave (CW) Coherent Radiation 599 dye laser and the Coherent Radiation 7210 cavity dumper. The active medium of the dye laser is rhodamine 6G (Exciton) at a concentration of about  $10^{-4}$  M which is dissolved in ethylene glycol solvent. It gives access to a tuning wavelength ranging from 560 to 650 nm [103], which is ideally suitable for lifetime studies of the fluorescent compounds of interest. The pump beam is focused on the dye jet through the input mirror of the dye laser. In order to avoid vibrations and bubbles in the dye stream, the dye is pumped via a corrugated Teflon tubing and a single-membrane filter. The desired wavelength is determined by a birefringent tuning filter made of three crystalline quartz plates, oriented at Brewster's angle. Rotation of the plates about an axis normal to the surfaces tunes the output wavelength. The output mirror of the dye laser is actually part of the cavity dumper so that the optical path length can be adjusted to match that of the Nd:YAG laser to achieve the synchronous pumping system. The average output power of the dye laser is usually greater than 150 mW at 610 nm with 3.8 MHz repetition rate.

The cavity dumper element of the dye laser system consists of an acousto-optic modulator and a radio frequency (RF) driver unit. The cavity dumper is used to provide selectable pulse repetition rates and to increase the peak power in the system output [104]. The acousto-optic modulator is used to deflect away part of the light pulse traveling within the dye laser cavity. As a result some of the laser energy is dumped out of the

resonant cavity in the form of a single high power optical pulse, by applying a strong acoustic pulse which is a controlled high frequency RF pulse from the cavity dumper driver. Since the pulse timing in the pump laser is given by the mode-locker driver of the pump laser, the pulse timing in the dye laser is controlled by the pump pulses and can be changed only by changing the phase of the mode-locker driver RF output. We set the repetition rate so that output pulses occur once every 10 cycles, which gives a pulse frequency of 3.8 MHz with about 10 ps pulse width.

In order to produce ultraviolet (UV) radiation from a dye laser pumped with Nd:YAG laser, the cavity dumped red beam of the dye laser is frequency doubled with a 50 mm-long temperature phase matched ADA crystal SHG. The doubler is placed at the focal point of the two lenses, which are identical both having a focal length of 7.4 cm. This allows for the largest solid angle of acceptance. This doubler converts about 100-500 mW output of the 610 nm beam to approximately 2 mW of 305 nm beam at the temperature 90 °C of the crystal. The resulting 305 nm pulse with a 10 ps width is ultimately used to excite the samples. The residual visible 610 nm radiation, which is due to low conversion efficiency of this frequency doubler, is separated by a UV pass filter (Schott UG 11). Figure 2.2 shows a schematic representation of the final pulse train after the ADA frequency doubler. The pulses are separated by about 260 ns so that there is enough time to get the SPC timing.

The final average output is approximately 2 mW at 305 nm which gives to a pulse energy of 0.5 nJ. Although it appears to be an extremely small pulse energy, it is

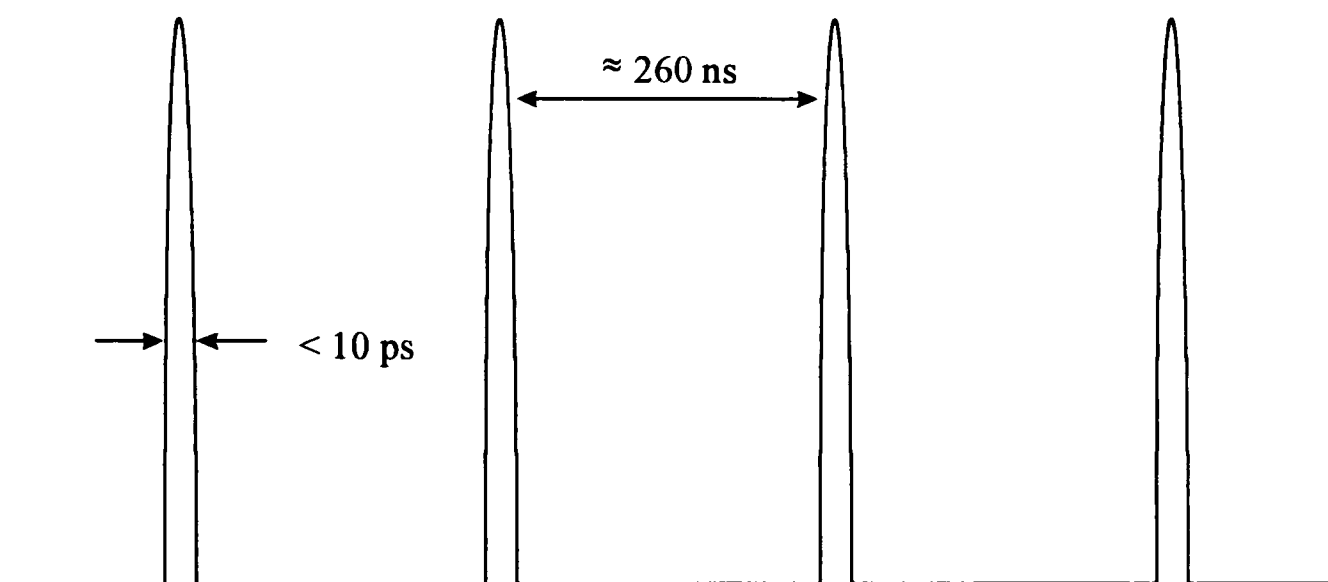


Figure 2.2. Schematic representation of the dumping pulse train of the dye laser output to excite a sample.

approximately equal to  $1.6 \times 10^9$  photons per pulse and is sufficient to acquire the photon counting data.

### 2.2.2 Photon Detectors

One of the most important parts of the TCSPC system is the single photon detector. Because light is quantized in the form of photons, detection of very low light levels ultimately moves into the regime of photon counting. The most efficient method for measuring a low light intensity is to employ a photomultiplier tube (PMT). The PMT must have a good detection sensitivity, a high signal/noise ratio, a high gain, and a fast time response. In the work presented here, there are two detection systems, the detector of the single photons emitted from the sample and the detector used in picking off the excitation laser pulse. As stated the previous section, the ADA frequency doubler has two outputs; the 610 nm fundamental beam to pick off the excitation pulse, and the 305 nm frequency doubled beam to excite the sample.

As a result of the excitation, a fraction of fluorescence emitted from the sample is focused by a lens and passes at right angles through a double monochromator (Instruments SA model DH-10) via a narrow rectangular slit in order to discriminate the required emission wavelength. These photons then strike the reflection grating in the monochromator at an angle. The dispersed radiation from diffraction is focused on the exit slit of the monochromator which selects the wavelength to be detected. The output from the monochromator is directed into the PMT.

The photons of selected frequencies are detected using a fast response and high gain 12-stage PMT (Amperex PM2254B). This PMT uses the trialkali photocathode material resulting in a 300-850 nm spectral response and a transit time spread of 250 ps. The PMT is operated at -2900 V with a high voltage power supply (Bertan 365). The PMT is used to convert radiant energy into electric signal. The photons enter the semitransparent photocathode that emits a cascade of electrons. Photoelectrons are then accelerated toward the first dynode, due to the potential difference between the photocathode and the first dynode. Each electron causes emission of several additional electrons, which are accelerated toward the second dynode. This process is repeated twelve times, and approximately  $3 \times 10^7$  electrons at a total voltage 2300 V for each photon. This cascade is finally collected by the anode. The resulting current, being a charge pulse, is immediately amplified by the HP model 8447F two-stage amplifier (0.1 MHz-1.3GHz bandwidth) with a gain of 26 dB and is converted into a voltage. The amplified single photon pulses from the PMT are approximately 200 mV at the peak, which is routed to the CFD and is adequate to trigger the TAC.

The fundamental beam of 610 nm is routed to the Antel AR-S2 photodetector, in which the detection element is a Positive-Intrinsic-Negative (PIN) type photodiode with passivated silicon. It operates by converting incident photons in the appropriate wavelength range into charge carriers in the silicon. Weak charge can then produce a current that is large enough to be readily detected by the electronics. In this photodiode, photons increase the conductance across a reverse-biased P-N junction with -18 V bias power. The detector has a risetime of 35 ps, a pulse response of 65 ps and a spectral

range of 300-1100 nm. It has a glass window, so it could not be triggered off the UV light. It produces a negative-going signal, greater than 1 V when it is displayed on the oscilloscope. This signal goes directly to a discriminator.

Recently, we replaced the old detector and other components connected to the PMT in our TCSPC system because it was found that microchannel plate (MCP) PMT has several desirable properties [101,105]. For short fluorescence lifetimes where resolution below 100 ps is required, the MCP-PMT is the fastest detector and offers a high gain with low noise performance. It can also be applied to the sample with a low fluorescent intensity. The MCP-PMT's apparently do not have the wavelength dependency of the instrumental response function (IRF), and with a laser source, relatively small IRF's of 40-100 ps have been reported [106].

The MCP-PMT introduced in our TCSPC system is Hamamatsu R3809U, having 6  $\mu\text{m}$  diameter channels which are secondary multipliers consisting of an array of millions of glass capillaries. It is of the proximity focus type, where the photocathode is very close to the MCP. This proximity type produces a very fast time response since it minimizes the transit time spread due to electron transit time differences between the photocathode and the MCP. The transit time spread and the rise time of this MCP is 6 ps and 160 ps, respectively. Since the gain of this MCP is  $10^6$  at 3000 V across the photocathode to the anode, this type of PMT is ideal for detecting extremely low level light. The PMT tube uses the multialkali (S-20) photocathode resulting in a 160-850 nm spectral response. This photocathode material has a high dark count rate of 1000 cps (counts per second) at

25 °C. Thus, it is necessary to cool this MCP-PMT with a Hamamatsu C2773 cooler to obtain low noise fluorescence decay data.

The determination of accurate fluorescence lifetimes by the TCSPC technique is often limited by difficulties in obtaining the correct IRF to the excitation pulse. One of these difficulties is increased when a grating monochromator is used to disperse the emission due to the path length difference for light of different wavelengths and the introduction of an additional temporal broadening of the IRF [107,108]. So, we removed the monochromator for filtering system. Instead, to avoid scatter of unwanted laser light through the detection system, a bandpass filter and a neutral density filter was typically used. Interference or colored glass filters were used to select the emission wavelength regions. The neutral density filter reflects 50 % of the incident light regardless of its wavelength (300-800 nm).

### 2.2.3 Timing Electronics and Data Acquisition

One of the purposes of the timing electronics is the measurement of the time difference between the excitation of sample and the detection of a single fluorescent photon. The start timing signal used to trigger the TAC is provided by the fluorescence emission, which is detected by a cooled PMT, amplified by a HP amplifier, and discriminated by a discriminator. The stop timing signal is supplied by a portion of the dye laser output, which is detected by an AR-S2 fast photodiode and discriminated by a discriminator via a passive inverting transformer with a 0.8 ns risetime capability. The output from the photodiode is delayed about 18 ns from the Ortec 425A delay box so that

the laser trigger from the photodiode is synchronized with the emitted photon detected by the PMT. The standard transistor-transistor logic (TTL) outputs from the discriminators are used as the start (PMT) and stop (photodiode) signals for the TAC. The output of the TAC is directed to a MCA, connected to an IBM AT computer. In this experiment, the actual number of counts acquired per second is in the range of 1000 to 2000 cps, depending on the laser intensity and sample quantum efficiency.

For an excitation source with high repetition rate, the conventional configuration of the TAC is not suitable because the TAC has no time to reset between the occurrence of successive excitation pulses [109]. In the conventional configuration, the start signal of the TAC is provided from a photodiode, and the PMT monitoring fluorescence provides the stop signal. The inverted timing scheme, which is adapted in this work, is used to facilitate data acquisition, allowing for the use of this high excitation source. In all other respects it is similar to the conventional configuration except that the decay curves are collected in the MCA with time increasing from higher to lower channel numbers.

The output from the PMT and the photodiode should be routed through a discriminator in order to improve the signal-to-noise (SN) ratio. The discriminator generates an accurate timing output, TTL signal, in order to furnish the TAC with a constant amplitude pulse that is independent of the input pulses. There are two operating modes of the discriminator, leading edge and constant fraction. In the leading edge mode, only input pulses with amplitudes between two discriminator levels are accepted and are timed at a low discriminator level. However, this mode is not suitable for the pulses with different amplitudes such as those from the PMT output since those pulses cross the

discriminator level at different times and result in a variation in timing. For this mode, the Ortec 583 discriminator is applied for the trigger pulses with very little noise for the pump pulse which is derived from a photodiode. On the other hand, the discriminator (Tennelec TC 454) with constant fraction mode is usually used for the single photon pulses from PMT. In this mode the input signal is split into two parts. One part of the signal is delayed and subtracted from the other part of the input signal. The resulting zero crossing point is fixed in time and this timing point is constant for pulses with varying amplitudes greater than a preset threshold. The output of the discriminator is the pulse used to initiate the cycle in the TAC.

The TTL output pulses from the discriminators are directed to the Ortec 457 TAC with a bias amplifier. The function of the TAC is to measure the time interval between the start and stop inputs and convert the measured time to a proportional output voltage. The corresponding timing with the inverted TAC configuration is illustrated in Figure 2.3. Upon acceptance of a start pulse by the PMT, a voltage builds linearly with time until the TAC receives a stop pulse within the selected time range. The output pulse of TAC is then generated with an amplitude derived from the final voltage. The height of the output pulse is proportional to the time difference between start and stop pulses. The analog output pulse is input to a linear biased amplifier incorporated in the TAC, where voltages corresponding to short times may be biased off and the remainder expanded by the post gain factor. By varying the gain on the TAC, the time-to-output voltage coefficient can be varied. All the decay data presented here were acquired using the 100 ns time range, 2.5 V gain, and 1 V bias level setting on the TAC. Therefore, the time range from 10 to 40 ns

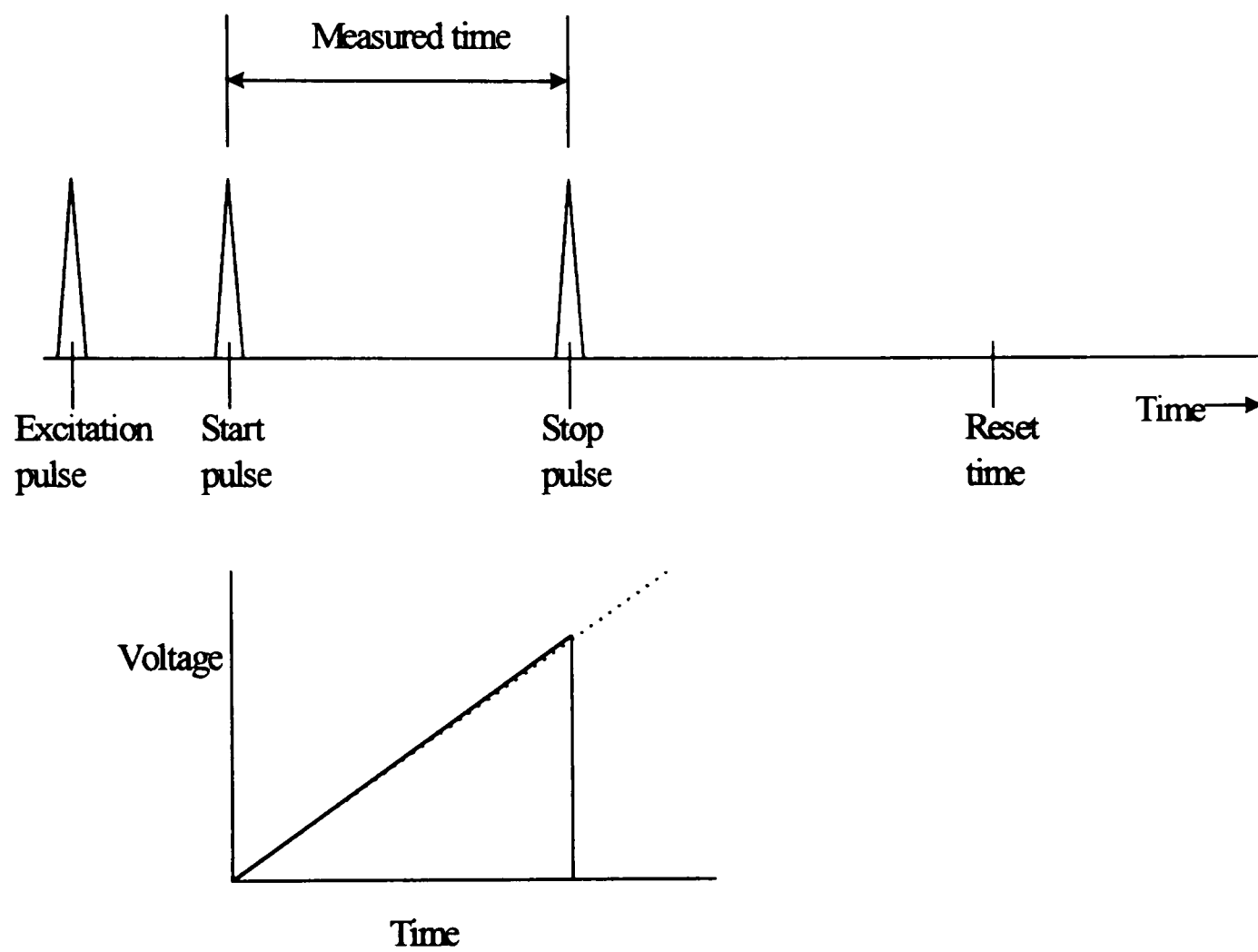


Figure 2.3. Schematic timing diagram showing the function of TAC.

would be identified proportionally with the 0 to 10 V linear output range; thus a 1 V output would identify 3 ns.

The positive output pulses of different amplitudes from the TAC are then scaled and are accumulated by a MCA (Ortec 7010). The MCA consists mainly of an analogue-to-digital converter (ADC), a memory consisting of channels for storing data, and a display unit. The MCA also incorporates discriminators and pulse high analysis (PHA) for data collection. The MCA is operated in real time in order to monitor the accumulation of the histogram of time events. The purpose of the PHA is to bin the individual TAC pulse into one of 4096 channels. The ADC accepts an input pulse from the TAC and measures the peak height of the pulse in digital form. This numerical value is then used to select a memory channel and a count is stored in a channel corresponding to that value. Thus, after a sufficient number of such events, the histogram of number of counts against channel number in the storage device represents the decay curve of the sample. The raw data consist of a record of the number of counts registered in each of 4096 channels.

The time per channel of the MCA is determined by inserting known cable delays between the start and stop inputs of the time to the TAC. The time per channel is chosen to be about 11 ps for all data presented in this work. To avoid bias towards early events after the excitation and pulse pile-up errors, the counting rate for fluorescence must be not more than 1-2 % of the pump repetition rate [98]. The experimental data in the MCA are transferred and then stored in binary form to a computer. This raw data is time inverted as described above and converted to ASCII format in order to analyze the decay data.

The instrumental profile, i.e., the excitation pulse-width broadened by the IRF, was obtained by light scattering from a pure water sample at the excitation wavelength of 305 nm. With the Amperex PMT, on which all the present data were collected, the IRF with a full width at half-maximum (FWHM) of 180 ps was found. This time resolution may be adequate for the studies described here, but future work must employ the faster Hamamatsu tube, now installed. Using an ultrashort pulse and high gain MCP-PMT's which gave about 80 ps response of the system, it was shown that fluorescence decays as short as 10 ps could accurately be measured.

The fluorescence intensity-time profiles of the sample were measured at a specified emission wavelength. The fluorescence lifetimes of excited states of ANS(I) were measured at 460 nm. The fluorescence signals from ANS(II), which is the photoproduct of the fast decay process, exhibit a rise and a fall as we expected. These signals must be collected as far to the red of 560 nm as practicable to avoid contamination from the tail of the emission of ANS(I) species. Intrinsically, then the signals from ANS(I) were noisier and of poorer quality than those from ANS(II). They will be described in Chapter III. Both fluorescence decay and instrument profile were acquired under the same electronic timing conditions insuring that the temporal response of the system remained unchanged. However, since a filter was placed in the emission path of the sample to remove scattered laser light and the monochromator grating was adjusted, the acquired fluorescence decay was slightly shifted in time from the instrument response, due to the different length of the photon travel.

### 2.3 Analysis Method of TCSPC Decay Data

All the fluorescence decay curves of the samples stored in a computer were analyzed by the method of deconvolution as described in Refs. [110-112]. The analysis of the fluorescence decay profile  $I(t)$  of the sample in the picosecond time range is complicated by the finite duration of the light pulse which excites the sample and by the response time of the detection system, both of which cannot be neglected. The decay profile  $I(t)$  acquired in the channels of the MCA is not the actual fluorescence signal emitted by the sample. If the detection system responds linearly, the fluorescence decay emitted by the sample,  $I(t)$ , is obtained as the convolution of the true excited state decay function  $G(t)$  with the instrument response function  $P(t)$ . The convolution integral can be written in the following form [46],

$$I(t) = \int_0^t P(t') \cdot G(t - t') dt'. \quad (2-1)$$

The true fluorescence decay function  $G(t)$  has a form of multiple exponentials. First of all, the task is to evaluate the  $G(t)$ . Using the above equation, the decay parameters, relative intensities and lifetimes, describing the function  $G(t)$  are then extracted by the iterative reconvolution method and nonlinear least-squares curve fitting technique [113].

If  $G(t - t')$  in the above integral is replaced by a delta function  $\delta(t - t')$ , then the measured signal  $I(t)$  is just the IRF  $P(t)$ . Typically, by setting the emission wavelength at the excitation laser frequency, either a mirror or a glass plate is used in place of the sample, which corresponds to replacing  $G(t - t')$  with  $\delta(t - t')$ . Thus, the IRF  $P(t)$  obtained contains the contribution from the excitation pulse, a PMT temporal response,

and other electronics. However, the IRF in this study was obtained by light scattering from the cuvette with a pure water sample because the experimental arrangement should be same in the measurement of both  $P(t)$  and  $G(t)$ . The instrument response and the acquired fluorescence decay data were deconvoluted using an iterative reconvolution technique assuming a discrete number of lifetimes, where the pre-exponential coefficients and lifetimes are varied.

The iterative reconvolution analysis procedures assume that the fluorescence decay  $G(t)$  emitted from the sample is a sum of exponential terms corresponding to emission from  $N$  individual fluorescence transition paths. Data analysis is carried out using a nonlinear least-squares-fitting program based on the Levenberg-Marquardt algorithm [113,114]. The nonlinear least-squares analysis has been suggested by Grinvald [110] as a method of seeking the values of the decay parameters which yield the minimum value of the chi-square  $\chi^2$ . For this analysis, the fluorescence decay function  $G(t)$  is given by

$$G(t) = \sum_{i=1}^N A_i \cdot e^{-t/\tau_i}, \quad (2-2)$$

where the  $A_i$  and  $\tau_i$  are the observed pre-exponential factor and lifetime of  $i$ th component, respectively. Combining this with Equation (2-1) gives the fitting function,

$$I(t) = \sum_{i=1}^N A_i \cdot \int_0^t P(t') \cdot e^{-(t-t')/\tau_i} dt'. \quad (2-3)$$

The fitting program uses a recursive form of the above equation [110]. In the discrete analysis case, both the  $A$ 's and  $\tau$ 's are allowed to vary until a best fit is found. The best fit is obtained when the reduced chi-square error sum  $\chi_r^2$  is minimized, where

$$\chi_r^2 = \sum_{i=1}^n \frac{[I_0(t_i) - F(t_i)]^2}{N_c I(t_i)}. \quad (2-4)$$

Here,  $n$  is a total number of data points and  $N_c$  is the number of degrees of freedom of the fitting function. The  $I(t)$  and  $I_0(t)$  are the raw decay data and the background-corrected data, respectively, and the  $F(t)$  is the fit to the data calculated with the final values of the decay parameters. The  $\chi_r^2$  can be used to provide a measure of the goodness of fit and should be close to 1 for Poisson distributed data [115]. Since a slight non-Poissonian contribution is expected from the noise in TCSPC experiments, good  $\chi_r^2$  values range from 0.8 to 1.2. The usual fitting procedure is finished when the  $\chi_r^2$  did not change by more than  $10^{-8}$  from the previous iteration.

In order to judge the quality of the fit, plots of weighted residuals and the autocorrelation functions have been visually examined along with the  $\chi_r^2$  value. The weighted residual in channel  $i$  is calculated from the following equation,

$$r(t_i) = \frac{I_0(t_i) - F(t_i)}{\sqrt{I(t_i)}}. \quad (2-5)$$

As seen in the above equation, residuals can be defined the difference between the measured decay data  $I_0(t)$  and the fitted data  $F(t)$ . The denominator in Eq. (2-5) comes from the uncertainty in the number of counts in each channel. This is assumed to follow a Poisson distribution with a standard deviation [46],  $\sigma_i = \sqrt{I(t_i)}$ . Residuals from successful fits when plotted against channel number should be randomly distributed about zero. The autocorrelation function of the weighted residual in channel  $i$  is defined [110] as

$$C_j = \frac{\frac{1}{n_2 - n_1 + 1 - j} \sum_{i=n_1}^{n_2-j} r(t_i) \cdot r(t_{i+j})}{\frac{1}{n_2 - n_1 + 1} \sum_{i=n_1}^{n_2} [r(t_i)]^2}, \quad (2-6)$$

where  $n_1$  and  $n_2$  are the first and last channels of the region chosen for analysis. The autocorrelation function  $C_j$  is the correlation between the residual in channel  $i$  and the residual in channel  $i + j$  summed over a selected number of  $i$  channels. The upper limit of  $j$  is set at  $(n_2 - n_1 + 1) / 2$ . For a good fit,  $C_j$  shows high frequency and low amplitude oscillations about zero when plotted against  $j$ .

The above analysis method, which gives the best results [116], is used because it has the following advantages. First, it can account for the scattered light component or time shifts. Second, decay parameters may be easily omitted from the fitting procedure if their values are known. Third, the long tail profile of the excitation light does not affect the analysis. Thus, the fluorescence lifetimes of the excited state ANS were obtained through the standard iterative reconvolution procedure and nonlinear least-squares curve fitting technique described above. With this analysis technique and proper experimental conditions, the TCSPC system could resolve a single lifetime down to much below of FWHM of the IP. A Fortran deconvolution program based on Levenberg-Marquardt's routine [113] has been written and tested with a known lifetime. The program works with the usual DOS operating system and is intended to provide an interactive method for fitting of the decay data. It is also designed primarily for plotting purposes using the PLOT88 software.

CHAPTER III  
EXPERIMENTAL STUDIES OF THE PROPERTIES  
OF INTERFACIAL WATER

The TCSPC apparatus, in combination with a synchronized mode-locked laser pulse and an Amperex PMT, was used to measure the decay parameters of the probe molecule ANS in the reverse micelle (RM) solutions as a function of the size of the RM. The data available from the TCSPC method give us the lifetime constants of the sample fluorescence when repetitively excited by picosecond laser pulses. The analysis technique employed here determines the lifetime distribution for samples and allows us to assess the number of components contributing to the fluorescence decay under study.

By measuring the emission of photons with time, the fluorescence lifetimes include contributions from radiative as well as nonradiative decay rates. Nonradiative channels proposed for the decay of the lowest excited singlet state of ANS are internal conversion, intersystem crossing, photoionization, and excited state charge transfer reactions [51]. The average amount of time that the probe molecule is in the excited state can reveal much about its environment. However, instrumental artifacts would distort the ability to obtain accurate representative decay parameters in such system. One of the most critical artifacts is the wavelength dependency of the IRF [117] because of variations of the transit time spread of the PMT. To avoid the wavelength-dependent problem of the PMT, the IRF and the sample fluorescence should be measured at the same wavelength. Another method would be to use a MCP-PMT as discussed in Chapter II.

The instrumental profile was obtained by light scattering from a pure water sample at 305 nm and had a full-width-half-maximum (FWHM) value of about 180 ps. Samples were placed in 10 × 10 mm spectrophotometer cells (far UV quartz materials by Wilmad) and collected at right angle to the excitation beam in order to eliminate interference from cell window reflections and ensure maximum light transmission. Fluorescence from the cell was focused on the slit of a monochromator equipped with a wavelength drive. The same cuvette was used for both IRF and sample measurements. The proper density filter was put in front of PMT to reduce the fluorescence intensity from the sample so that at most one photon is detected for each exciting event.

All the samples were excited at 305 nm and the fluorescence lifetimes of the excited states of ANS were observed at 460 nm for ANS(I) molecules and at 560 nm for ANS(II) molecules. All experiments were conducted at count rates less than 20 kHz. Thus, the observed sample count rate is held to less than 1 % of the excitation pulse repetition rate in order to minimize pulse pileup [118]. All the decay profiles were acquired over approximately 5 minutes with a peak count of about 1000 counts. Decay lifetimes were obtained by deconvolution of the data stored in a PC.

### 3.1 Experimental Materials

Sodium bis (2-ethylhexyl) sulfosuccinate (AOT) was obtained from Fisher Scientific company. Even though purchased AOT material had 100 % purity, we recrystallized it to remove the impurity present as a result of the manufacturing process such as by-products. However, it is not easy to recrystallize the solid AOT because AOT

has a high melting point above 154 °C. For further purification, the surfactant AOT was dissolved in HPLC grade methanol. The solution was filtered using a funnel and filter paper, and a white residual was discarded. The solvent was then evaporated using Rotavaper-R at 40 °C for 1 day to recrystallize AOT. A white precipitate was obtained, which was dried under vacuum. The purified AOT sample was stored in a vacuum desiccator over P<sub>2</sub>O<sub>5</sub>.

Pure water was obtained from a Barnstead NANO-pure three-cartridge system. The measured resistivity of the filtered water was above 18.0 MΩ·cm. HPLC grade n-heptane was purchased from Aldrich and used without further purification. The probe molecule used here, 1,8-Anilinonaphthalene sulfonate (ANS), was obtained from Fisher Scientific company and was used as supplied. Care was taken to avoid prolonged exposure of the ANS solution to light since it can cause the loss of sulfonate [119] or the yield of bis-ANS [120]. All samples were prepared, stored, and studied at a temperature close to 20 °C. For every experiment, fresh samples were used and sample degradation was not observed over the period of the laser experiment.

### 3.2 Preparation of Reverse Micelle Solution

In this experiment, we varied the water-AOT molar ratio  $w_0$  for each solution. The experimental range of  $w_0$  was chosen from 4 to 35. Below  $w_0 = 4$ , AOT molecules pack and clump unevenly around the spherical core [121]. If  $w_0 > 35$ , the reverse micelle may lose its spherical shape and breakdown. In order to ensure stability in the RM solution [122], surfactant AOT is used in this work because it has low equilibrium

concentrations, which reduces interfacial tension, and it has high flexibility at the interface. In the preparation of RM's, the AOT concentration is maintained at 3 % w/v of the total solution throughout the work.

This work was performed for four different reverse micelle sizes. Since we want to keep the occupancy of ANS in RM's to be less than 1 per RM (for the largest RM studied here, the ANS occupancy per RM is 0.213), sufficiently small concentrations of ANS, about  $2 \times 10^{-5}$  M, were dissolved in water prior to micellization. The ANS solution was stored in the dark because it might deteriorate when it was exposed to light for a long time. To each 100.0 ml of n-heptane was added 3.00 g of the previously purified AOT (M.W. 444.62). The desired range of samples is prepared by adding 0.5, 1.0, 2.0 and 4.0 ml of H<sub>2</sub>O containing ANS to the 100.0 ml AOT/heptane solution. The RM solutions were sonicated using the Ultrasonic Cleaner to mix completely. The molar ratio  $w_0$  in these four samples is 4.1, 8.2, 16.4 and 32.9, respectively.

### 3.3 Results

The fluorescence properties of ANS might be strongly influenced by the nature of its local environment, where ANS is incorporated into the water pool of RM. To explain such result, we must consider the excited state decay processes of ANS and their response to environmental perturbations. The absorption spectrum of a  $2 \times 10^{-5}$  M solution of ANS in pure water was measured with a Shimadzu UV-265 spectrophotometer. As shown in Figure 3.1, the spectrum has a sharp maximum at 265 nm and a broad flat one at around 350 nm, involving the two lowest excited singlet electronic states. When compared with

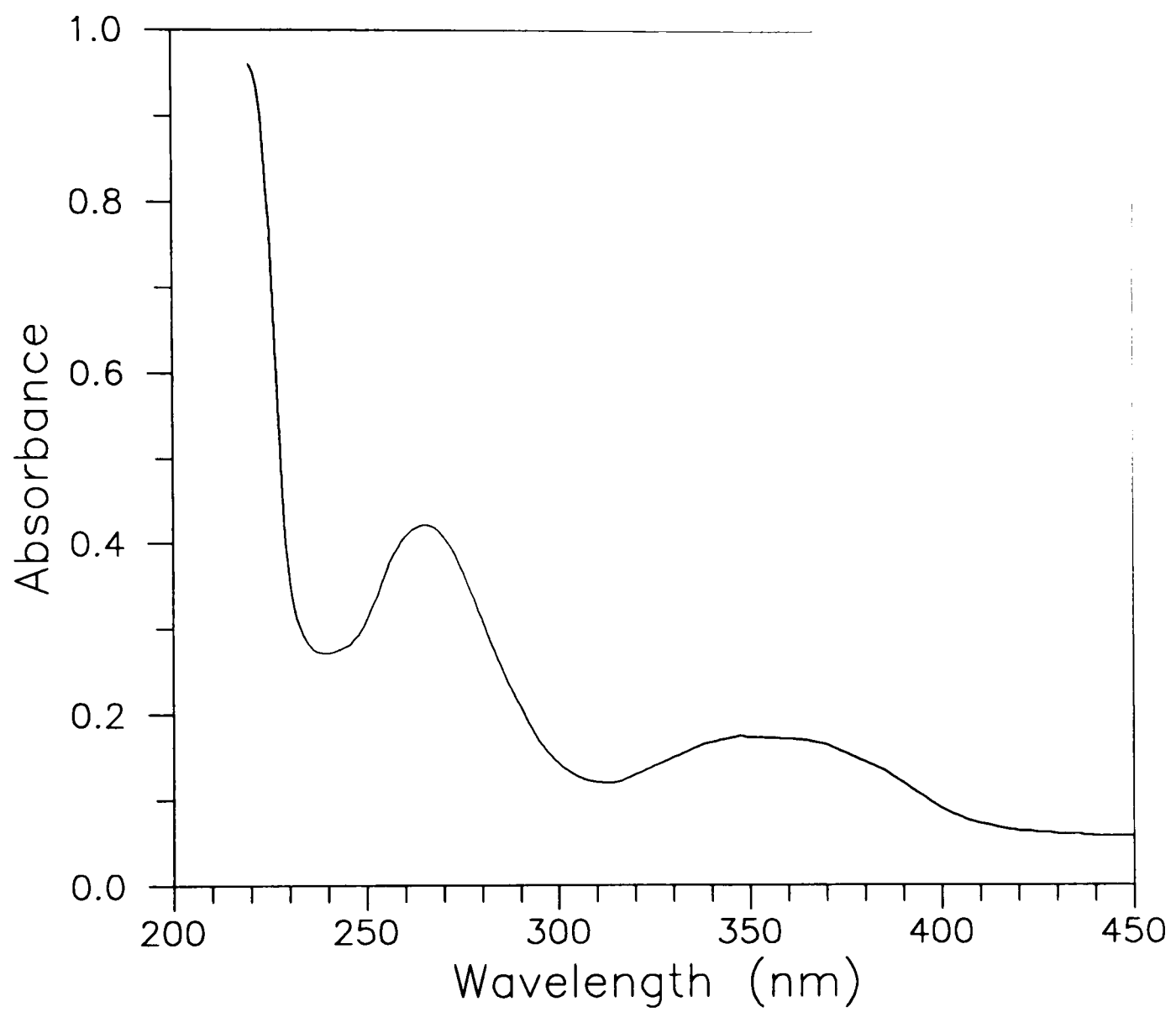


Figure 3.1. The absorption spectrum of ANS in pure water at 25°C.

the solutions in ethanol solvent, it was found that the spectrum is very similar in shape. but it has a blue shift by a small amount.

In a comprehensive study of ANS in H<sub>2</sub>O-EtOH mixed solvents, Robinson et al. [51] found that ANS shows a marked solvent dependence of its fluorescence properties. The fluorescence emission maxima, quantum yields, lifetimes, and radiative and nonradiative rates of ANS in pure water and pure ethanol are summarized in Table 3.1. The absorption and emission spectra of these solvents are very similar, but fluorescence lifetimes and quantum yields are strongly dependent on solvent composition. The emission spectrum in both solvents is red-shifted relative to the absorption spectrum because of the Stokes' shift. This implies that in an aqueous solvent, the excited ANS molecule becomes more polar, resulting in a reorientation of the surrounding solvent molecules. This solvent effect stabilizes the excited state ANS because of a large change in dipole moment between the ground and excited states [58].

Table 3.1. Absorption and Emission Maxima, Quantum Yields, Lifetimes, and Radiative and Nonradiative Rates of 1,8-ANS at 25 °C.<sup>a</sup>

Solvent	$\lambda_{\text{abs}}$ (nm)	$\lambda_{\text{em}}$ (nm)	$\phi_F$	$\tau$ (ns)	$k_r$ (s <sup>-1</sup> )	$k_{nr}$ (s <sup>-1</sup> )
Water	350	523	0.003	0.25	$1.6 \times 10^7$	$4.0 \times 10^9$
Ethanol	360	464	0.41	8.3	$4.8 \times 10^7$	$7.2 \times 10^7$

<sup>a</sup> Sources of data are given in Refs. [51] and [124].

A more interesting result is that ANS shows a large decrease in the fluorescence quantum yields and lifetimes as the proportion of water molecules in the H<sub>2</sub>O-EtOH mixed solvents is increased. It is apparent that the quantum yield  $\phi_F$  derives its strong dependence on the solvent composition both from a decrease in the radiative rate  $k_r$  and an increase in the nonradiative rate  $k_{nr}$ . One plausible explanation of this solvent effect suggested by Fleming et al. [125] is that one-photon ionization in aqueous solution is an important nonradiative pathway for the excited state ANS. Therefore, the nonradiative transition would be expected to favor the charge-transfer-to-solvent (CTTS) process in an aqueous solvent, while intersystem crossing to a triplet state is favored in a non-aqueous solvent environment [51].

The lifetime of the excited state of ANS(II) in pure water was measured at the emission wavelength of 560 nm. The fluorescence decay profile of ANS(II) together with the excitation pulse is displayed over 1000 channels in Figure 3.2. All the decay data presented in this work have 11 ps per channel number. The solid line represents the fitted curve with a single exponential function to the decay profile of dotted curve and the narrow peak to the left is the instrument response function. The weighted residuals are plotted over the range of the fit and autocorrelation function  $C_r$  of the residuals is plotted over one half the range of the fit. The resulting  $\chi_r^2$  is 1.97, which is larger than the usually accepted value, mainly due to the rising portion of the decay curve. The result is a good fit to the acquired data as it is shown from the flat weighted residual plot and the low amplitude autocorrelation plot. The lifetime of ANS(II) obtained here is 280 ps, compared

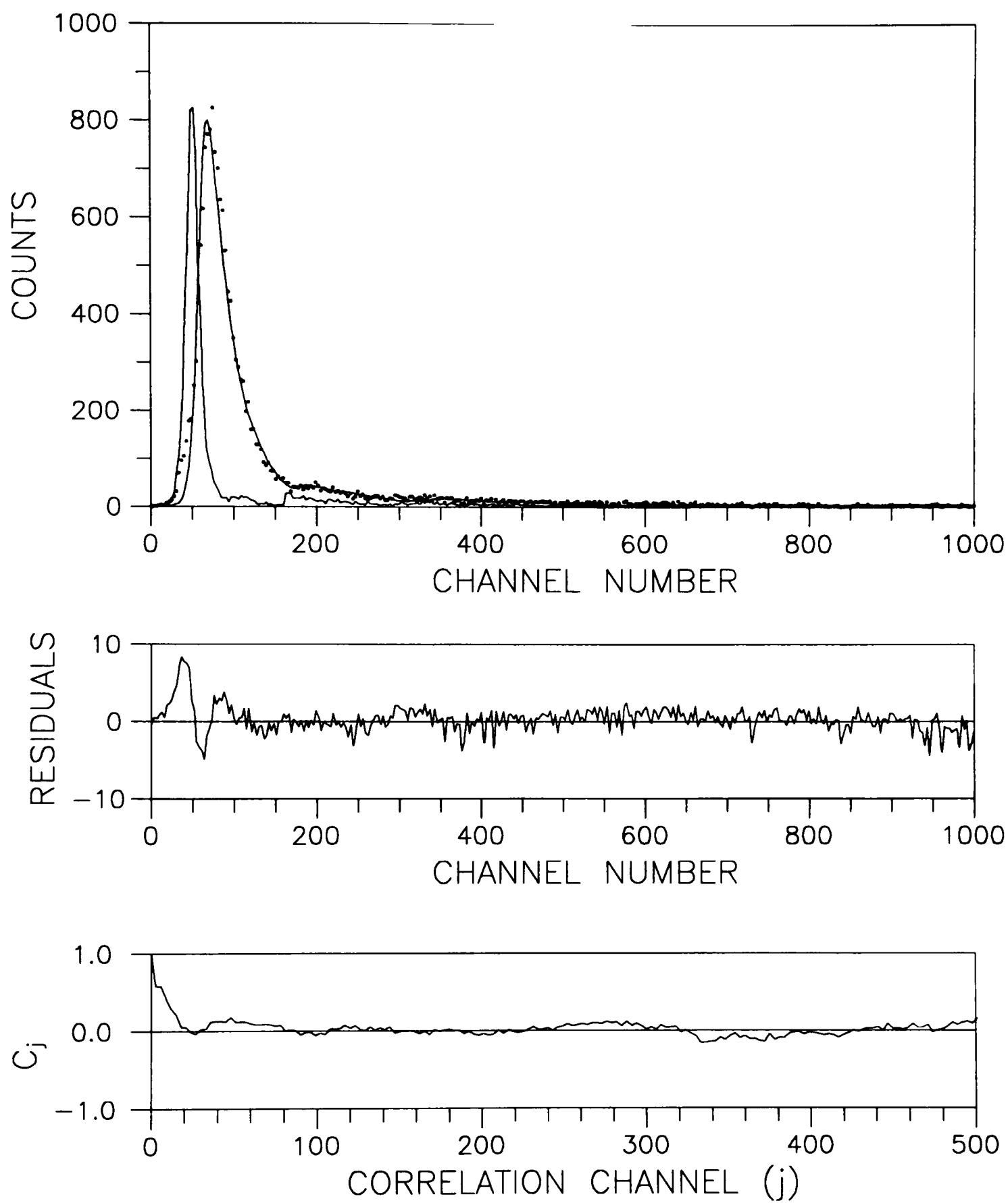


Figure 3.2. Fluorescence decay profile with single exponential fit, attributed to the ANS(II) in pure water.

with 250 ps for emission at 523 nm as determined by Robinson et al. [51] using a Nd:glass laser. This fast decay process may occur primarily through the excited state of ANS(II) created by photoionization of ANS(I) to solvents [125].

### 3.3.1 Decay Profiles from the ANS(II) Molecules

In the water/ANS/AOT/heptane experiments, the excited state lifetime and diffusion times of the probe in the RM water pools seem to have somewhat similar magnitudes. The rates are neither reaction controlled nor diffusion controlled. Under such circumstances, nonexponential decays would be expected. In fact, in preliminary experiments [11], nonexponential decays have been observed in a number of similar confined volume systems, such as controlled pore glass, quartz surfaces, and the air-water interface.

The fluorescence decays for the ANS(II) in the various RM solutions were obtained at 560 nm, which is far from the emission maximum for the ANS(I). The results of decay profiles for the four different RM samples as a function of  $w_0$  are given in Figures 3.3-3.6. Each decay curve acquired was individually deconvoluted with a single exponential fitting function to determine its corresponding lifetime. For all decay curves, the solid line represents the fitted curve and the dotted one is the experimental decay curve. The quality of the fit can be assessed visually from the residual plot and the value of  $\chi_r^2$ . The reason for the large value of  $\chi_r^2$  and the large oscillation of residuals at the sharp rising part of decay curve is due to the different emission paths when acquiring the IP and sample fluorescence as previously discussed in Chapter II. The autocorrelation plot

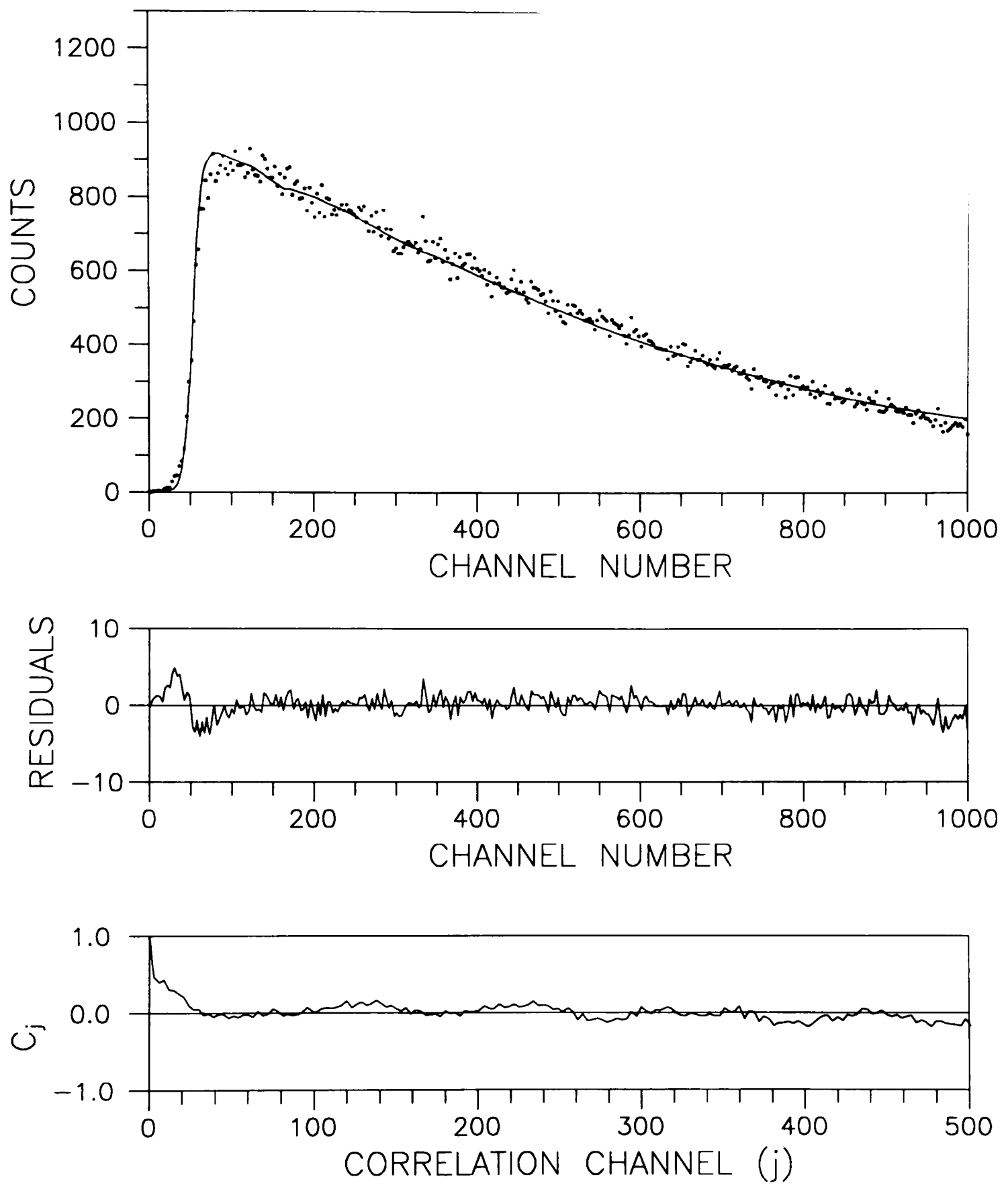


Figure 3.3. Fluorescence decay profile with single exponential fit, attributed to the ANS(II) for  $w_0 = 4.1$  at 560 nm.

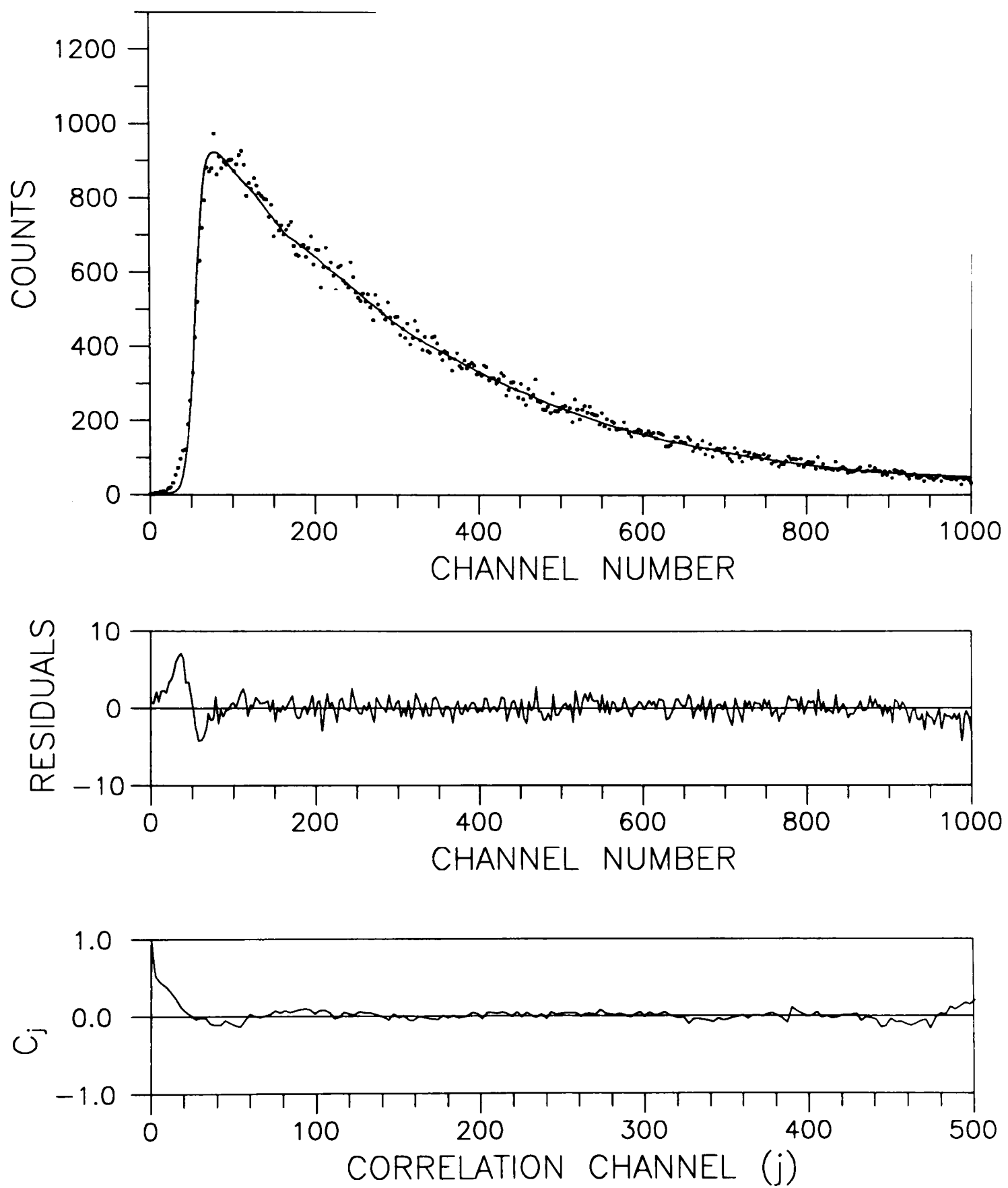


Figure 3.4. Fluorescence decay profile with single exponential fit, attributed to the ANS(II) for  $w_0 = 8.2$  at 560 nm.

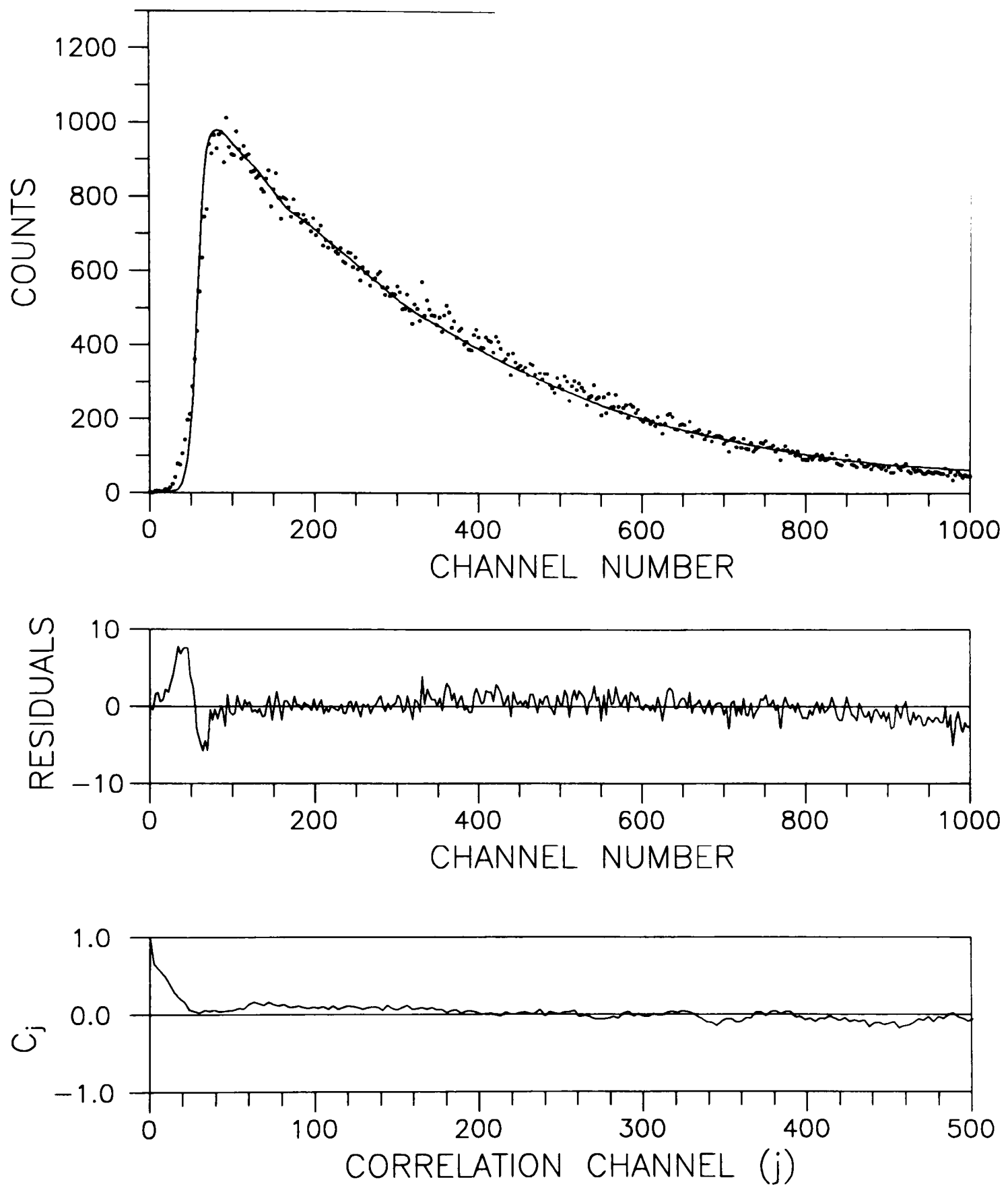


Figure 3.5. Fluorescence decay profile with single exponential fit, attributed to the ANS(II) for  $w_0 = 16.4$  at 560 nm.

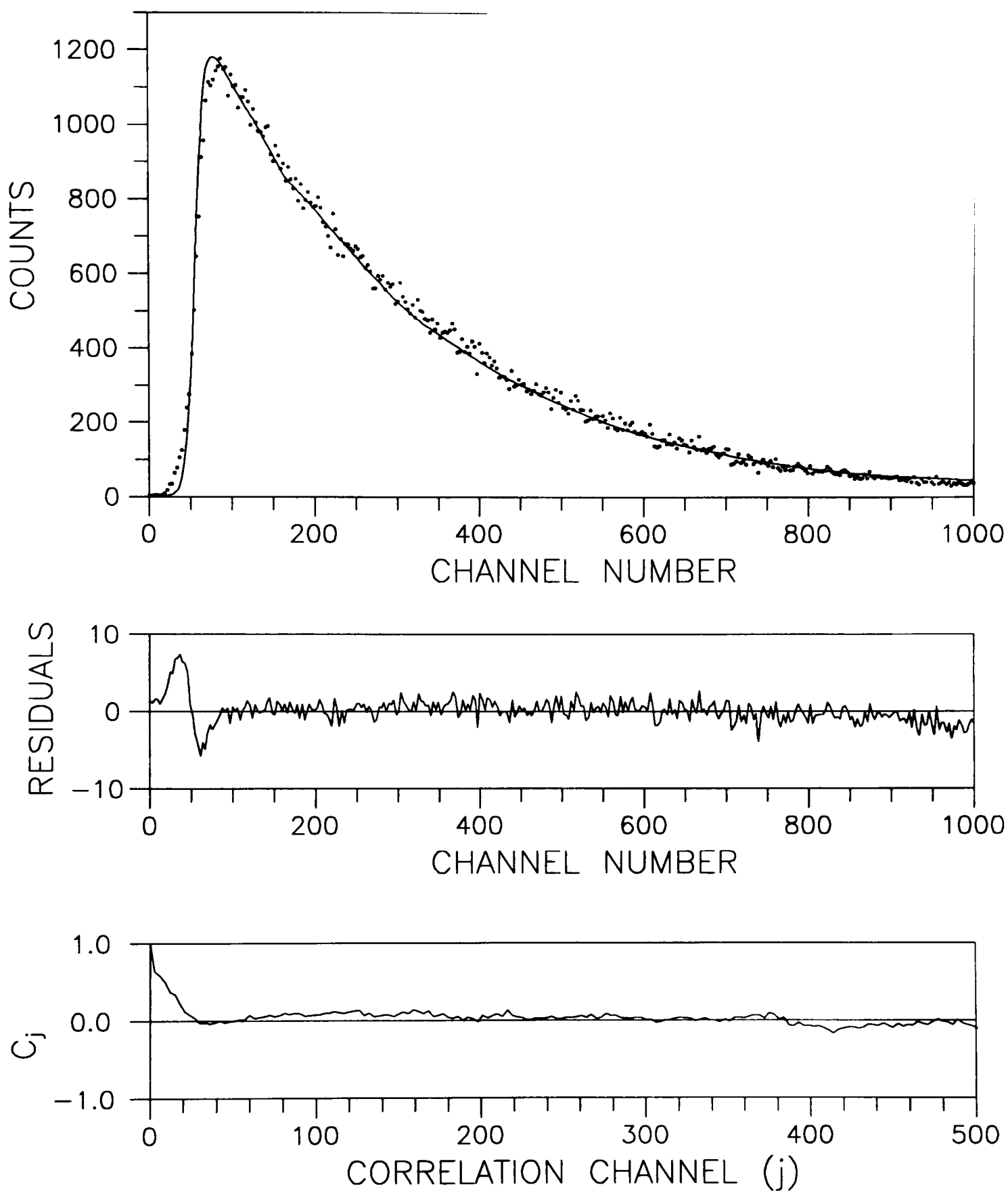


Figure 3.6. Fluorescence decay profile with single exponential fit, attributed to the ANS(II) for  $w_0 = 32.9$  at 560 nm.

also shows a large deviation at the lower correlation channels. The decay curves have a broad peak at the early decaying part, but it becomes more sharp with increasing  $w_0$ . All the fitted curves presented here show wiggles during their decay because of the deconvolution with the rough tail of the IRF, which is not smooth, as shown from Figure 3.2. In addition, the distortion during the rise portion of the curve may be caused by the time-dependent Stokes' shift.

Table 3.2 lists the results in the lifetimes of the ANS(II) as a function of  $w_0$  when the experimental decay profiles are fitted by a single exponential. The value of  $\chi_r^2$  increases while the lifetimes decrease with increasing  $w_0$ . This decrease in the lifetimes is probably due to the increasing percentage of ANS near surface, which can be attributed to environment differences within the RM water pools. From the bi-exponential fitting, we could barely resolve two component lifetimes. A small contribution from one component, especially at the higher  $w_0$ , indicates that the environment for ANS is also changing by a different decay route. At lower  $w_0$ , where most solvent molecules are supposed to bound to the interface, the lifetime for ANS(II) approaches that in ethanol solvent.

### 3.3.2 Decay Profiles from the ANS(I) Molecules

The fluorescence decay of the ANS(I) in RM solutions can be described by a sum of discrete exponential decay components or by a distribution of lifetimes. However, single exponentials might provide a good fit to the data if there is a small spread in the rate constants, or if the instrumental response is too slow, and/or if the various domains

Table 3.2. Single Exponential Fitting Parameter for Emission at 560 nm, Attributed to the ANS(II).

$w_0$	$\tau$ (ps)	$\chi_r^2$
4.1	5170	1.65
8.2	2685	2.13
16.4	2806	2.97
32.9	2269	2.67
pure water	280	1.97

intermix by a process such as diffusion on time scales much faster than the decay times [48]. While the decay data from the ANS(I) cannot be fit accurately by a single exponential, they can be fit by a double exponential with a small fitting error.

Even though theoretically expected to be multi-exponential, the decay data can indeed be fit reasonably well to a bi-exponential. Figures 3.7-3.10 represent the acquired decay curves for the various RM samples and their corresponding fitted curves assuming two discrete exponentials. In all cases, the fit over the decay curve is smooth as indicated by the residual pattern and autocorrelation function,  $C_r$ . The peak count is on the order of 1200, much higher than typically acquired from the ANS(II).

The standard errors are quite large for some of the decay curves. The greatest deviation between the observed and fitted functions occurs on the rising portions of the curves, which makes a large difference in the quality of the fit. It is apparent from the weighted residual plots of each of these figures. This behavior is quite general when lifetimes are measured by the technique described in Chapter II. An immediate improvement in  $\chi_r^2$  was obtained if the analysis is restricted to the decay side of the profile.

The fitting parameters and  $\chi_r^2$  for the bi-exponential fits for the various RM solutions are given in Table 3.3. It is noteworthy that in the small RM's, where there is a greater surface to volume ratio, the percentage intensity of the long-lived component ( $I_2$ ) is larger, as it would be expected to be. It is also important to note that there is a general decrease of the apparent lifetimes of both the short ( $\tau_1$ ) and long ( $\tau_2$ ) components as the

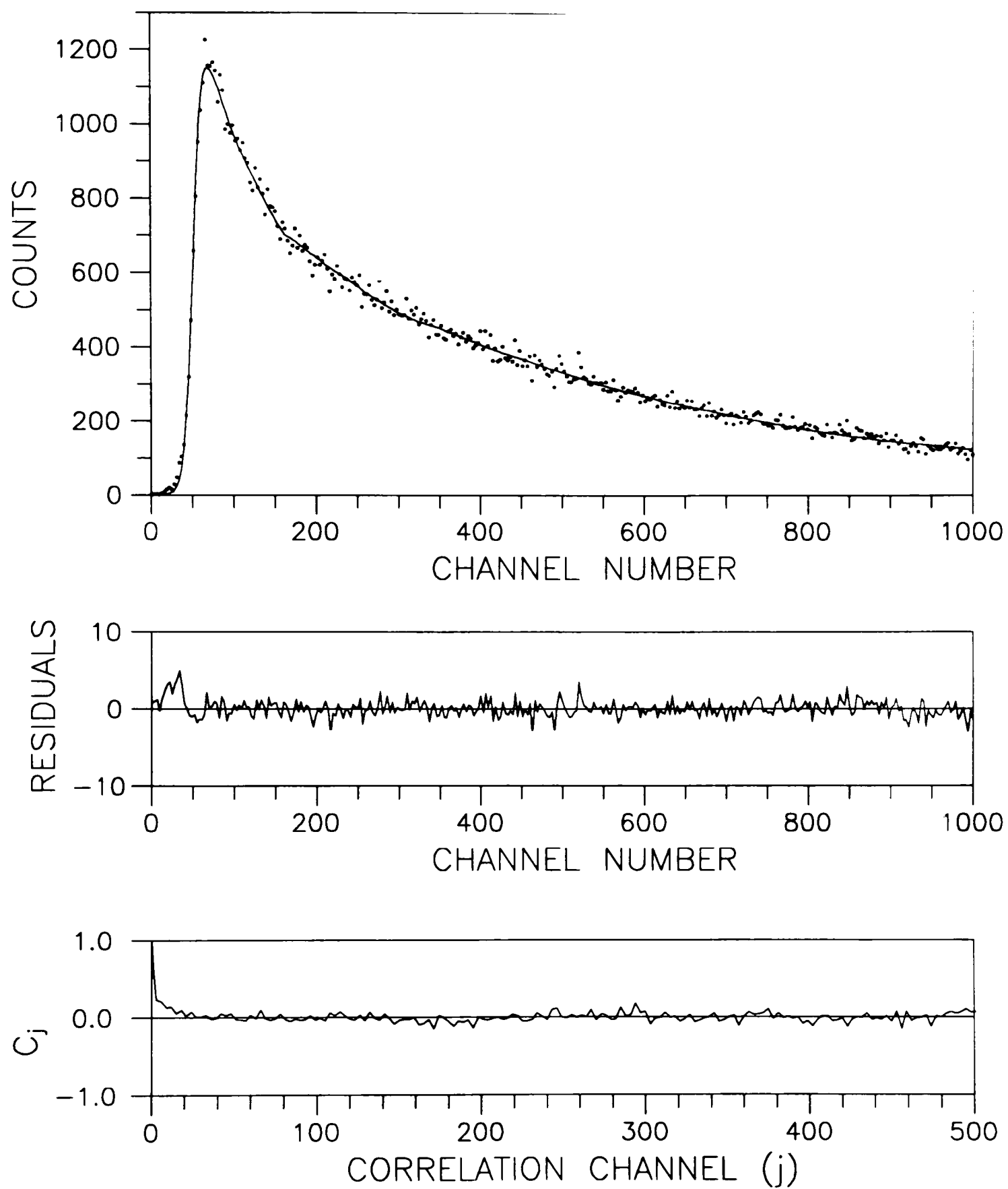


Figure 3.7. Fluorescence decay profile with double exponential fit, attributed to the ANS(I) for  $w_0 = 4.1$  at 460 nm.

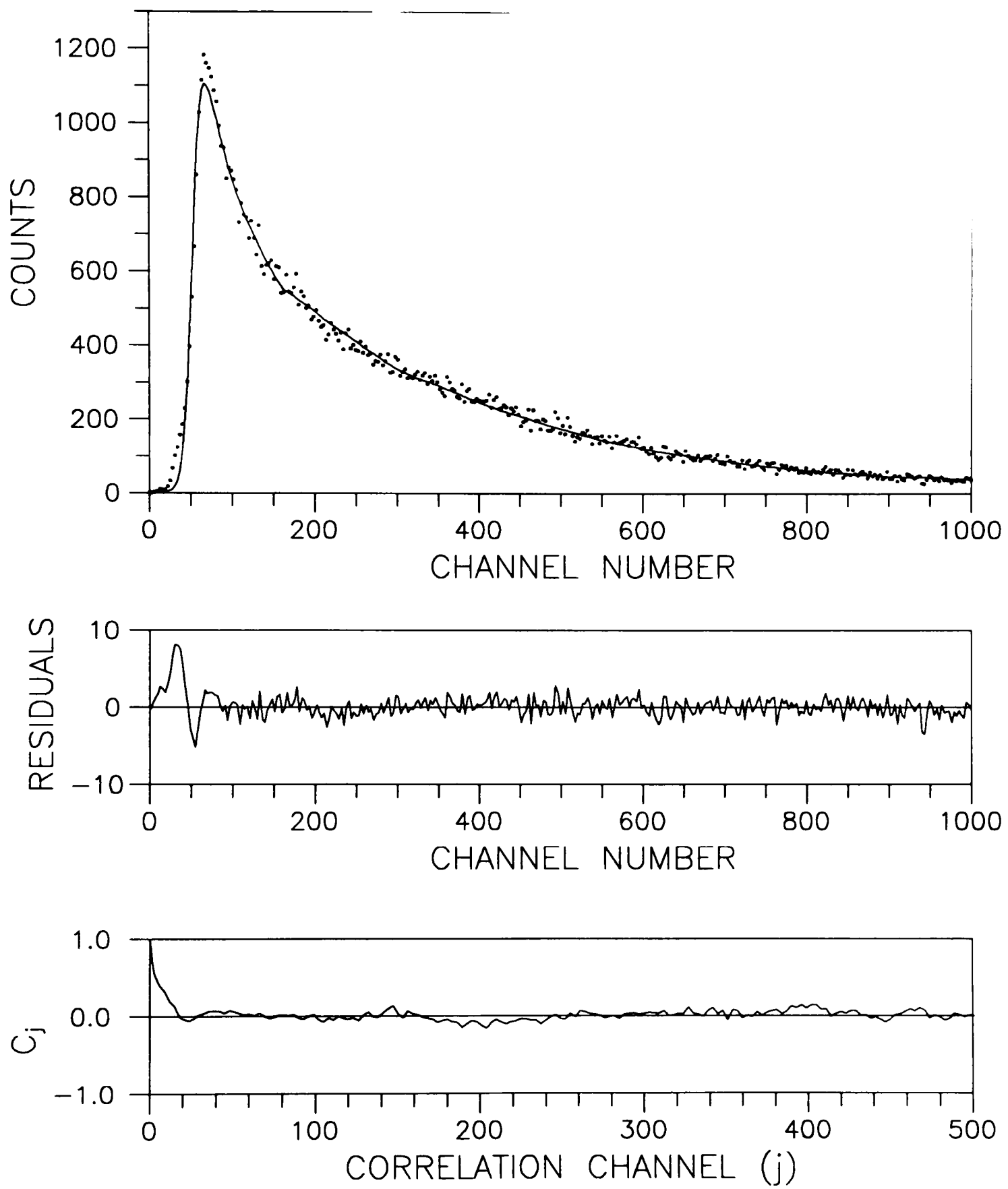


Figure 3.8. Fluorescence decay profile with double exponential fit, attributed to the ANS(I) for  $w_0 = 8.2$  at 460 nm.

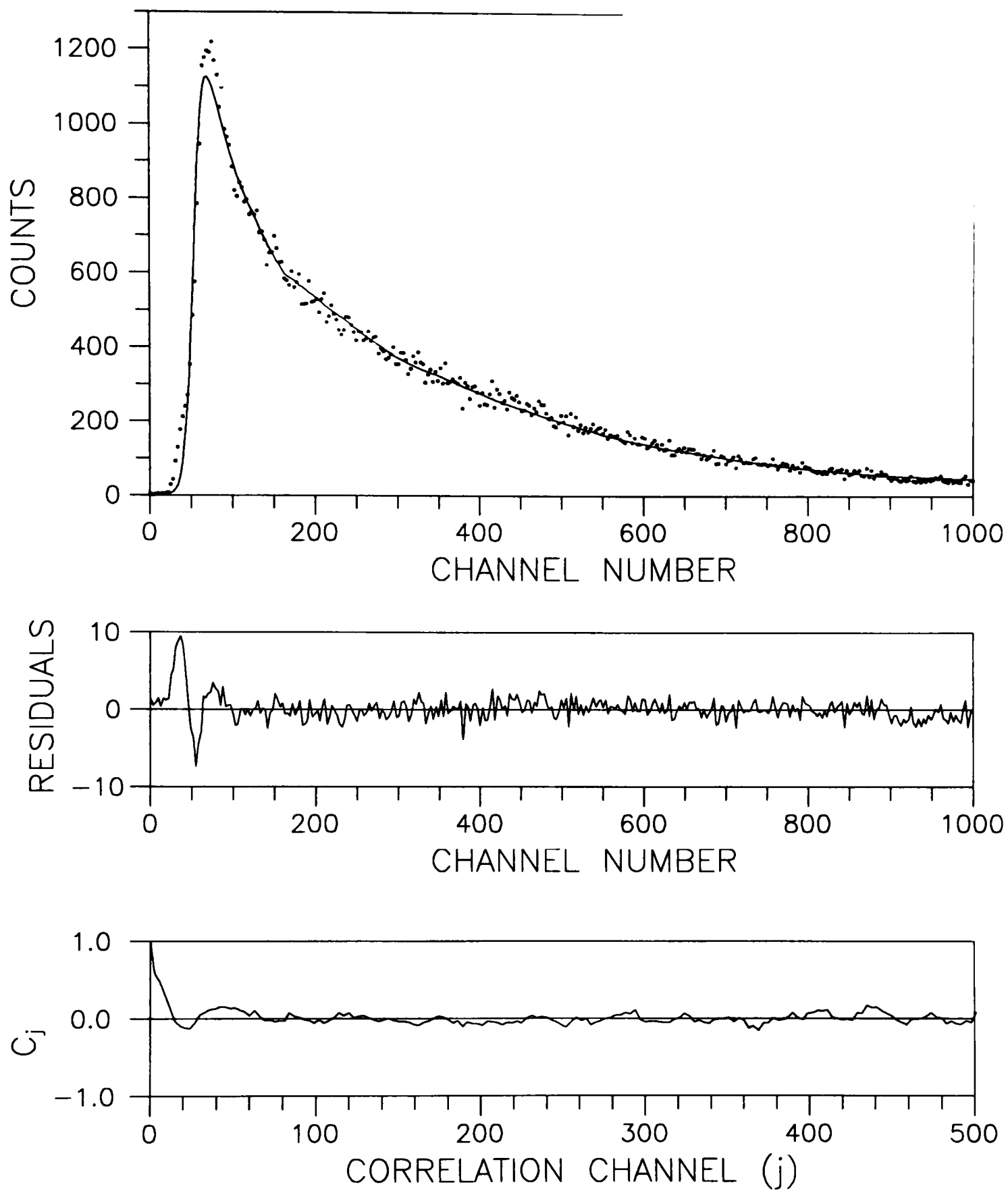


Figure 3.9. Fluorescence decay profile with double exponential fit, attributed to the ANS(I) for  $w_0 = 16.4$  at 460 nm.

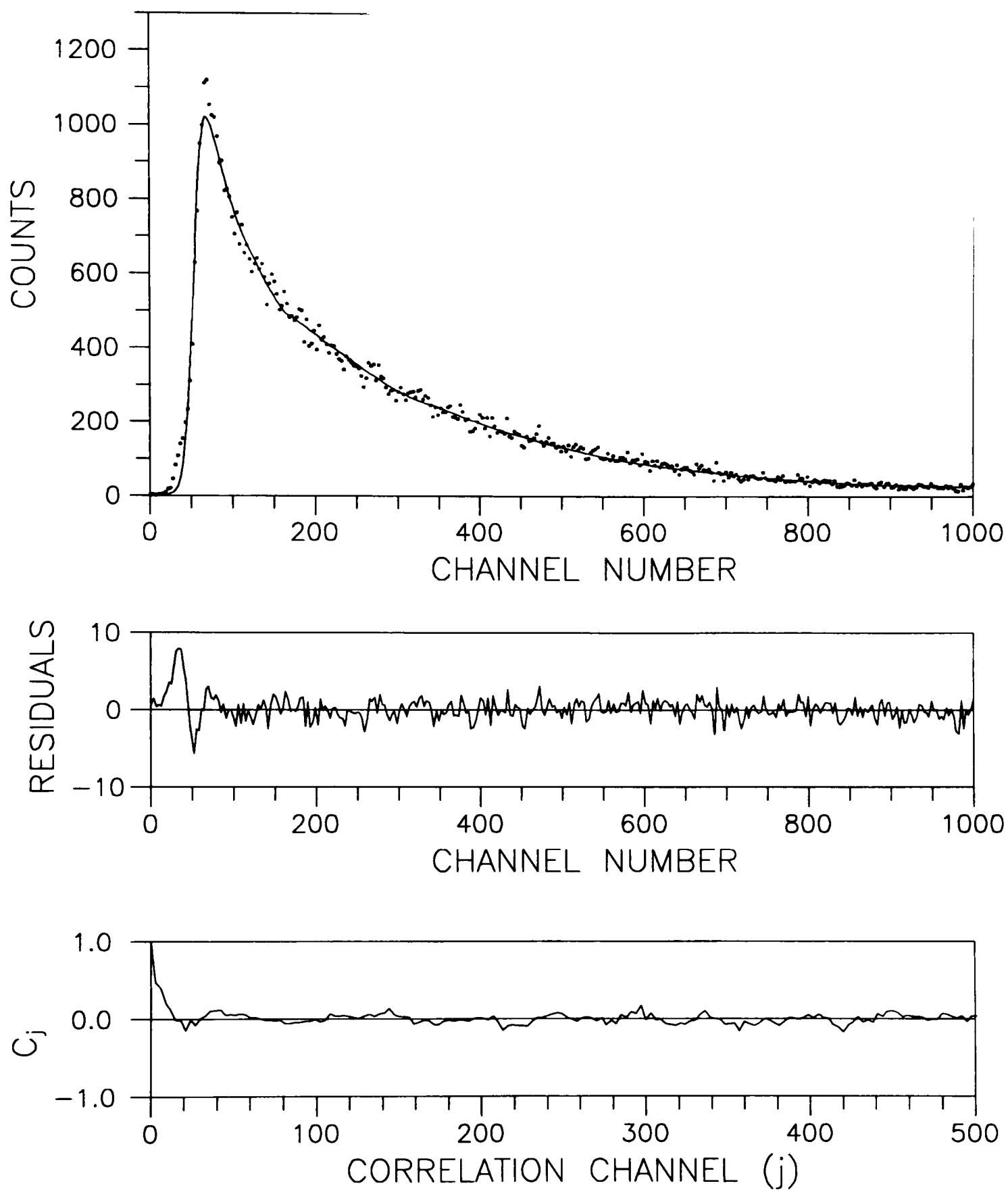


Figure 3.10. Fluorescence decay profile with double exponential fit, attributed to the ANS(I) for  $w_0 = 32.9$  at 460 nm.

Table 3.3. Double Exponential Fitting Parameters for Emission at 460 nm, Attributed to the ANS(I).

$w_0$	$\tau_1$ (ps)	$I_1$ (%)	$\tau_2$ (ps)	$I_2$ (%)	$\chi_r^2$
4.1	640	36	4703	63	1.28
8.2	413	41	2648	59	2.31
16.5	444	43	2765	57	2.75
32.9	373	49	2211	51	2.40

RM's become larger, showing an absence of two fixed lifetimes with varying relative weights. There is clearly the general trend that the shorter component increases the fluorescence decay compared to the long component by going from lower to higher  $w_0$  samples. This indicates a shift of the overall lifetime distribution toward shorter lifetimes, i.e., towards the 280 ps found in pure water, which corresponds to the increasing percentage of ANS(II) in a more aqueous environment.

In particular, not observed in the fluorescence experiments is the picture used to describe NMR proton chemical shifts  $\delta$  in these systems [35]: one long-lived component representing bound water, and one short-lived component representing free water, each having varying weight as the surface-to-volume ratio decreases with increasing RM size. A two-state model based on bound and free water molecules does present an enigma, since intuition dictates that there is very likely a gradual change of water properties from the periphery to the center of the RM. A similar conclusion for ionic solutes has been reached by Enderby [126]. There is no sharp boundary on structural features.

#### 3.4 Discussion

We have shown that our TCSPC system did not work very well in collecting the fluorescence signals from the ANS(II), which is presumed to have more than two components making up the fluorescence emitted, associated with the nonradiative photoionization of ANS(I). When trying to fit those decay functions with multi-exponentials, especially bi-exponential, the fit for higher  $w_0$  shows that the percent contributions of one of the components are negligible. For lower  $w_0$ , the calculated

lifetimes of the bi-exponential fit turn out to be nearly equal, so that the decay profiles are really fitted by a single exponential. This indicates that the fractional fluorescence intensity of a fast decay process, as we expected, may not be detectable since the system used was not sensitive enough to detect the very low emission from samples. Comparison of the ANS(I) and ANS(II) decay curves demonstrates similar lifetimes for the long-lived components. These observations indicate that the signals from ANS(II) could be greatly contaminated by the tail of the emission for the ANS(I).

In the RM system, because of orientational constraints, bound water [35] near the hydrophilic interface is very likely incapable of participating in the fast decay process. Consequently, the lifetime of the ANS molecule in such an environment is very long compared with its lifetime in bulk water. Furthermore, at different distances from this surface there must be a series of different environmental domains in which the ANS molecule can reside, and each of these domains suffers a different perturbation. Thus, each domain gives rise to a different exponential lifetime. The sum of such a series of exponentials will seldom appear as a single exponential decay. The short-lived components at short times and the long-lived components persistent at long times are incompatible with such a decay. An excellent discussion of multiple exponential decays and related points has recently been presented by Toptygin et al. [127]. It is also known that the small number of exponentials required to fit a fluorescence decay can cover complex distributions of lifetime [128].

Whatever the physical origin of these complex decays, the double-exponential analysis from the ANS(I) can be used to study the RM environment. As seen in Table 3.3,

the longer lifetime increased markedly when the solvent is close to the interface, ranging from 2.2 ns at  $w_0=32.9$  to 4.7 ns at  $w_0=4.1$ . These striking changes in the decay data imply that its environment differs greatly in the near interface. The lifetimes for RM's presented here can be studied using an analytical method to eliminate one important fitting parameter.

It is not possible to rule out some repulsion of the probe (or active site in the probe) by the surface, but nothing like complete absorption of the probe to the surface was indicated. This conclusion can be reached merely through a qualitative examination of the decay curves in Figures 3.7-3.10 or the bi-exponential parameters in Table 3.3. The more rapidly decaying initial component, even in the smallest RM, indicates that the probes have some propensity to be found in the central regions of the RM's, where the decay rates are faster; the slowly decaying tails show that the probes also may reside in the vicinity of the surface. Note, in particular, that the tails progressively rise as the micelle size decreases. The gradual transition between these two extremes in the various RM's, as evidenced again from the double and triple exponential fits, means that intermediate situations are present and the best fits for fewer exponential decay terms are clearly not satisfactory in this RM.

Certainly, the rate would be expected to increase towards the fast decay time of 280 ps as the center of a large RM, with increasingly bulk-like water properties, is approached. What are the expectations about the diffusion coefficients? It is an unresolved question whether a dissolved molecule in confined water diffuses faster or slower than that in bulk water. Molecular dynamics (MD) simulations of various liquids

near simple surfaces have presented a mixed picture. For a Lennard-Jones fluid [16], diffusion perpendicular to the surface is retarded because of particle reflections from the surface, which cause a faster decay of the velocity autocorrelation function. However, for a flexible/polarizable rigid plate [15], MD indicates that both perpendicular or tangential diffusion rates are only mildly enhanced. Karim and Haymet [19], using a rigid non-polarizable MD model for water, also report negligible perturbations on diffusion near the ice-water interface. MD for water near the air-water interface [20] shows larger effects, which indicate faster diffusion perpendicular to the surface than tangential to it. Noteworthy, however, in all these MD simulations is that there are no ionic interactions. In contrast to the above findings, MD simulations [129] of water near a more realistic RM-like surface have indicated a stronger perturbation on diffusion.

The shortest lived component from a fast decay process cannot be observed at 560 nm, probably due to the limitation of the our TCSPC system. In other words, this very fast process was not within the resolution limit of the system. It was determined that a more sensitive system was necessary to resolve the observed fluorescence with a very short lifetime component. The new MCP-PMT has been installed and a total instrument response of 80 ps has been measured. However, the fast response of the PMT and amplifier may be limited by devices which follow, i.e., the CFD or TAC. The use of better timing units can improve the instrument response much below 80 ps.

CHAPTER IV  
ANALYTICAL METHOD FOR INTERPRETING  
THE PROPERTIES OF AN INTERFACIAL WATER

It has been suggested that the fluorescence decay of a probe molecule ANS confined in the RM solution cannot be characterized simply by a single exponential decay law. This means that the fluorescence decay of ANS should be described as a continuous distribution of lifetimes, each of which corresponds to a different environment. This different lifetime distribution is interpreted by the environmental effect on a photophysical process of the probe molecule, each with its own set of lifetimes [130,131]. Some research works from both electron and proton rates in charge transfer reactions, in which charge transfer quenches the fluorescence, have shown that water clusters may also play an important role in the photophysics of the excited state of a molecule [132].

Although experimental models have been used to study the origin of lifetime distributions by the expected heterogeneity of the environment in the RM water pool, no quantitative methods for analyzing such data have been available. By using certain kinetic parameters, it is possible to construct a physical model that takes into account the photophysical processes of the fluorescence decay of ANS in a confined system and to provide new insights into the properties of interfacial water. In this study, an analytical method will be constructed and used to obtain a realistic and informative fitting procedure that takes account of the expected continuous distribution of lifetimes from the decay curves.

All the analysis done in this chapter will be based on the main photophysical processes associated with the excited states of ANS, assuming that the fluorescence decay is followed with some decay routes. Before presenting the analyzed data, it is important to understand the structure of the RM and the photophysical basis for the model used, and to detail the analytical procedure used in determining the various parameters.

#### 4.1 Reverse Micelle Structure

The hydrophilic interface in these RM's is made up of the AOT head groups, containing dissociable ionic charge ( $\text{Na}^+$ ). The overall outside radius of these RM's can range up to about 100 Å. The size of RM's depends on the mole ratio  $w_0$  of water to AOT: about 4:1 to produce 25 Å radius RM's and about 30:1 for 60 Å radius RM's. The inside radii  $r_w$ , i.e., the radii of the encapsulated water pools in the 25 Å and 60 Å radii RM's, are 10 Å and 50 Å, respectively. These water pools are thus convenient for studying biological relevant perturbed water in confined volumes of an extremely small but fairly well defined size.

In this analytical method, the sizes of RM's will be considered up to about 60 Å radius because they tend to be nonspherical when their radii become larger than 60 Å, and further increasing their size much beyond 100 Å, they become unstable [133]. The radius of the water region can thus vary within the range 10-60 Å and then the size of the entire RM ranges from 25-76 Å. Smaller RM's exist, but the water pools within them, as well as the head group packing, seem defined differently than in the larger water pools.

Figure 4.1 shows a schematic cross-sectional picture of the water pool in the RM, which is divided into spherical shells or zones (Z's), whose midpoints lie at different distances from the surface. Except perhaps for the special zone (SZ), all the zones have equal thicknesses, chosen to be approximately 2.0 Å in order to attempt to keep an equivalent level of spatial resolution. The thickness of the zone chosen here is less than the diameter of a water molecule, which is about 2.8 Å [2].

If it is assumed that all the AOT molecules take up a constant area at some fixed distance beyond the radius of the water pool, the inside radii  $r_w$  in Å can then be obtained using the following surface and volume relationships:

$$4\pi(r_w + \alpha)^2 = \bar{n}A \quad (4-1)$$

and

$$\frac{4\pi}{3} r_w^3 = 29.97 w_0 \bar{n}, \quad (4-2)$$

where the quantity  $29.97 \text{ \AA}^3$  is the average volume of a water molecule in the normal liquid at 20°C,  $\bar{n}$  is the number of AOT molecules per RM, and  $\alpha$  is a fixed distance outward from the water pool surface where each AOT head group is assumed to occupy a constant area  $A$ . Eliminating  $\bar{n}$  from the above two equations (4-1) and (4-2), one finds the following relationship between  $r_w$  and  $w_0$ :

$$\frac{r_w^3}{(r_w + \alpha)^2} = 89.91 \frac{w_0}{A}. \quad (4-3)$$

To find the constants  $\alpha$  and  $A$ , we examine the data of Eicke et al. [34,133] as quoted by Maitra [35], assuming the isooctane primary solvent used by them and the n-heptane

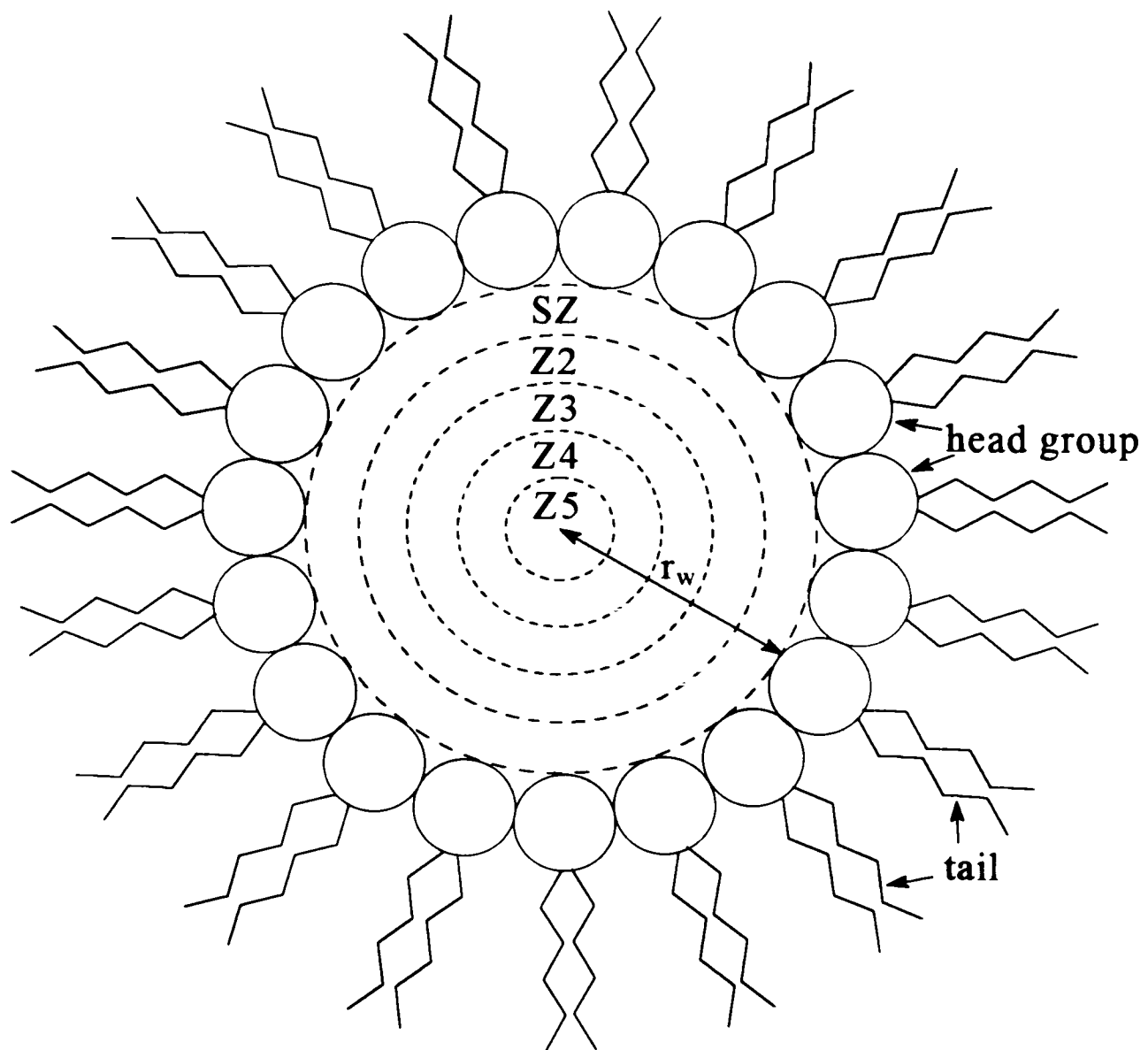


Figure 4.1. Schematic cross-sectional diagram of the reverse micelle of AOT. The size of RM is exaggerated to illustrate its structure for analysis purpose. There are four inner zones and one special zone (SZ) for the 10 Å RM.

solvent used by us behave the same way with respect to these constants. The effect of this assumption on our calculation is unknown. Except for the smallest RM ( $w_0 = 4.1$ ), where we suspect tighter AOT packing, we find  $\alpha = 2.3 \pm 0.2 \text{ \AA}$  and  $A = 58.2 \pm 0.5 \text{ \AA}^2$  from the range of  $w_0 = 6.0 \sim 35.0$  in the Table I of Ref. [35]. To determine the sizes of the resulting water pools, these two constants are used to solve for  $r_w$  of the equation (4-3). For the four different RM's, the values of  $r_w$  are 9.7, 16.5, 29.5 and 55.2  $\text{\AA}$ , respectively, which agree well with interpolated values [35]. For the smallest RM, where more dense head-group packing destroys the constancy of  $\alpha$ , we use  $r_w \approx 10.0 \text{ \AA}$ . Table 4.1 gives the  $r_w$  values together with relevant physical properties of these four different reverse micelles. The  $r_w$  increases linearly as  $w_0$  increases. In general, with the addition of water, the number of reverse micelles decreases as their sizes increase because the number of AOT molecules remains constant.

We calculate the  $\bar{n}$  from the equation (4-1) and the total number of water molecules  $n_w$  in the RM using  $\bar{n}w_0$ . To estimate the number of bound water  $n_B$ , we use the mole fraction of bound water  $P_B$  from NMR experiments [35]. The mathematical expression of  $P_B$  defined by Maitra is given by

$$P_B = 1 - \left(1 - \frac{d}{r_w}\right)^3, \quad (4-4)$$

where  $d$  is the thickness of the bound water layer. We found  $d = 4.0 \pm 0.3 \text{ \AA}$  using the same data as used to find  $\alpha$  and  $A$  values. Once the values of  $P_B$  and  $\bar{n}$  are known, a

Table 4.1. Some Physical Properties of the Reverse Micelles Used in This Work.

$w_0$	$r_w$ (Å)	$N$	$\bar{n}$	$n_w$	$P_B$	$n_B$
4.1	10.0	5	34	139	0.78	109
8.2	16.5	8	77	628	0.56	352
16.4	29.5	15	219	3588	0.35	1256
32.9	55.2	28	715	23508	0.20	4702

$w_0$ : the molar ratio of water to AOT.

$r_w$ : the radius of the encapsulated water pools.

$N$ : the number of zones.

$\bar{n}$ : the number of AOT molecules per a RM.

$n_w$ : the total number of water molecules.

$P_B$ : the mole fraction of bound water from NMR experiments [35].

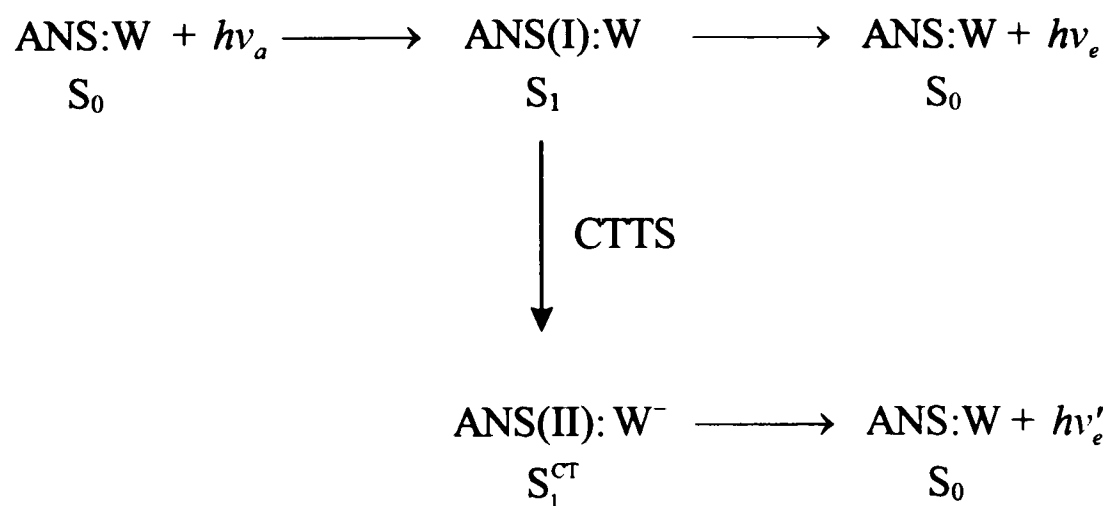
$n_B$ : the number of bound water molecules.

straightforward calculation of the  $n_B$  can be made from the equation,  $n_B = w_0 \bar{n} P_B$ . The number of zones ( $N$ ) along with  $r_w$  is ultimately used as input parameters in the proposed analysis method.

#### 4.2 Probability Kinetics

As emphasized previously, the emission properties of the probe molecule ANS are sensitive to solvent composition in the excited state and its environment. The excited ANS molecules in water/alcohol mixtures have shown that the nonradiative rate increased with increasing the dielectric constant of solvent by an order of magnitude on going from water to ethanol [51,125], see Table 3.1. This result indicates that the lack of fluorescence of ANS(II) in aqueous solution is due to rapid photoionization from the singlet state of ANS(I). After the formation of charge transfer to solvent (CTTS), the nonradiative transition, which is the fast decay (FD), occurs.

On the basis of the above information, the theoretical description of the ANS photophysics may be proposed by the following kinetics model,



where W labels the surrounding solvent molecules. After absorption of a photon ( $h\nu_a$ ), the excited state of ANS(I) may be depopulated either by emission of light ( $h\nu_e$ ) or by means of a CTTS nonradiative quenching process, resulting in the production of ANS(II). This event may occur in the picosecond time domain if it is to compete with the radiative emission ( $h\nu_e$ ). The CTTS process causes the solvent shell of ANS(II) to reorient and follow the fluorescence emission ( $h\nu'_e$ ) from the state  $S_1^{CT} \rightarrow S_0$ . Some other photophysical processes, which are not depicted in the above scheme, may occur during the lifetime of the excited ANS. Those processes are not included in this analytical method because we want to keep as simple a picture as possible and we assume that the rate of CTTS is much greater than other nonradiative rates.

In order to take account of the fact that no more than one ANS molecule is involved in the fluorescence process, this photophysical kinetics model uses the probability matrix method [134] similar to the Markov's "gambler's ruin" problem [135]. The Markovian situation implies that the transition probability depends only on the present state of a molecule at time  $t$  but not on the previous history of the molecule.

Using the probability matrix method, the quantitative model can be constructed for calculating the combined diffusion and radiative decay dynamics of the ANS molecule in RM's. It can also be applied to formulate a better structural picture of the CTTS process in the RM's. In this analytical method the square probability matrix  $\bar{P}$  whose dimension is  $2N + 1$ , where  $N$  is the number of zones including the SZ used for the RM in question, has the following form,

$$\bar{P} = \begin{pmatrix} A_{11} & K_{12} & 0 & \cdots & K_{1B} & 0 & 0 & \cdots & K_{1G} \\ K_{21} & A_{22} & K_{23} & \cdots & 0 & K_{2B} & 0 & \cdots & K_{2G} \\ 0 & K_{32} & A_{33} & \cdots & 0 & 0 & K_{3B} & \cdots & K_{3G} \\ \vdots & \vdots & \vdots & \ddots & \vdots & \vdots & \vdots & \ddots & \vdots \\ 0 & 0 & 0 & \cdots & B_{11} & J_{12} & 0 & \cdots & J_{1G} \\ 0 & 0 & 0 & \cdots & J_{21} & B_{22} & J_{23} & \cdots & J_{2G} \\ 0 & 0 & 0 & \cdots & 0 & J_{32} & B_{33} & \cdots & J_{3G} \\ \vdots & \vdots & \vdots & \ddots & \vdots & \vdots & \vdots & \ddots & \vdots \\ 0 & 0 & 0 & \cdots & 0 & 0 & 0 & \cdots & 1 \end{pmatrix}. \quad (4-5)$$

Each element of this matrix denotes the transition probability during a small time span  $\Delta t$  for some event to occur. The rows 1 (SZ) to  $N$  (central zone) of the matrix correspond to events occurring in each zone for the excited state of an ANS(I) molecule. The next  $N$  rows from  $N + 1$  to  $2N$  represent events for the excited state of an ANS(II) in the various zones since the excited ANS(I) is supposed to dissociate to an electron [51,59,60]. The row  $2N + 1$  corresponds to the common ground state to which all excited state tend.

The off-diagonal elements of the matrix,  $K_{i,i\pm 1}$  and  $J_{i,i\pm 1}$ , correspond to the diffusion between adjacent zones, respectively. The other off-diagonal elements  $K_{iB}$  describe the production of the ANS(II) by CTTS from the ANS(I) molecule in the same zone. The elements  $K_{iG}$  and  $J_{iG}$  correspond to transitions directly to the ground state from the ANS(I) and the ANS(II) respectively by a radiative or a nonradiative process.

Since the diagonal elements  $A_{ii}$  and  $B_{ii}$  denote the probabilities for remaining unchanged during an incremental time step  $\Delta t$ , they are given by

$$A_{ii} = 1 - K_{i,i+1} - K_{i,i-1} - K_{iB} - K_{iG} \quad (4-6)$$

and

$$B_{ii} = 1 - J_{i,i+1} - J_{i,i-1} - J_{iG}, \quad (4-7)$$

respectively. In order to avoid computational overruns and errors in the calculation, the time step  $\Delta t$  must be chosen sufficiently small that the diagonal probabilities are all close to unity. Since the matrix represents the probabilities for all possible events in a zone to occur during each  $\Delta t$ , the elements in a row must sum to unity.

As zero time signifies the point of laser excitation, transitions from the ground state back to excited states cannot take place following this time, and therefore the corresponding off-diagonal elements are all zero. In the probability matrix, it has also been assumed that the energetically uphill back reaction, ANS(II)  $\rightarrow$  ANS(I), does not occur.

The zone-dependent off-diagonal elements are governed by the connectivity relationships between the diffusion and the FD process, since probe molecules are free to diffuse towards the center of the reverse micelle. In order to describe the variation in translational diffusion and in the FD decay rate as a function of distance  $r$  from the interface, the hyperbolic tangent function, because of its versatility, is employed for the rates  $R$  of diffusion and CTTS, respectively.

$$\frac{R_{Z(r)}}{R_b} = \tanh(a + br^n), \quad (4-8)$$

where  $R_{Z(r)}$  is the rate for an RM zone  $Z$ , whose midpoint lies a distance  $r$  from the hydrophilic interface, and  $R_b$  is the rate for bulk state water. The ratio  $R_{Z(r)} / R_b$  depends on the process considered, diffusion (primed) or FD (double primed). The resulting

parameters  $a'$ ,  $b'$ ,  $n'$ ,  $a''$ ,  $b''$ , and  $n''$  are adjustable constants. The parameters  $n'$  and  $n''$  are integral powers that establish how quickly bulk-water properties set in as  $r$  increases.

The diffusional elements were computed from the following equation representing the flux of particles  $F$  normal to the interface [136],

$$F = -\frac{R_{z(r)}}{R_b} \times \frac{\Delta n}{\Delta z} \times \mathcal{D}, \quad (4-9)$$

where  $\Delta n / \Delta z$  is the concentration gradient of ANS molecules and  $\mathcal{D}$  is the diffusion coefficient of ANS in bulk water. The diffusion coefficient of ANS in pure water is given in Table 1.1. Since each RM contains only one probe molecule, these quantities are considered to be averages over a large ensemble of RM of the specific size under consideration. The number of particles per second crossing a zone boundary is given as the flux  $F$  multiplied by the surface area of this boundary. To obtain the concentration gradient  $\Delta n / \Delta z$ , we use the number of particles per volume of zone and the discrete zone thickness  $\Delta z$ . If we divide  $\Delta z$  to be very small, it will be given by smooth concentration gradient in the RM. During the relaxation dynamics, this concentration varies among the zones owing to the more rapid depletion of probe molecules farther from the interface because of the shorter lifetimes there.

The probability  $K_{i,i\pm 1}$  for boundary crossing to occur in a given time step  $\Delta t$  is obtained by multiplying the particles per second by  $\Delta t$ . It is assumed that ANS(I) and ANS(II) molecules have identical diffusion properties so that  $K_{i,i\pm 1} = J_{i,i\pm 1}$ . Even though this assumption may not be exactly right because of the charge on the ANS(II), the

dynamics of the ANS(II) will have no effect on the ANS(I), which comprises the central issue of the present study.

Assuming that perturbations on the water structure have little effect on the photophysics,  $K_{iG}$  can be obtained from the ANS lifetime of 8600 ps in non-water solvents [51]. The lifetime of ANS in bulk water is taken to be 280 ps from the results presented in Chapter III. The lifetime of the ANS(II) (which corresponds to matrix elements  $J_{iG}$ ) can roughly be assumed to be a few nanoseconds since they do not affect the analysis of the ANS(I).

#### 4.3 Fitting Procedures

The probability matrix  $\bar{P}$  is applied to the concentration changes of the ANS(I) and the ANS(II) in the various zones. Thus, to construct theoretical fluorescence decay curves by summing over all the zones, a series of matrix multiplications is performed, one for each evolving  $\Delta t$ . One first multiplies the probability matrix  $\bar{P}$  by a density vector  $\hat{C}^0$ , which denotes the initial concentrations of the ANS(I), ANS(II) and ground state in the various zones. The initial concentrations of the ANS(I) molecules are expressed in terms of volume fractions and typically, those of the ANS(II) and ground state are set to zero. Again, these quantities are thought of as being averaged over an ensemble of RM. If there is a surface interaction in the SZ, the initial concentration of ANS(I) molecules in the SZ is not proportional to its volume, as is the case for all the other zones. In that case, the initial concentration profiles can be determined by a pre-equilibration procedure using

$10^4 \times \Delta t$ , where all off-diagonal elements are turned off except those denoting diffusion of the ANS(I) molecules  $K_{i,i\pm 1}$ .

In the actual photophysical computation, each time the row matrix  $\hat{C}^n$  is multiplied by  $\bar{P}$ , it changes to an updated row matrix  $\hat{C}^{n+1}$ . These evolving  $\hat{C}^n$ 's then give the variations in the concentrations, during the series of time steps  $n\Delta t$ , of the ANS(I) and the ANS(II) in the various zones, as well as the common ground state as it continuously building up. In other words, the  $n$  successive multiplications are given by

$$\begin{aligned}\hat{C}^0 \times \bar{P} &= \hat{C}^1 \\ \hat{C}^1 \times \bar{P} &= \hat{C}^2 \\ &\vdots \\ \hat{C}^{n-1} \times \bar{P} &= \hat{C}^n.\end{aligned}\tag{4-10}$$

The evolving  $\hat{C}^n$ 's give the concentrations and thus the emission intensities of the probe as a function of time. Throughout the entire computation, if everything is done correctly, except for round-off errors the sum of all the concentrations (including that of the ground state) remains a constant. The constant is unity if the concentrations are initially normalized.

Usually,  $\Delta t$  is chosen to be sufficiently small,  $\sim 1$  ps, that the diagonal elements are within  $< 1\%$  of unity. Thus, following the  $10^4$  time step equilibration process if necessary, we use 11,000 additional time steps to compute theoretical decay curves out to 11 ns. The Fortran program for carrying out these set of multiplications is straightforward and is computationally efficient. In principle, then, the time dependent concentrations

represented by the evolving concentration matrix summed over all zones should give the experimental decay of the ANS(I) and the rise and decay of the ANS(II) species.

There is another more sophisticated method [52] for obtaining the various concentrations at different times. In this method, one first diagonalizes the probability matrix  $\bar{P}$  with the help of the transformation matrix  $T$  and its inverse matrix  $T^{-1}$  such that,

$$T^{-1}\bar{P}T = D, \quad (4-11)$$

where  $D$  is the resulting diagonal matrix,  $D = \|\lambda_i\|$ . Upon raising the diagonal matrix  $D$  to the  $m$ th power, the equation (4-11) is given by

$$T^{-1}\bar{P}^m T = D^m, \quad (4-12)$$

and thus

$$\bar{P}^m = T^{-1}D^m T. \quad (4-13)$$

Here  $D^m = \|\lambda_i^m\|$  and for sufficiently small  $\Delta t$ ,  $\lambda_i^m \approx e^{-\lambda_i m \Delta t}$ . Finally, the concentrations and thus the emission intensities after a time  $m \Delta t$  are given by

$$\hat{C}^m = T D^m T^{-1} \times \hat{C}^0. \quad (4-14)$$

Since raising a diagonal matrix to a given power is done simply by raising all of its diagonal elements to the same power, the process seems very much more compact. But, of course, at the beginning one has to diagonalize the matrix  $\bar{P}$ . In practice, we have found that, computationally, the diagonalization of the large matrices employed in this method is much more time consuming than the multiplication method explained above. In

this work, we will therefore present results obtained using the first approach of repeatedly multiplying the probability matrix  $\bar{P}$  by the concentration.

The decay data of both the ANS(I) and the ANS(II) species are given by the time dependent concentrations summed over all the zones. The parameters  $a'$ ,  $b'$ ,  $n'$ ,  $a''$ ,  $b''$ , and  $n''$  used in connectivity relationships for both the diffusion and charge transfer are then extracted from the experimental decay curves by using a non-linear least squares (NLLS) fitting method [113]. These parameters should reflect the photophysical and diffusional properties of the probe in the confined water environment as a function of distance from the hydrophilic interface.

#### 4.4 Results

We have analyzed the four experimental decay curves using the multiplication procedure in conjunction with a NLLS fitting method. In this analysis, the width of the special zone (SZ) was chosen to be the same as the widths of the other zones. The  $n'$  and  $n''$  parameters were set equal to the nearest integer according to a series of fits where these parameters were allowed to vary. The values of  $n'$  and  $n''$  are then 1 and 6, respectively. The  $a$ - and  $b$ -parameters were allowed to vary in the analysis, where the  $b$ -parameters depend on distance in units Å.

The results of the fitting procedure are presented in Table 4.2, where values found for the  $a'$ ,  $b'$ ,  $a''$ , and  $b''$  constants of Eq. (4-8) are given with the  $\chi_r^2$  values. The corresponding fitting results to experimental decay curves for the ANS(I) are given in Figures 4.2-4.5. The solid line represents the theoretical fit to the noise curve for the

Table 4.2. Diffusion and Lifetime Parameters Employed for the Analysis.<sup>a</sup>

$r_w$ (Å)	$a'$	$b'$	$a''$	$b''$	$\chi_r^2$
10.0	0.0	$1.30 \times 10^{-4}$	$1.42 \times 10^{-2}$	$9.61 \times 10^{-5}$	1.27
16.5	0.0	$5.91 \times 10^{-3}$	$1.42 \times 10^{-2}$	$3.92 \times 10^{-5}$	1.29
29.5	0.0	$2.04 \times 10^{-2}$	$1.42 \times 10^{-2}$	$1.58 \times 10^{-6}$	1.07
55.2	0.0	$3.76 \times 10^{-2}$	$1.42 \times 10^{-2}$	$1.02 \times 10^{-7}$	1.19

<sup>a</sup>The parameters,  $n'$  and  $n''$  in Eq. (4-8), are fixed at 1 and 6, respectively.

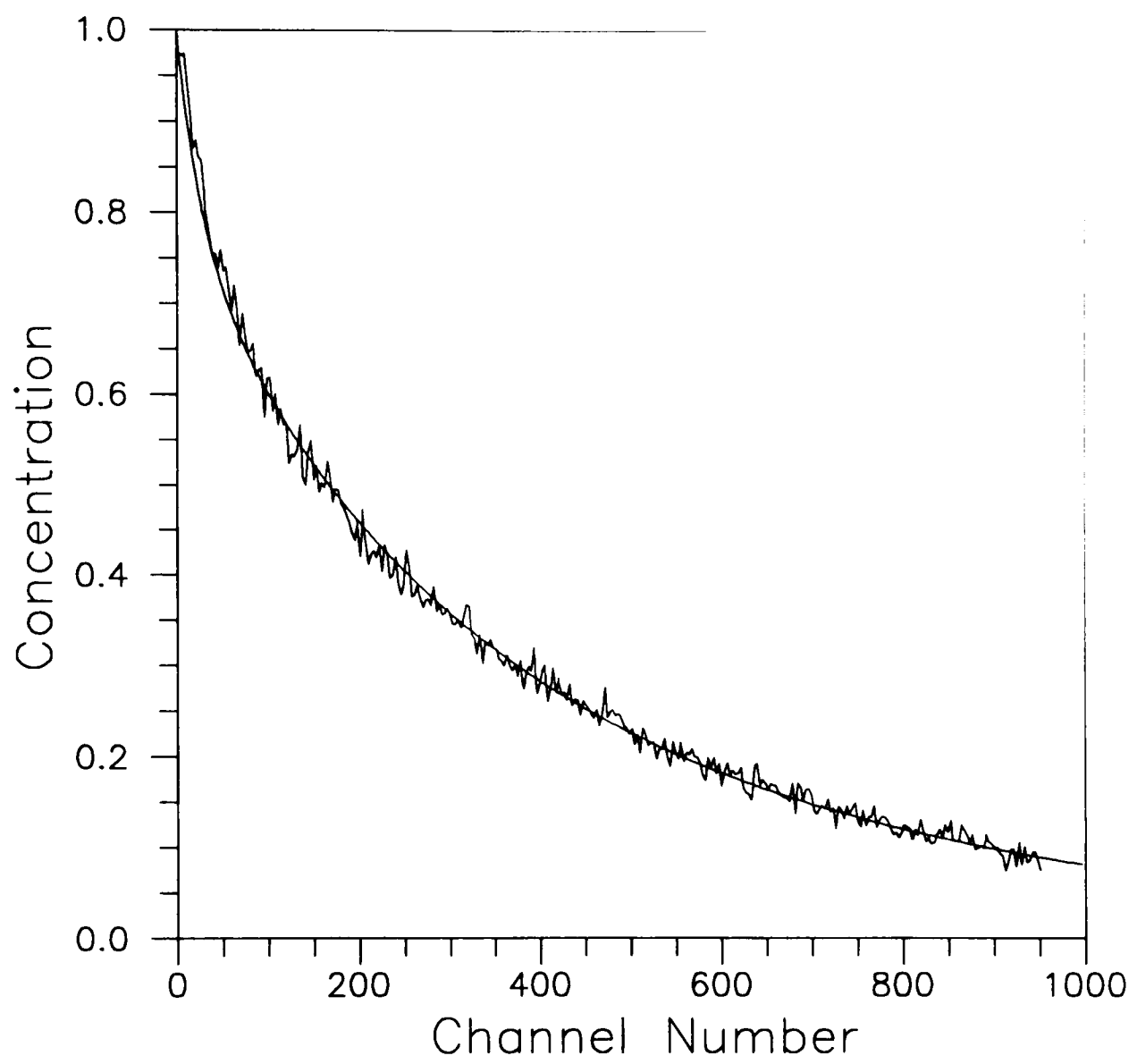


Figure 4.2. The theoretical fit to the experimental decay profile for  $r_v = 10.0 \text{ \AA RM}$ .

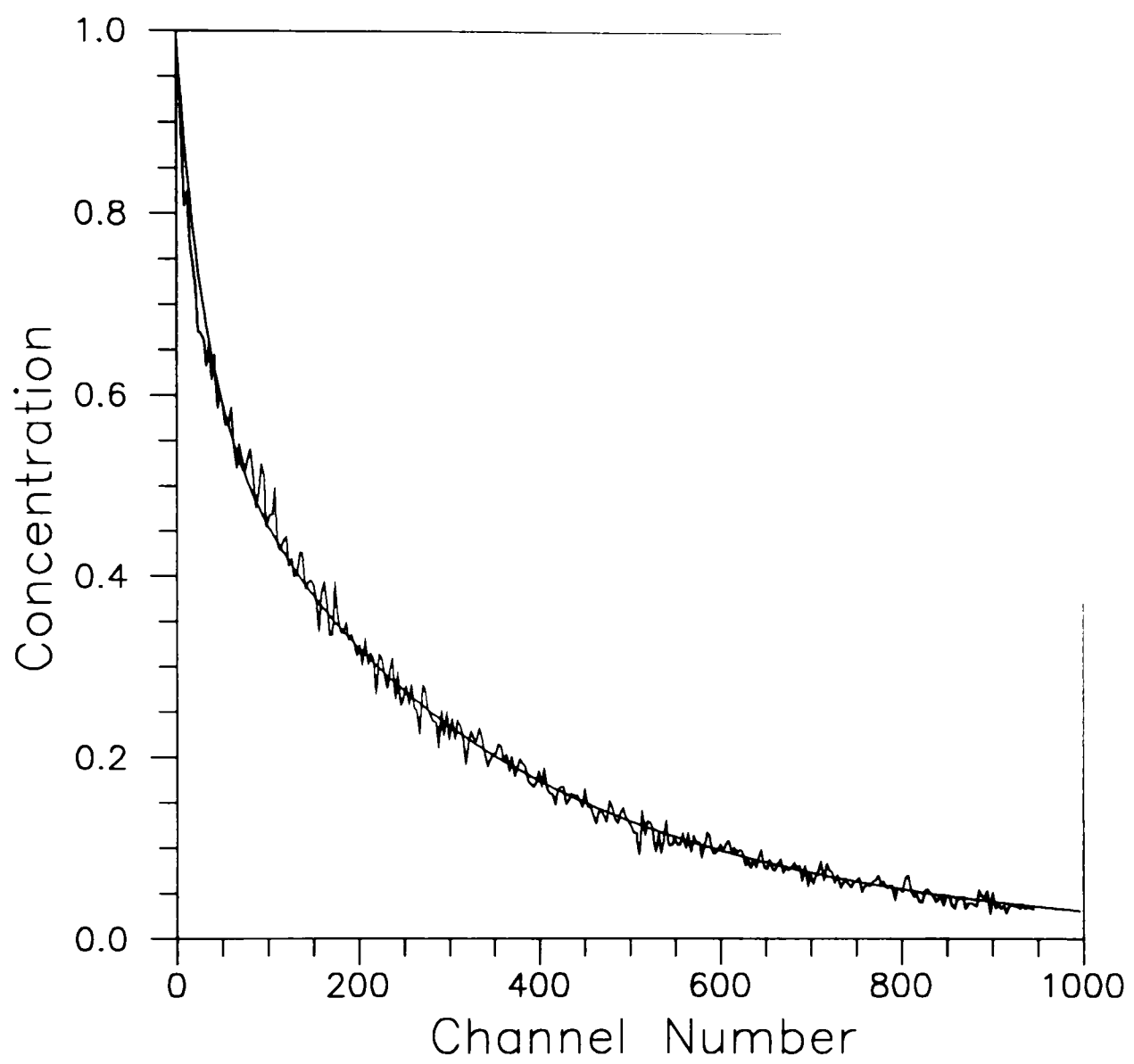


Figure 4.3. The theoretical fit to the experimental decay profile for  $r_w=16.5 \text{ \AA}$  RM.

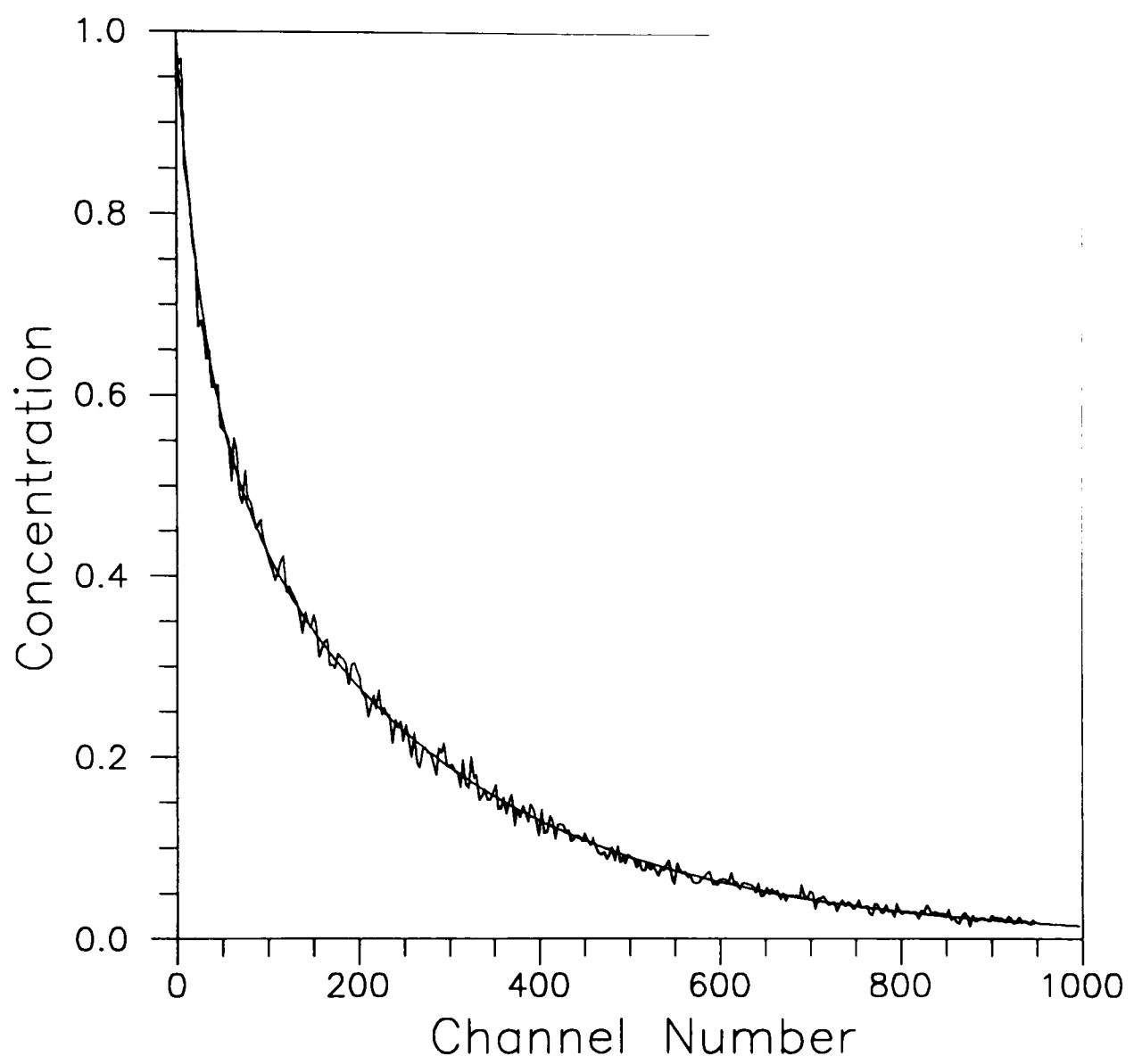


Figure 4.4. The theoretical fit to the experimental decay profile for  $r_w = 29.5 \text{ \AA}$  RM.

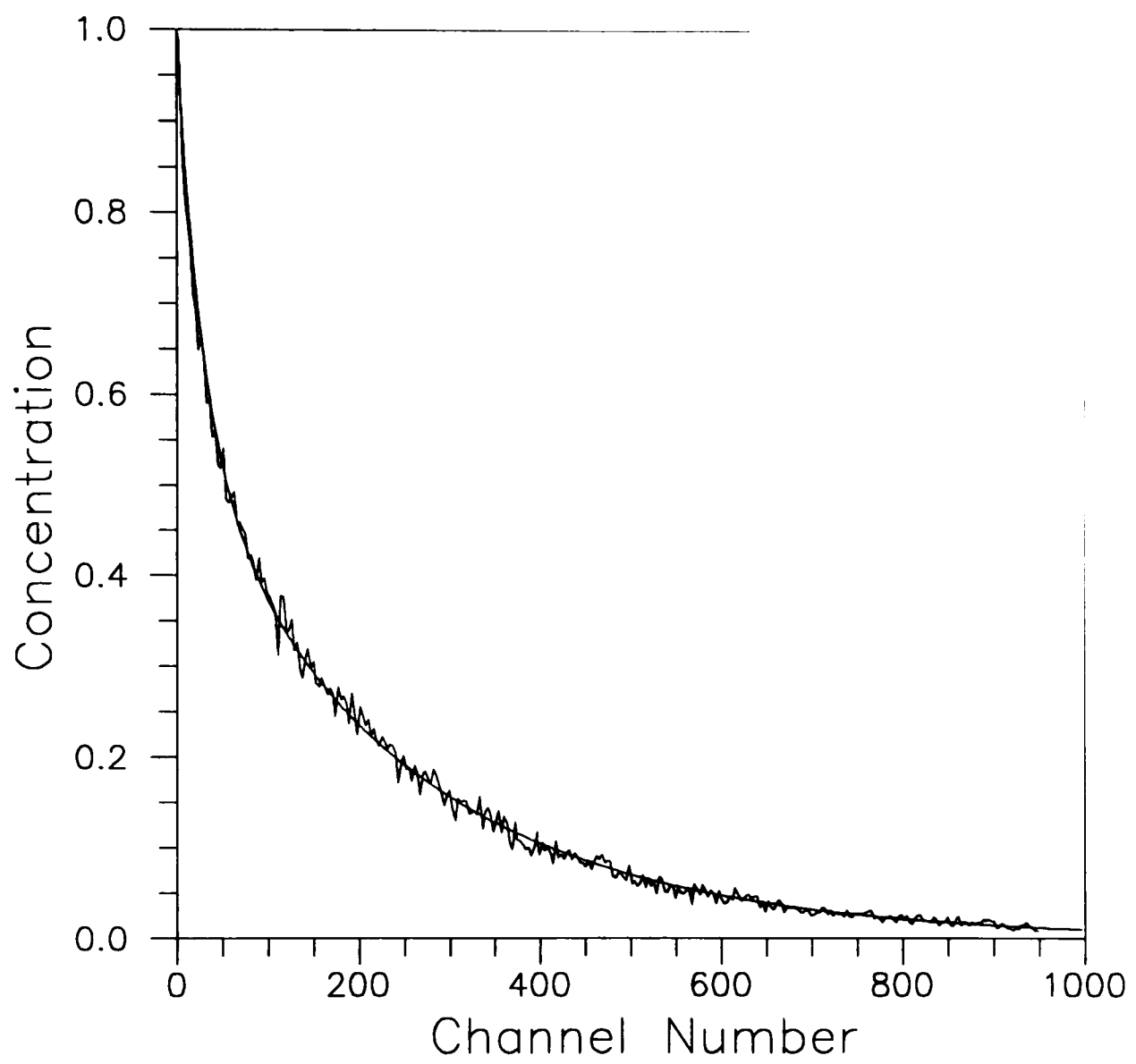


Figure 4.5. The theoretical fit to the experimental decay profile for  $r_w = 55.2 \text{ \AA RM}$ .

experimental decay. The quality of the fits for the decaying ANS(I) molecule can be evaluated visually from an examination of Figures 4.2-4.5 together with the  $\chi_r^2$  values in Table 4.2. Note that, with the somewhat limited experimental time resolution used in the present work, "noise" in the fitting stages of the decays could play a role in the fitting.

The resulting connectivity relationships required to fit the decay data for all four RM's in Table 4.2 are plotted in Figure 4.6 for diffusion and Figure 4.7 for lifetime. The distance,  $r$ , from the RM surface (i.e., the distance of the probe from the hydrophilic interface) is given in Å along the horizontal axis. The diffusion and lifetime relationships from Eq. (4-8) are plotted with respect to the estimated bulk-state diffusion constant, 0.065 Å/ps, and the bulk-state lifetime, 280 ps. The symbols in Figure 4.6 are used to clarify for the various RM's.

Even though the experimental decay data for the ANS(II) have been found to slightly exhibit an expected rise and fall behavior at the higher reverse micelle sizes (cf. Figures 3.3-3.6), these data are not suitable for this analysis. The main reason is that spectral overlap causes the contamination of ANS(II) decays by fluorescence of the ANS(I), and so much wavelength filtering so far has resulted in very noisy ANS(II) decay curves. However, we have been able to establish that the ANS(II) rise and fall curves can be approximated by subtracting a certain fraction (over 50 %) of the calculated contaminating ANS(I) decays. Future experiments with an improved TCSPC system should be able to do a more convincing job.

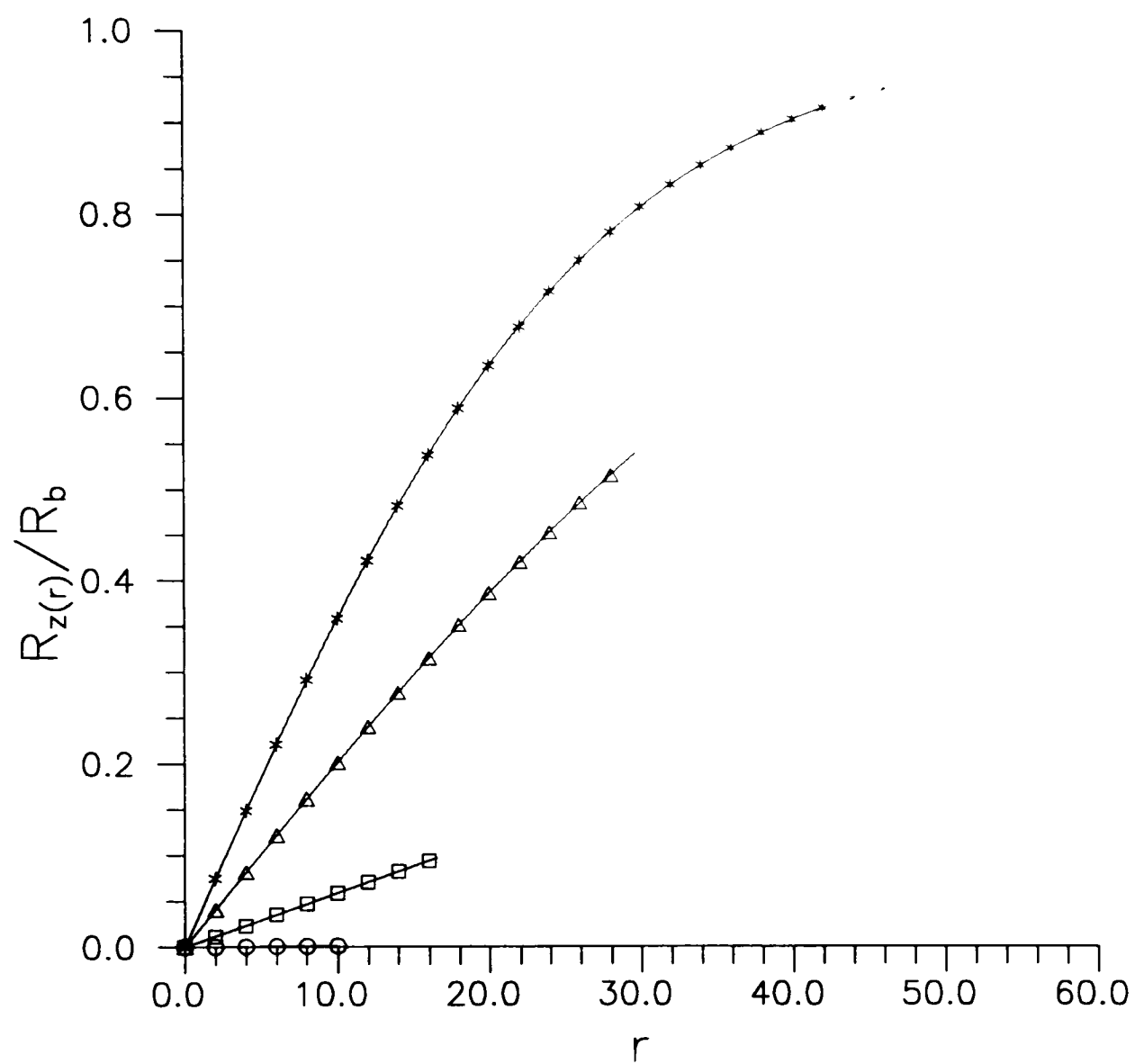


Figure 4.6. Diffusion relationships of ANS(I) for the various reverse micelle sizes.  
 \* = 55.2 Å radius RM, Δ = 29.5 Å radius RM, □ = 16.5 Å radius RM,  
 and ○ = 10.0 Å radius RM.

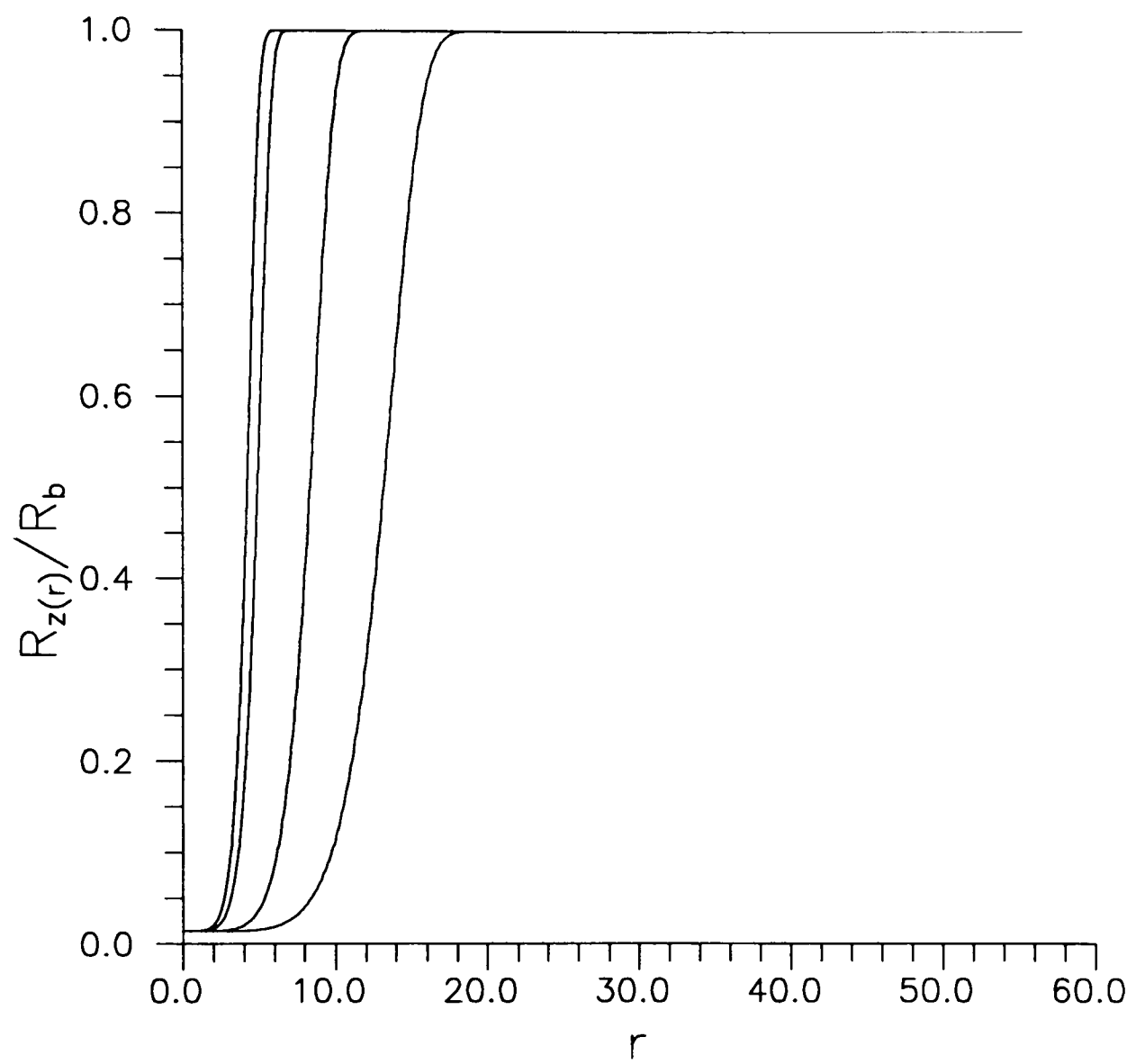


Figure 4.7. Lifetime relationships of ANS(I) for the various reverse micelle sizes. Left to right 10.0, 16.5, 29.5, and 55.2 Å radius RM.

#### 4.5 Discussion

Diffusion in the RM may correspond either to rotational or translational motions of the photochemically active site (the anilino- group) in the ANS probe molecule. Clearly, diffusion of the probe in and out of the surface zone adjacent to the micelle surface is required during the relaxation dynamics, see Figure 4.1. Otherwise, if the probes had a propensity to be strongly bound to the hydrophilic micelle surface, all probes would collect in the surface zone. This situation would lead to a long lived single exponential decay, as observed for probe molecules absorbed from aqueous solutions onto silica gel [56]. On the other hand, the probes would never be found in the surface zone if diffusion out were much faster than diffusion in, i.e., if the probe were repelled by the surface, as proposed by Wong et al. [42]. Neither of these situations seems to be the case. As seen from Figure 4.6, the very strong binding of "surface eater molecules" to the interfacial AOT head groups, as implied by the NMR experiments [35], does not carry over to the probe molecules.

In fact, it was found that fitting all four RM's with the same connectivity relationships was non-trivial and probably not possible. Parameters for the smallest two RM's considered here ( $r_w = 10.0 \text{ \AA}$  and  $16.5 \text{ \AA}$ ) seem definitely to be different from the parameters required to fit the larger RM's. In particular, the  $10.0 \text{ \AA}$  RM seems to require a smaller, almost zero, diffusional flux compared with the larger RM's as seen from Figure 4.6. This could mean that the water in such small confinement, surrounded by the highly hydrophilic head group surface of high curvature, is nearly ice-like (cf. Figure 3 of Ref.

[37]). The huge perturbation on diffusion found here indicates the difficulties and dangers of trying to apply bulk water properties to phenomena occurring in confined volumes.

Comparing Figure 4.7 with Figure 4.6, why is the CTTS FD process not affected very far from the interface, while translational diffusion is? On reflection, it does not seem reasonable that orientational motions of water, which determine the FD process, would be less affected far from the RM surface than are translational motions of the large probe molecules confined in such tiny water pools. Rotational diffusion is probably closer to normal in these systems, but this mode of diffusion only oscillates the active site of the probe molecule between adjacent zones. Perhaps the confining nature of the nearly rigid RM walls gives a lowered probability of vacancy fluctuations, particularly near the interface. This prevents efficient translations of the probes because of a "forced packing" arrangement of the water molecules in the confined space. This packing seems important in the 10.0 Å radius water pool.

Finally, while it is reasonable that translational diffusion might become more highly perturbed as the confined volume of such small water pools decreases, it is a mystery why the photophysics seems faster for certain regions of the smallest RMs compared with the same regions in the large RMs. We have found that the fitting procedure is very sensitive to the choice of the lifetime parameters in Equation (4-8). It could be that those parameters do not change or change even in an opposite fashion than pictured in Figure 4.7. The acquisition of better data with a faster microchannel-plate photomultiplier tube could help resolve this issue. Another possibility is that, in agreement with Wong et al. [42], there is some type of repulsion of the probe by the micelle surface which affects our

analysis method. Actually, examination of Figure 4.7 shows that the photophysics in all the micelles becomes bulk-like within  $\sim 6-18$  Å from the surface, so the apparent variations in the FD rates may just be caused by slight experimental uncertainties entering the fitting procedure.

## CHAPTER V

### CONCLUSIONS

A greater understanding of the chemical and physical properties of interfacial water has been acquired by the use of the RM water pools. The TCSPC technique has then been employed for the measurement of lifetimes of the probe molecule ANS in RM's of various sizes. The fluorescence decays of the ANS(I) and the ANS(II) in four RM's have been found and can be described as a continuous distribution of lifetimes at different distances from the RM surface. The results imply that different environmental domains of ANS can strongly influence the lifetimes because of solvent effects. Under such circumstances, water properties are changed gradually from the interface to the center of the RM.

From the results of fluorescence decay profiles of ANS(I) in a RM, one can infer the following important findings. Fast decay components are found near the central region of the RM's, where the solvent properties approach those of bulk water. Long-lived decay components occur close to the surface, where the behavior of water solvent is mediated by the surface. With the weight of the short-lived fluorescence components increasing with the RM's size, it is certain that the ANS molecules do not become permanently attached to the inner surface of the RM. The results suggest there is free diffusion from the interface inward on the time scale of the experiment.

In order to gain further insight into the lifetime distribution as well as other properties of ANS(I) in the RM's, experimental decay data of ANS(I) in these RM's were analyzed by using an analytical method with a NLLS fitting technique. The variations of

lifetime and diffusion relative to bulk water values were found as a function of a distance  $r$  from the RM surface as shown in Figures 4.6 and 4.7. The results show a correlation with each other, in that there is more fluorescence at the interface and slower diffusion of the ANS(I) normal to the interface, compared to bulk water. Strong structural perturbations at the surface can induce a partially ordered form of water by interactions with the surface. The perturbed structure extends to nearly 10-15 Å from the surface as seen from our result shown in Figure 4.7. It is evident that the properties of water near a surface are markedly different from those of bulk water. We believe that this is also true for the behavior of biological interfacial water [4].

Since the weights of the fast components are strongly affected by the size of the RM, water solvent slowly hydrates the electronic charge because of the slow orientational motions of water at the interface. The charge transfer rate would be expected to increase towards the center of a large RM where a bulk-like water environment dominates. This is supported by the fact that studies of this type [11] have already indicated that when water is confined to volumes having dimensions less than about 500 Å one can observe large changes, compared with bulk water, in the behavior of the charge transfer to solvent [47].

Through this work, it is possible to have a better understanding of the properties of interfacial water in biological environments. The most important conclusion is drawn from the fact that bulk water properties could not be applied to water-rich biological systems in confined volumes since we observed a large perturbation of translational diffusion near the surface, as seen from Figure 4.6. All the methods and techniques presented here can be applied to various interfaces and surfaces, for example, between quartz plates or the

metals, pores, and thin films. It is necessarily required to accumulate more chemical and physical properties at those interfaces in order to gain more knowledge for water-rich biomolecular systems.

A new series of laboratory experiments is currently being directed towards these subjects. The hope is that these experimental results and those from other techniques [33,137,138] with intrinsic molecular-level resolution, when combined with improved MD models, can provide added spatial and dynamic resolving power to the study of water near interfaces.

Future experimental work on the RM system using the above techniques will be directed toward the use of a faster probe molecule, 1-naphtol, rather than ANS. Since 1-naphtol is highly soluble in primary hydrocarbon solvents, it is necessary to seek other primary solvents and hydrophobic tail groups, such as fluorocarbons, in which 1-naphtol is insoluble. The water/1-naphtol/AOT/heptane probe experiments will provide complementary information about the RM system since they are better able to achieve a more informative molecular resolution in both space and time.

PART II  
NOVEL POTENTIAL FUNCTIONS OF WATER  
FOR COMPUTER SIMULATIONS

## CHAPTER VI

### ONE-DIMENSIONAL FLUID MODEL

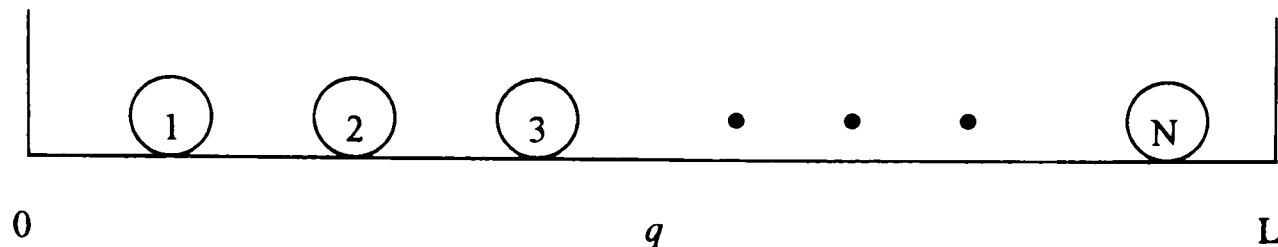
There have been many attempts to explain the density maximum of liquid water at 4 °C. These have usually focused on complicated mechanisms involving lengthy computations or many-body interaction concepts. In this study, the possibility that the density maximum may have a simple origin is explored using an exactly soluble model.

The main point of this one-dimensional model will be to study the competing effects on the density of two second-neighbor potential wells. We can simply treat the second neighbors in a real liquid as "first neighbors" in the theoretical model. The distortion from a real three-dimensional structure thus comes from the placement of two second-neighbor wells in a line rather than at some angle. The second-neighbor positions can then be modeled by two square wells between each particle along this line.

To investigate this prospect, the one-dimensional fluid Takahashi model [139] with nearest neighbor interactions will be introduced and studied. We will apply and test this model for several simple potentials showing no density maximum. However, for certain double well potentials, it can be shown that a density maximum exists for a range of low pressures. This potential consists of a hard core and two square wells beyond which the potential is zero. It is believed that this may help explain the density maximum in water and help formulate a model for water that gives the correct temperature- and pressure-dependent density from the presence of the two second-neighbor potential wells .

### 6.1 Takahashi Model

An one-dimensional Takahashi fluid at a given temperature  $T$  and pressure  $P$  would schematically appear as the string system:



Here  $N$  is the number of particles,  $q$  is the position of a particle, and  $L$  is the “volume,” actually the length of the string corresponding to the given  $T$  and  $P$ . In the one-dimensional string system  $P$  is the force of tension at the two ends of the fluid system. Note that the relative order of the particles is fixed. This is because the particles get stopped by their hard cores and cannot go around one another; they are strung like beads on a string. It is a well-known statement that a set of real numbers (or points along a line) forms an ordered field. Therefore,  $0 < q_1 < q_2 < q_3 \cdots < q_N < L$ . This single fact, which distinguishes the Takahashi model from models in higher dimensions, leads to its exact solution. In higher dimensions the particles can go around on another and, for example, particle 1 can be found between particle 2 and 3 at some time. The set of movable points in a plane or a three-dimensional space cannot be ordered in any way. Even if the system is artificially prepared to be in a state with the particle positions ordered in some way, interactions between the particles will put them in motion and the ordering will be lost in some time.

This problem for one dimension was first solved for a hard sphere potential by Tonks [140], and was later extended to more general potentials by Takahashi [139] and others [141]. The classical Hamiltonian in this model is

$$H = \sum_{i=1}^N \frac{p_i^2}{2m} + U(q_i), \quad (6-1)$$

where  $p_i$  is the momentum of particle  $i$  with mass  $m$  and  $U(q_i)$  is the total potential energy of the system.  $U(q_i)$  is assumed to be a sum of pair potentials involving nearest neighbor interactions and including a hard core for stability. The potential function is given by

$$U(q_i) = \sum_{i=1}^{N-1} u(|q_{i+1} - q_i|), \quad (6-2)$$

which has a total of  $N - 1$  terms and allows only nearest neighbor pair interactions.

Since the system is studied over a range of temperatures and pressures, it is convenient to work with the isobaric-isothermal ensemble for which the partition function [142,143] for a classical one-dimensional fluid is

$$Q_N(P, T) = \frac{1}{N! h^N} \int_0^\infty dL \int e^{-\beta(PL+H)} d^N q d^N p, \quad (6-3)$$

where  $h$  is the Planck constant and  $\beta = 1/k_B T$ . The single integral sign collectively stands for  $N$  momentum integrals with limits  $-\infty$  to  $+\infty$ , and  $N$  position integrals with limits 0 to  $L$ . Of course, as required for an isobaric-isothermal ensemble, both the energy and the volume of the system are allowed to take all possible values so that  $T$  and  $P$  are fixed at the required values.

The thermodynamics is obtained from the Gibbs free energy [142]

$$G(P, T) = -k_B T \ln Q_N(P, T). \quad (6-4)$$

Using standard manipulations involving the laws of thermodynamics [144],

$$\left(\frac{\partial G}{\partial P}\right)_T = L \quad \text{and} \quad \left(\frac{\partial G}{\partial T}\right)_P = -S. \quad (6-5)$$

As is usual in classical systems, the momentum and the position integrals separate.

Therefore, the momentum integrals in Eq. (6-3) may be evaluated to yield,

$$Q_N(P, T) = \frac{1}{N!} \left(\frac{2\pi m k_B T}{h^2}\right)^{N/2} \int_0^\infty dL e^{-\beta PL} \\ \times \int_0^L dq_N \cdots \int_0^L dq_i \cdots \int_0^L dq_1 \exp\left[-\beta \sum_{i=1}^{N-1} u(|q_{i+1} - q_i|)\right]. \quad (6-6)$$

The multi-dimensional configurational integral over the positions of all the particles can be determined exactly in one dimension by showing that it is  $N!$  times the integral over the special region,  $0 < q_1 < q_2 < q_3 \cdots < q_N < L$  [139-141]. Therefore, the isobaric-isothermal partition function reduces to,

$$Q_N(P, T) = \left(\frac{2\pi m k_B T}{h^2}\right)^{N/2} \int_0^\infty dL e^{-\beta PL} \\ \times \int_0^L dq_N \int_0^{q_N} dq_{N-1} e^{-\beta u(q_N - q_{N-1})} \cdots \int_0^{q_2} dq_1 e^{-\beta u(q_2 - q_1)}. \quad (6-7)$$

This integral is the Laplace transform of a number of convolutions. So, using the convolution theorem [145], one obtains

$$Q_N(P, T) = \left(\frac{2\pi m k_B T}{h^2}\right)^{N/2} \frac{1}{\beta P} [\kappa(P, T)]^{N-1} \frac{1}{\beta P}, \quad (6-8)$$

where  $\kappa(P, T)$  is the Laplace transform of  $e^{-\beta u}$ ,

$$\kappa(P, T) = \int_0^\infty dx e^{-\beta px} e^{-\beta u(x)}. \quad (6-9)$$

In this calculation, the fixed end boundary condition has been used. Therefore, the two factors of  $1/\beta P$  in Eq. (6-8) arise from the fact that the two end particles (numbered 1 and  $N$ ) interact only with one nearest neighbor whereas all the inner particles interact with two neighbors, one on either side. On the other hand, if the periodic boundary condition had been chosen, these two end particles would have become nearest neighbors and would have interacted with each other. In that case the two factors representing the missing partners mentioned above would have been replaced by a single  $\kappa(P, T)$  to reflect the added interaction between the particles numbered 1 and  $N$ .

From the equations (6-4) and (6-8), the Gibbs free energy is then

$$G(P, T) = -\frac{1}{\beta} \left[ \frac{N}{2} \ln \left( \frac{2\pi m k_B T}{h^2} \right) + (N-1) \ln \kappa(P, T) - 2 \ln \beta P \right]. \quad (6-10)$$

Taking the thermodynamic limit in which  $L \rightarrow \infty$ ,  $N \rightarrow \infty$ , while the volume per particle  $l = L/N$  is held constant, one obtains for the Gibbs free energy,

$$G(P, T) = -\frac{N}{\beta} \left[ \frac{1}{2} \ln \left( \frac{2\pi m k_B T}{h^2} \right) + \ln \kappa(P, T) \right]. \quad (6-11)$$

From Eq. (6-5), the total volume of the system in this limit is given by

$$L = \left( \frac{\partial G}{\partial P} \right)_T = -\frac{N}{\beta \kappa(P, T)} \left( \frac{\partial \kappa(P, T)}{\partial P} \right)_T, \quad (6-12)$$

and the volume per particle  $l$  and the density  $\rho$  are given by

$$l = \frac{1}{\rho} = -\frac{1}{\beta \kappa(P, T)} \left( \frac{\partial \kappa(P, T)}{\partial P} \right)_T. \quad (6-13)$$

Therefore, to obtain the density, one must first choose a potential, then perform the  $\kappa(P, T)$  integral in Eq. (6-9), and differentiate the result with respect to the pressure  $P$  and then the above relation gives the desired result.

## 6.2 Simple Potential Functions

First, let us consider a very simple potential function to study the behavior of density with respect to the temperature  $T$ . For the ideal gas, there is no pair potential,  $u = 0$ , and the  $\kappa(P, T)$  integral and its derivative are easily done to get

$$\kappa(P, T) = \frac{1}{\beta P} \quad \text{and} \quad \frac{\partial \kappa(P, T)}{\partial P} = -\frac{1}{\beta P^2}. \quad (6-14)$$

Then, the volume per particle is given by

$$l = \frac{1}{\beta P} = \frac{k_B T}{P}, \quad (6-15)$$

and then

$$PL = Nk_B T, \quad (6-16)$$

which is the ideal gas equation in one dimension and we have introduced the one-dimensional gas constant  $R = Nk_B$ .

The density of the ideal gas for a given pressure is a monotonously decreasing function of temperature. There is no such thing as an ideal gas in real life, but all gases do behave like one for sufficiently high temperatures and sufficiently low densities, a regime in which the kinetic energy dominates over the potential energy, which can then be neglected. What happens to the ideal gas at low temperatures? The density keeps on

increasing and becomes infinite at absolute zero, indicating a collapse of the system to the origin. This is highly unphysical. Real gases do not have this problem because real particles have a repulsive potential at small separations. Therefore real gases condense to a close packed crystalline configuration at absolute zero, except for Helium in which the large quantum mechanical zero point energy keeps it a liquid at ordinary pressures.

To avoid the collapse in the Takahashi gas, the next level of approximation, which is the hard sphere case, is considered. The potential function of the hard sphere is shown below,

$$u(x) = \begin{cases} \infty, & x < a; \\ 0, & x > a. \end{cases} \quad (6-17)$$

The particles have been endowed with a hard diameter equal to  $a$  such that they cannot come closer than  $a$ . One can obtain the  $\kappa(P, T)$  integral and its derivative:

$$\kappa(P, T) = \frac{1}{\beta P} e^{-\beta P a} \quad \text{and} \quad \frac{\partial \kappa(P, T)}{\partial P} = -e^{-\beta P a} \left( \frac{1}{\beta P^2} + \frac{a}{P} \right). \quad (6-18)$$

Therefore, the volume per particle is given by

$$l = a + \frac{k_B T}{P}, \quad (6-19)$$

and then

$$P(l - a) = k_B T, \quad (6-20)$$

which is the exact equation of state for the one-dimensional hard sphere gas. Clearly at high temperatures, the first term on the right hand side in Eq. (6-19) can be neglected and the hard sphere gas behaves like an ideal gas. For low temperature, its behavior deviates from an ideal gas, because the isobars become flatter. At absolute zero for any pressure,

the close packed density  $1/a$  is obtained without any kind of collapse as seen in the ideal gas. On raising the temperature the density can only decrease from this state of the highest density, so there is no maximum in density at a nonzero temperature.

Now, consider an attractive potential with square well, which has a similar shape with the three-dimensional Lennard-Jones potential. The square well potential is given by

$$u(x) = \begin{cases} \infty, & 0 < x < a; \\ -\varepsilon, & a < x < 2a; \\ 0, & 2a < x < \infty, \end{cases} \quad (6-21)$$

where  $\varepsilon$  is the well depth and is greater than zero. The  $\kappa(P, T)$  integral can be done easily and is given by

$$\kappa = \frac{1}{\beta P} \theta [\phi + \theta(1 - \phi)], \quad (6-22)$$

where  $\theta = e^{-\beta Pa}$  and  $\phi = e^{\beta \varepsilon}$ . The volume per particle can be obtained before and after some algebra and the equation of state can be reduced to the form

$$P(l - a) = k_B T + \frac{Pa\theta(1 - \phi)}{\phi + \theta(1 - \phi)}. \quad (6-23)$$

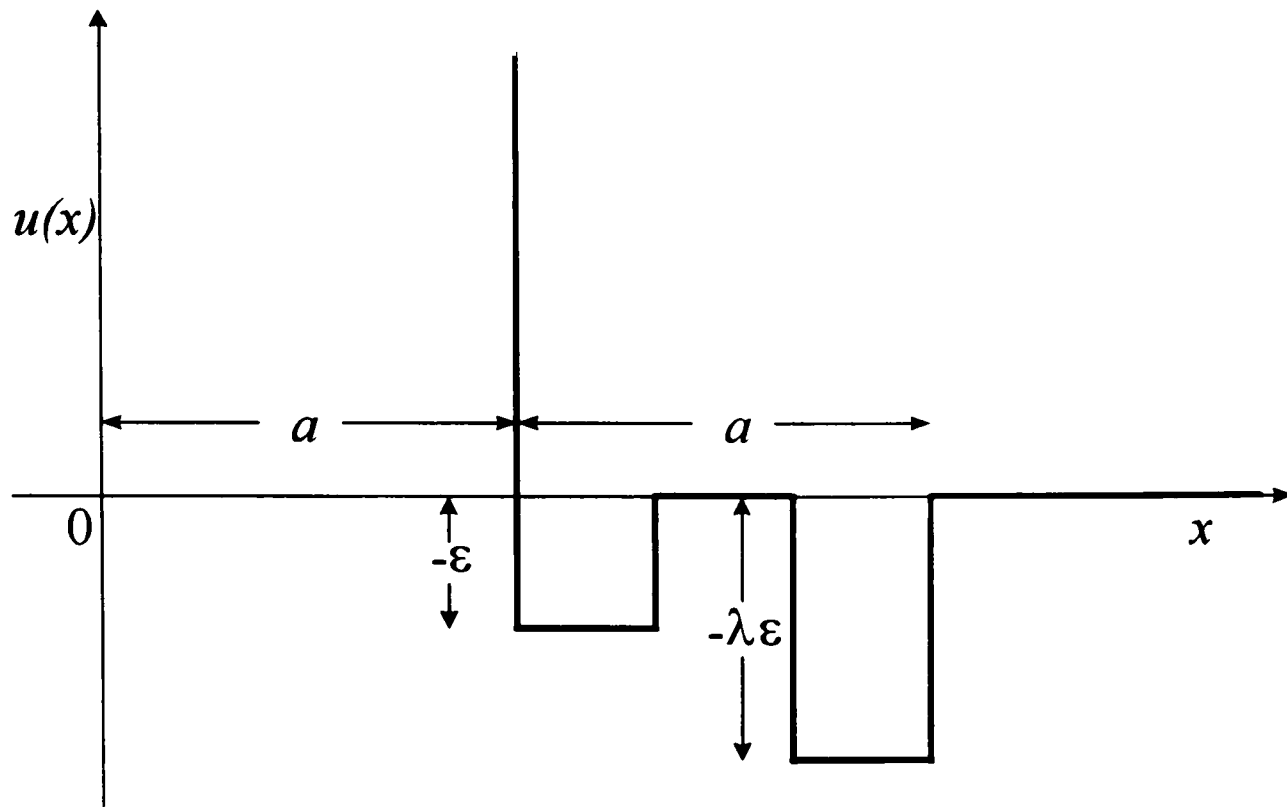
From this equation it is seen that for zero well depth  $\phi = 1$  and the hard sphere case is recovered. For zero temperature there is the crystalline configuration which sublimates into a gas as soon as the temperature is raised above zero. Thereafter, the volume just keeps on increasing with temperature, the gas approaching the ideal gas limit at high enough temperatures.

From these simple potentials, it is clear that to have a maximum density for a nonzero temperature, the system should not be in a state of close packed density.

However, a density maximum in the Takahashi model can be engineered in the following way. Suppose that, in addition to the hard core, there are two square wells in the potential, the one farther from the hard core being the deeper of the two. For zero pressure at  $T = 0$  K, the system exists in a crystalline state with all the particles in the outer well. A small pressure forces the particles into the inner well creating a higher overall density of the system. More interestingly, keeping the pressure fixed and raising the temperature, entropic and thermal effects start to become important. In this case, the particles tend to “boil” into the inner well, increasing the overall density. On further heating, the system expands so as to reach the ideal gas limit at sufficiently high temperatures. The initial density increase at low temperatures, followed by the expansion at high temperatures, then produces the density maximum.

### 6.3 The Double Well Potential Function

In the original Takahashi model [139,141] there is a hard core for  $0 < x < a$  and the potential is zero for  $x > 2a$ . Any analytically tractable potential can be used in the region  $a < x < 2a$ . In order to reproduce the second-neighbor characteristics of real water, we can therefore extend the Takahashi model to two wells, dividing the region between  $a$  and  $2a$  into three equal parts. These parts correspond to an inner well, a plateau and an outer well, respectively. The double well potential is shown below.



The potential can then be written,

$$u(x) = \begin{cases} \infty, & 0 < x < a; & \text{hard core,} \\ -\varepsilon, & a < x < 4a/3; & \text{inner well,} \\ 0, & 4a/3 < x < 5a/3; & \text{plateau,} \\ -\lambda\varepsilon, & 5a/3 < x < 2a; & \text{outer well,} \\ 0, & 2a < x < \infty. & \end{cases} \quad (6-24)$$

Here, it can be considered that the two second-neighbor wells in real water have been replaced by nearest-neighbor wells in the one-dimensional model. The quantities  $\lambda$  and  $\varepsilon$  are positive. The energy is measured in unit of the first well depth and the distance in unit of the hard core. The integral for  $\kappa(P, T)$  yields

$$\kappa(P, T) = \frac{1}{\beta P} \theta^3 [\phi + \theta(1 - \phi) - \theta^2(1 - \theta)(1 - \phi^2)], \quad (6-25)$$

where  $\theta$  and  $\phi$  have the same meaning as before. The volume per particle can be calculated as before. After simplifying the result and using Eq. (6-13), the equation of state becomes

$$P(l - a) = k_B T + \frac{Pa}{3} \frac{\theta[1 - \phi - \theta(2 - 3\theta)(1 - \phi^\lambda)]}{\phi + \theta(1 - \phi) - \theta^2(1 - \theta)(1 - \phi^\lambda)}. \quad (6-26)$$

It is easy to see that this equation reduces to the expected result in all appropriate limits, i.e., ideal gas, hard sphere, single well, etc.

Near absolute zero temperature,  $\theta$  is small and  $\phi$  is large. The equation of state then reduces to

$$P(l - a) \approx k_B T + \frac{2Pa}{3} \frac{\theta^2 \phi^{\lambda-1}}{1 + \theta^2 \phi^{\lambda-1}}. \quad (6-27)$$

In the case where the inner well is deeper than the outer well,  $\lambda \leq 1$  and the terms involving  $\phi$  vanish. Thus, the right hand side of Eq. (6-27) goes to zero as  $T \rightarrow 0$ , and the crystalline state of minimum volume,  $l = a$ , where all the spheres are touching, is obtained. On raising the temperature, the system simply expands and no density maximum occurs.

On the other hand, for the case of "water," where the outer well is deeper ( $\lambda > 1$ ), the terms involving  $\phi$  are dominant, and at  $T = 0$  K, the equation of state becomes

$$l - a \approx \frac{2a}{3} \frac{\theta^2}{\theta_c^2 + \theta^2}, \quad (6-28)$$

where  $\theta_c$  is defined through by the relationship,  $\phi^{1-\lambda} = \theta_c^2 = e^{-2\beta P_c a}$ . This gives rise to a “critical pressure”  $P_c = 3\varepsilon(\lambda - 1)/2a$ . It is then evident that at the zero temperature limit, the volume per particle is a discontinuous function of  $\theta$ ,

$$l = \begin{cases} a, & P > P_c; \\ 4a/3, & P = P_c; \\ 5a/3, & P < P_c. \end{cases} \quad (6-29)$$

Physically, these three possibilities correspond to all the particles being in the inner well, in both wells with equal probability, or in the outer well. At zero pressure and  $T = 0$  K, the system exists in a crystalline state with all the particles in the deeper, outer well, with  $l = 5a/3$ . Of course, as soon as the temperature is different from zero, the discontinuity in volume disappears and, as is normal for any substance, the volume is a continuous monotonously decreasing function of the pressure. However, for pressures lower than critical, there is a possibility that the density may show a maximum as a function of temperature. The application of pressure simply forces the particles into greater confinement, in this case into the inner well, creating a higher overall density, as in the dense ice polymorphs of the real system.

More interesting are temperature changes for pressures lower than critical. Keeping the pressure fixed at not too high a value and raising the temperature from  $T = 0$  K causes particles in the outer well to “boil” into the inner well, increasing the overall density. This effect, followed by the inevitable expansion at high temperatures, then produces a density maximum. As a specific example, we choose  $\lambda = 10$  and  $P = 10\varepsilon/a$ . Since this pressure is less than the critical pressure, which equals  $13.5\varepsilon/a$ , a

density maximum is obtained. This is seen in Figure 6.1, where  $\rho a/m$  is plotted as a function of  $k_B T/\epsilon$ .

Figure 6.2 shows the variation of densities with respect to temperature at various pressures. For higher pressures the maximum becomes broader and shifts to lower temperatures, finally disappearing at sufficiently high pressures, in this case  $P_c$ . This is exactly the type of behavior observed in real liquid water [146].

Though it is of course unrealistic to compare  $\rho(T)$  for the one-dimensional model with that of real water, it is of interest to note that by appropriate parameter scaling of the one-dimensional result, it is possible to match exactly the  $\rho(T)$  curve of real liquid water, both at normal and elevated pressures.

In conclusion, it has been shown that, by mapping the two known second neighbors in real liquid water onto first-neighbor locations in a one-dimensional model, a density maximum is obtained. The one-dimensional model also captures other pressure-temperature properties of this mysterious and important liquid. Since realistic density maxima are clearly absent in popular computational water models [78,79], it might be necessary, in order to reproduce the known temperature and pressure effects, to insert empirically the appropriate double-well feature into the water-water potential.

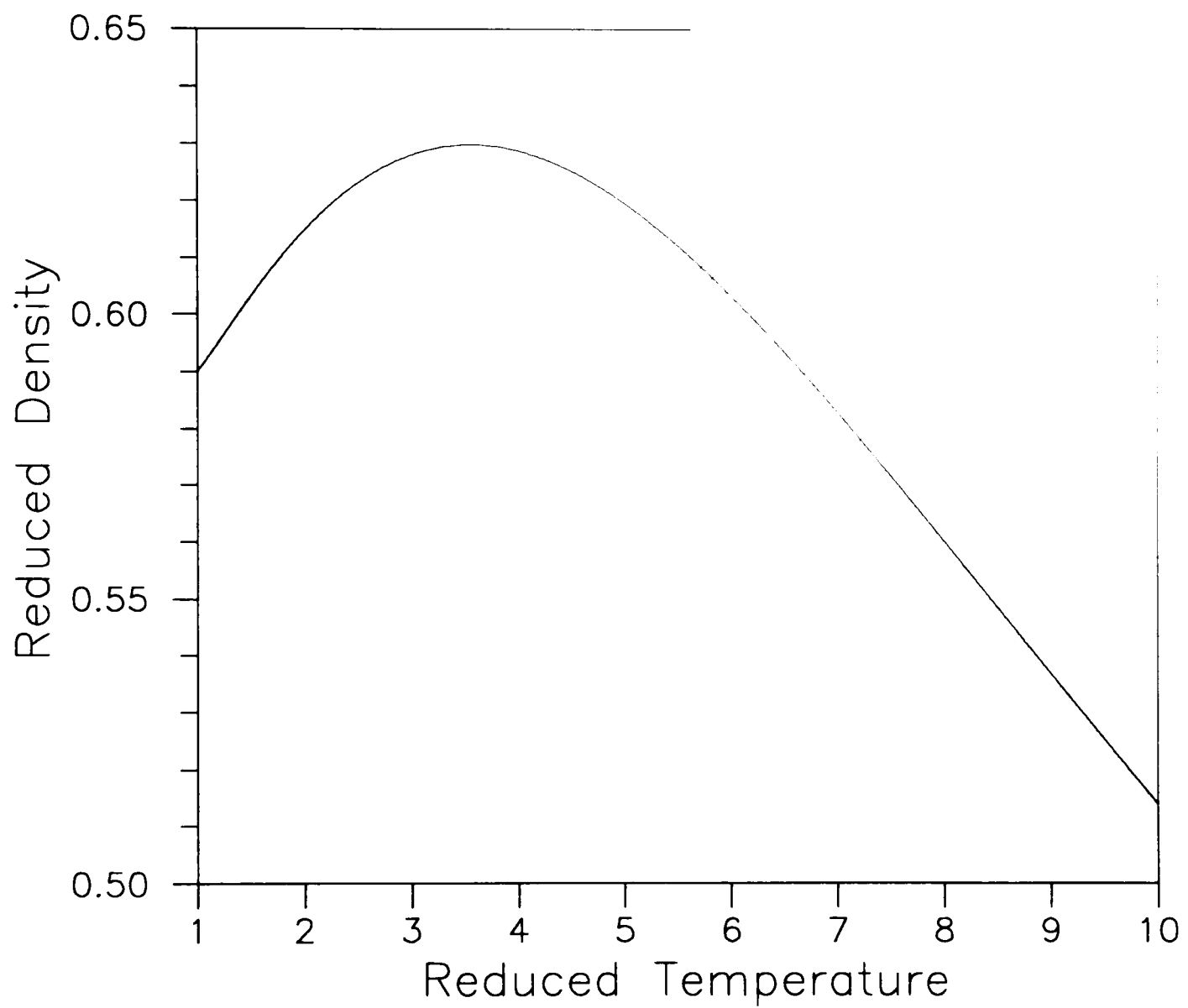


Figure 6.1. The reduced density  $\rho a/m$  as a function of reduced temperature  $k_B T/\epsilon$  for  $\lambda = 10$  and  $P = 10\epsilon/a$  for the 1-D double well potential model.

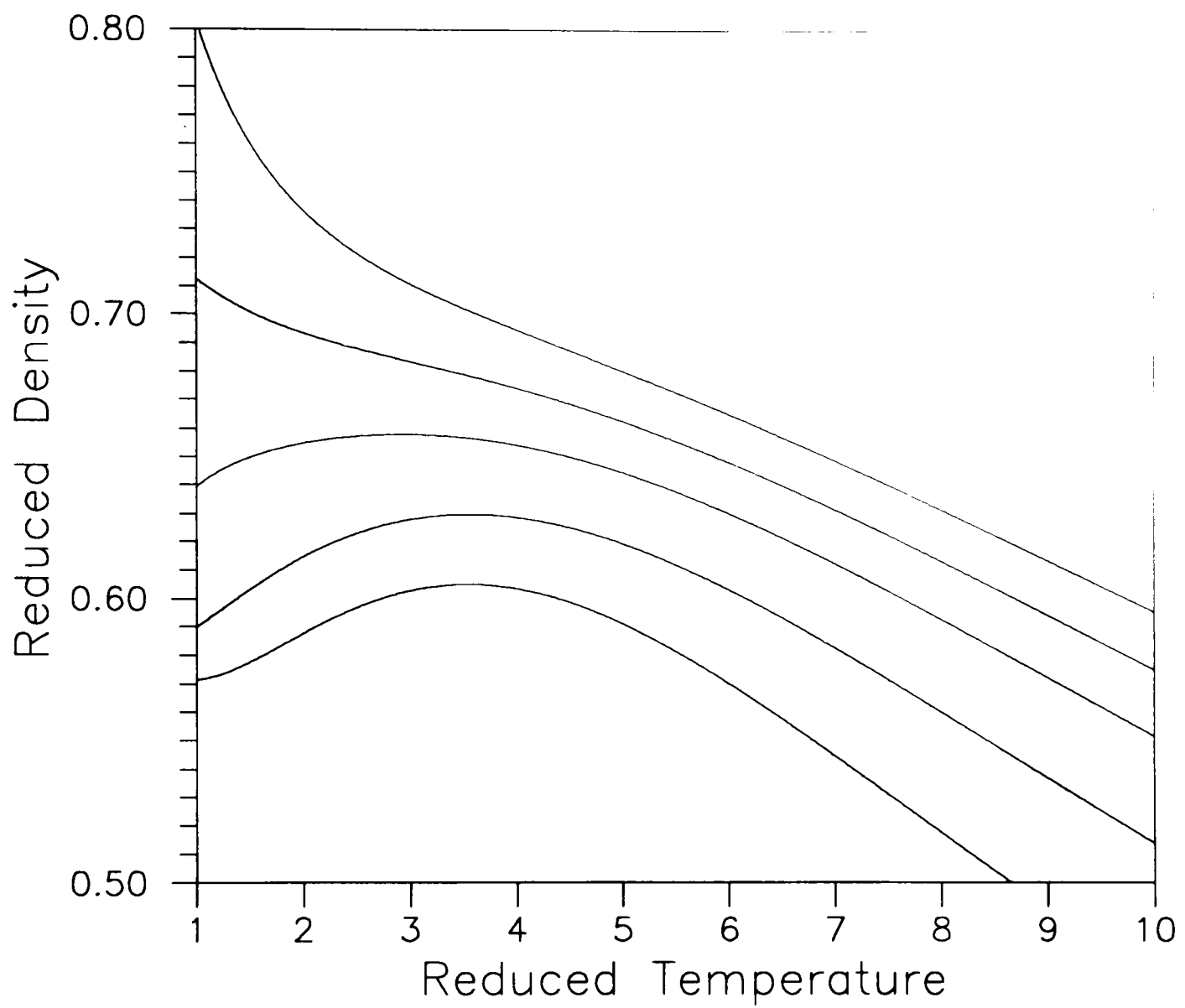


Figure 6.2. The variation of densities with respect to temperature at various pressures; Bottom to top  $P = 8, 10, 12, 13.5, 15$  for  $\lambda = 10$ . All quantities are used in reduced units.

## CHAPTER VII

### THREE-DIMENSIONAL POTENTIAL FOR WATER

It has been shown in an exactly soluble one-dimensional case that the existence of two dynamic states can give rise to a density maximum. Those two dynamic states can be described in terms of a competition between the presence of open second-neighbor oxygen-oxygen structure at 4.5 Å and a dense second-neighbor structure obtained from the bending of hydrogen bonds. This type of dense bonding is known to exist in the more stable higher density ice forms [77].

The dense structures have been missing in all previous theoretical attempts to understand the properties of liquid water. Therefore, in three dimensions, it should be accounted for phenomenologically by including another minimum in the potential in addition to the LJ well so that the outer potential minimum would correspond to the second-neighbor 4.5 Å distance, while the inner potential minimum corresponds to the second-neighbor 3.4 Å distance.

Since this approach has never been applied to computer simulations of water and no current water model can provide a realistic explanation of the density maximum, we propose altering the attractive water-water potential so as to obtain proper interactions in the second-neighbor region. This proposed potential function for MD simulations can solve the dynamical problems of liquid water. It also provides the key to a detailed understanding of water's "anomalous" characteristics. Using an NVE molecular dynamics

simulation, we will see if one can get a density maximum with this proposed potential function, which we will denote by the GWR potential model\*.

### 7.1 The New Potential Function of Water

If one uses a simple Lennard-Jones (LJ) potential for the oxygen atoms in typical molecular dynamics (MD) or Monte Carlo (MC) simulations, the density maximum of water cannot be reproduced. Typically, the LJ potential is an empirical formula that provides a reasonable description of the properties of argon-like fluids and is an approximation to the real argon potential, since atoms may have perfect spheres and their interactions may be described in a pairwise additive. So, the LJ potential always leads to monotonously decreasing density of any substances with increasing temperature.

Current water-water interaction models are mainly concerned with the formation and disruption of the tetrahedral structure at the nearest-neighbor level, with the hope that the longer range features will come out. To represent hydrogen bonding, long range attractive terms through charge-site interactions are included in the usual models. For example, one of the most widely used pair potentials in MD simulations for water is the extended simple point charge (SPC/E) potential which can be expressed [147] as

$$U_{\text{SPC/E}} = \frac{A}{r_{i_oj_o}^{12}} - \frac{B}{r_{i_oj_o}^6} + \sum_{n=1}^3 \sum_{m=1}^3 \frac{q_n q_m}{r_{i_nj_m}} \left[ 1 + \frac{1}{2} \left( \frac{r_{i_nj_m}}{r_c} \right)^3 \right], \quad (7-1)$$

---

\*Originally, this idea was suggested by Dr. G. Wilse Robinson who has devoted much of his recent life to the study of the water problem.

where the parameters  $A$  and  $B$  can be derived from the experimental dimer  $O\cdots O$  separation and binding energy, and the subscripts  $n$  and  $m$  represent O (1) or H (2 or 3) atoms of the  $i$ th and  $j$ th molecules, respectively. Here the equation (7-1) uses the reaction field approach to correct for the polarizability of water. It is assumed that  $\epsilon_{RF} = \infty$ , because the dielectric constant of water is very high. In the above equation,  $q$  is the appropriate point charge on O or H atom,  $r_c$  is the potential cutoff distance, and  $r_{i_n j_m}$  is the distance between atom  $n$  of the  $i$ th molecule and atom  $m$  of the  $j$ th molecule.

Unfortunately, the Coulomb terms from the above equation dominate the LJ interaction in the 3.4 Å region and, hence, no role has ever been played by second-neighbor interactions in current water-water interaction models. It is no wonder then that none of them is able to provide a realistic density maximum [78,79]! Therefore, the LJ term in the water-water potential should be modified so as to provide a second-neighbor  $O\cdots O$  minimum near 3.4 Å.

The initial form of the new water potential will be chosen to be one that is as simple as possible so that it can be used for interfacial studies of chemical and biological systems. This is required because the molecular-level structural and dynamic properties of a realistically modeled surface are themselves so very computationally intensive. Avoiding an explicit angular dependent interaction is desired in order to reduce computer time substantially.

A simple 3-site model will be considered here for computational investigations of bulk water. As shown in Figure 7.1, the pairwise intermolecular potential between

molecule 1 and molecule 2 has one O···O, four H···H, and four O···H contributions, together with long range Coulomb interactions from the dipole and quadrupole moments of the water molecules. Coulomb interactions can be introduced through a hyperbolic tangent “switching function” by including a point dipole and a point quadrupole centered on the true electrical center-of-charge in each molecule. In this study, the long range Coulomb interactions will be omitted initially, since it is felt that the local and outer structure in the liquid is not too sensitive to their presence, and the first goal is to obtain realistic representations of more local properties, such as the radial distribution function and the thermodynamic properties, but not the dielectric properties.

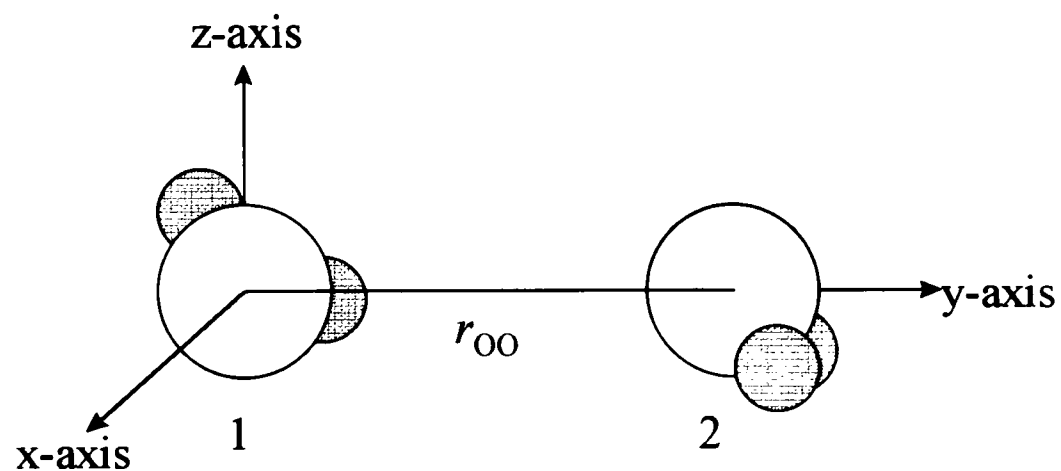


Figure 7.1. The coordinate system used to the water dimer interaction. The big circle stands for oxygen and the small shaded ones for hydrogens.

The four distinct H···H interactions ( $U_{HH}$ ),  $H'_1 \cdots H'_2$ ,  $H'_1 \cdots H''_2$ ,  $H''_1 \cdots H'_2$ , and  $H''_1 \cdots H''_2$  have a standard LJ form. The four O···H interactions ( $U_{OH}$ ),  $O_1 \cdots H'_2$ ,  $O_1 \cdots H''_2$ ,  $O_2 \cdots H'_1$ , and  $O_2 \cdots H''_1$  are Morse-like potentials, while the  $O_1 \cdots O_2$  ( $U_{OO}$ )

interaction has a  $r^{-12}$  repulsive form together with an attractive Gaussian function. Thus, the mathematical forms for the proposed GWR potential have the following forms,

$$\begin{aligned}
 U_{OO} &= 4\epsilon_{OO} \left[ \left( \frac{\sigma_{OO}}{r_{OO}} \right)^{12} - \frac{1}{2} e^{-\beta (r_{OO} - d_{OO})^2} \right], \\
 U_{HH} &= 4\epsilon_{HH} \sum \left[ \left( \frac{\sigma_{HH}}{r_{HH}} \right)^{12} - \left( \frac{\sigma_{HH}}{r_{HH}} \right)^6 \right], \\
 U_{OH} &= D_M \sum \left[ 2e^{-\alpha_1 (r_{OH} - \delta_1)} - \frac{1}{1 + e^{\alpha_2 (r_{OH} - \delta_2)}} \right].
 \end{aligned} \tag{7-2}$$

In the  $U_{HH}$  and  $U_{OH}$  equations, the summations are over the four interactions noted. Then, the total potential of intermolecular interactions between any pair of water molecules is given by the summations over the nine atomic interactions,

$$U_{ij} = U_{OO} + U_{HH} + U_{OH}. \tag{7-3}$$

In Table 7.1 is given the values of the parameters of the GWR potential for liquid water tested in the NVE MD simulation. The GWR potential function will be optimized to get the best simulation results.

Using the parameters in Table 7.1, the shape of the GWR potential together with the popular SPC/E potential model [147] is shown in Figure 7.2. The intermolecular interaction used here is the hydrogen-bonded like configuration as shown in Figure 7.1. The potential curves are plotted against  $r_{OO}$  along the O—H...O bond direction being y-axis. The SPC/E potential gives a good account of the local properties of pure water, such as the radial distribution function (RDF) up to around 3 Å. The much shallower potential in the new model is meant to match approximately the quantum mechanical

Table 7.1. The Parameters of the GWR Potential for Liquid Water.

$\epsilon_{\text{OO}}$	0.83 kJ/mol	$D_{\text{M}}$	55.0 kJ/mol
$\sigma_{\text{OO}}$	3.03 Å	$\alpha_1$	2.50 Å <sup>-1</sup>
$\beta$	0.80 Å <sup>-2</sup>	$\delta_1$	1.00 Å
$d_{\text{OO}}$	3.80 Å	$\alpha_2$	4.80 Å <sup>-1</sup>
$\epsilon_{\text{HH}}$	0.132 kJ/mol	$\delta_2$	2.00 Å
$\sigma_{\text{HH}}$	2.34 Å		

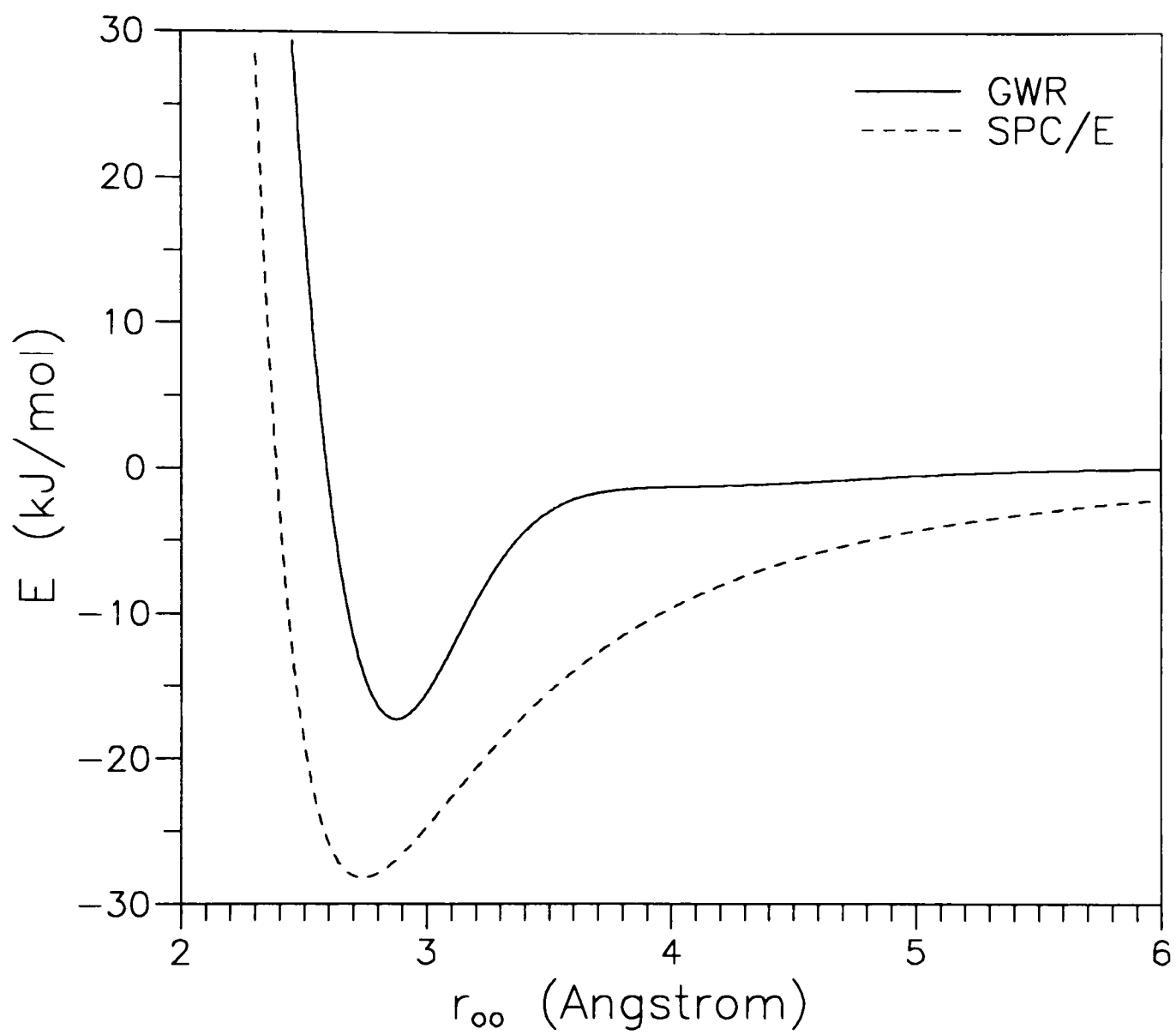


Figure 7.2. The comparison of the GWR potential with the SPC/E potential.

dimer energy of about  $-18.5\text{kJ/mol}$  [148]. Unlike the SPC/E model, the dimer H-bond energy in the GWR potential is not obtained from the assumption that it is half the lattice energy of ice Ih ( $56.0\text{kJ/mol}$ ), which of course includes non-H-bonded, many-body and long-range effects.

Interestingly, our shallow but narrow potential, with good outer-neighbor structure, gives a first peak RDF similar to that from the deep and wide SPC/E potential from the preliminary calculation. The distance-dependent Coulomb interactions are in principle already included in the quantum mechanical results, but they only attain their  $r^{-3}$  (dipole-dipole),  $r^{-4}$  (dipole-quadrupole) or  $r^{-5}$  (quadrupole-quadrupole) forms at distances where the valence interactions have become small. This is the reason that the Coulomb interactions are not switched on strongly until about  $4\sim 5\text{ \AA}$ .

Since the angular dependence is internally built in the GWR pair potential, it is possible to compare with the pair potential, SPC/E. Either water molecule 1 or 2 in Figure 7.1 is rotated counterclockwise around its x-, y-, and z-coordinate, and then its angular dependent potentials are given for two important O...O distances, the H-bond distance of  $2.8\text{ \AA}$  in Figures 7.3-7.6 and the outer neighbor distance near  $3.8\text{ \AA}$  in Figures 7.7-7.11 for the GWR potential (solid line) and the SPC/E potential (dashed line). Though the potentials seem qualitatively different, some angular dependence in the two models is very similar under appropriate choice of parameters. Through these comparisons, better informed adjustments of the parameters (or the form of the potential function itself) can be made, while at the same time not steering too far from SPC/E, a water-water potential that provides a good representation of the local interactions.

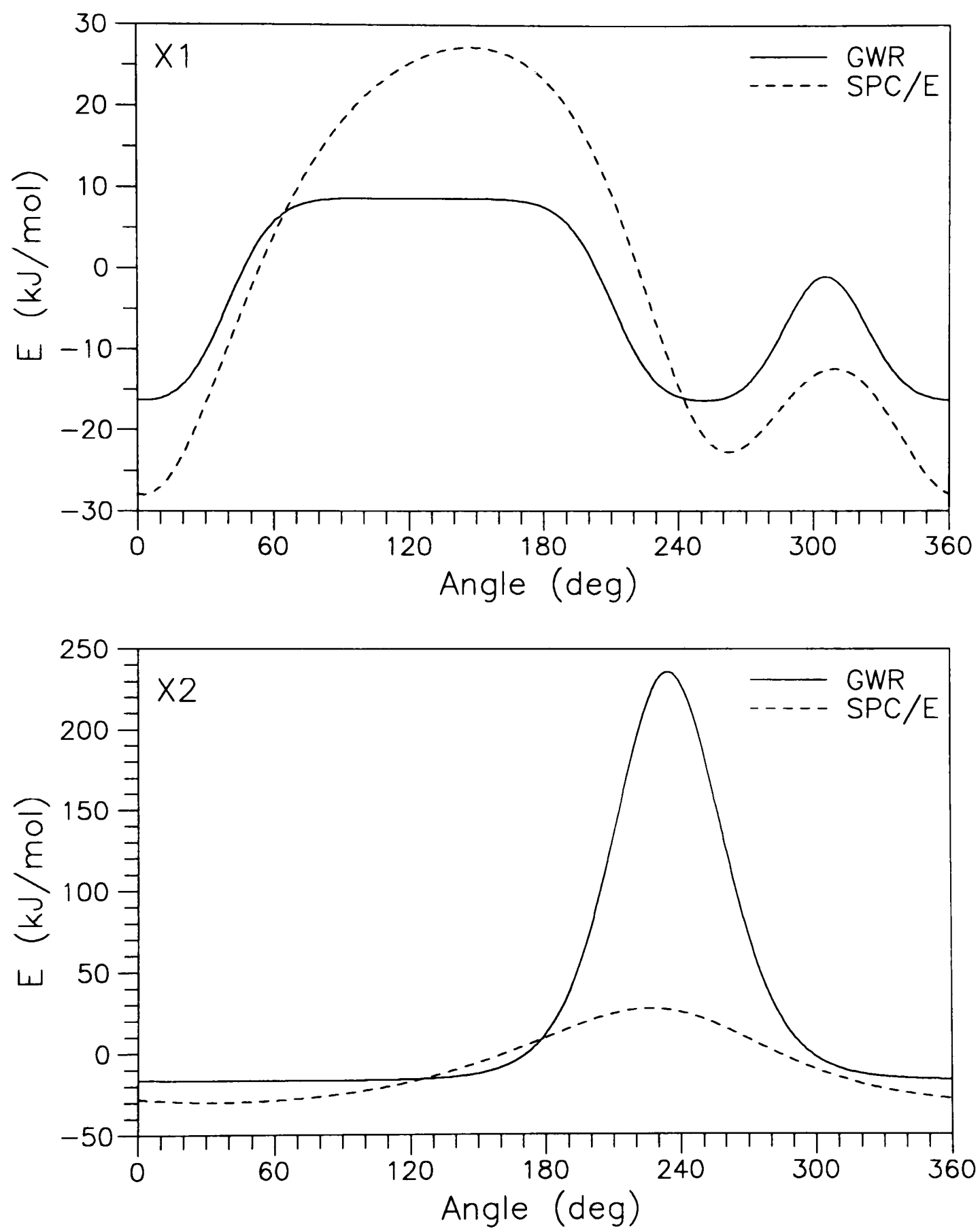


Figure 7.3. The angular dependent potentials of water molecule 1 (top) and 2 (bottom) rotated around x-axis at 2.8 Å.

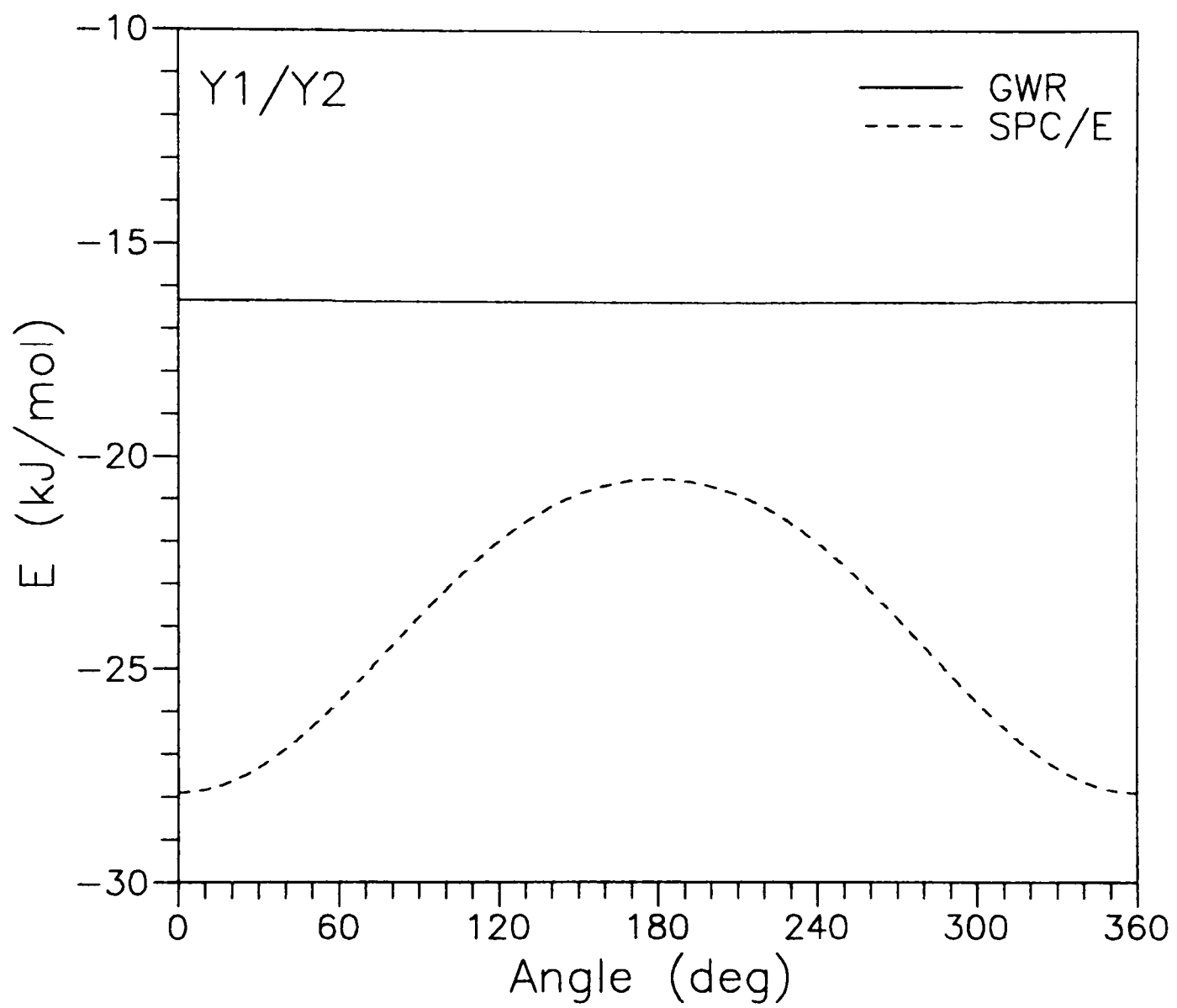


Figure 7.4. The angular dependent potentials of water molecule 1 or 2 rotated around y-axis at 2.8 Å.

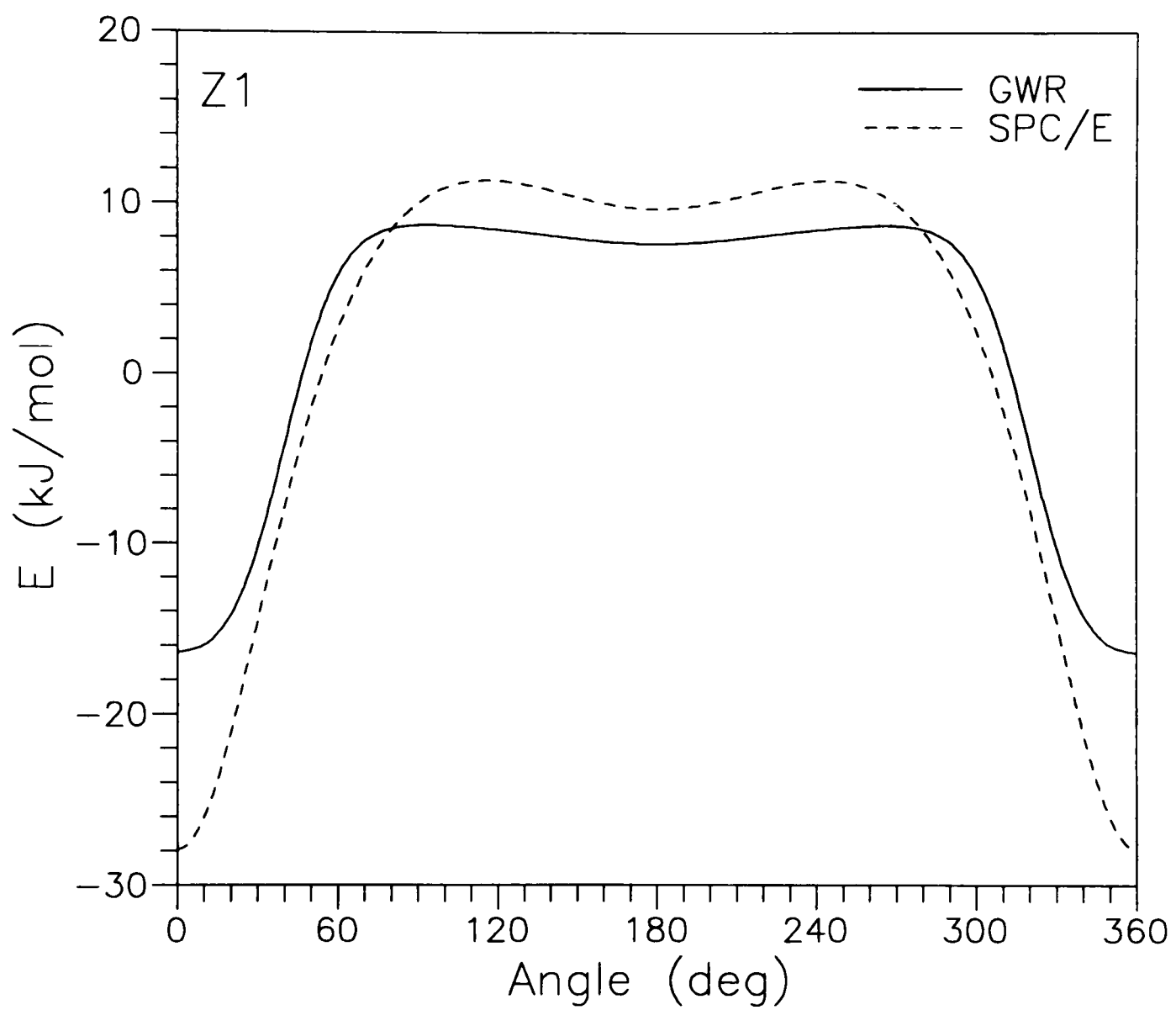


Figure 7.5. The angular dependent potentials of water molecule 1 rotated around z-axis at 2.8 Å.

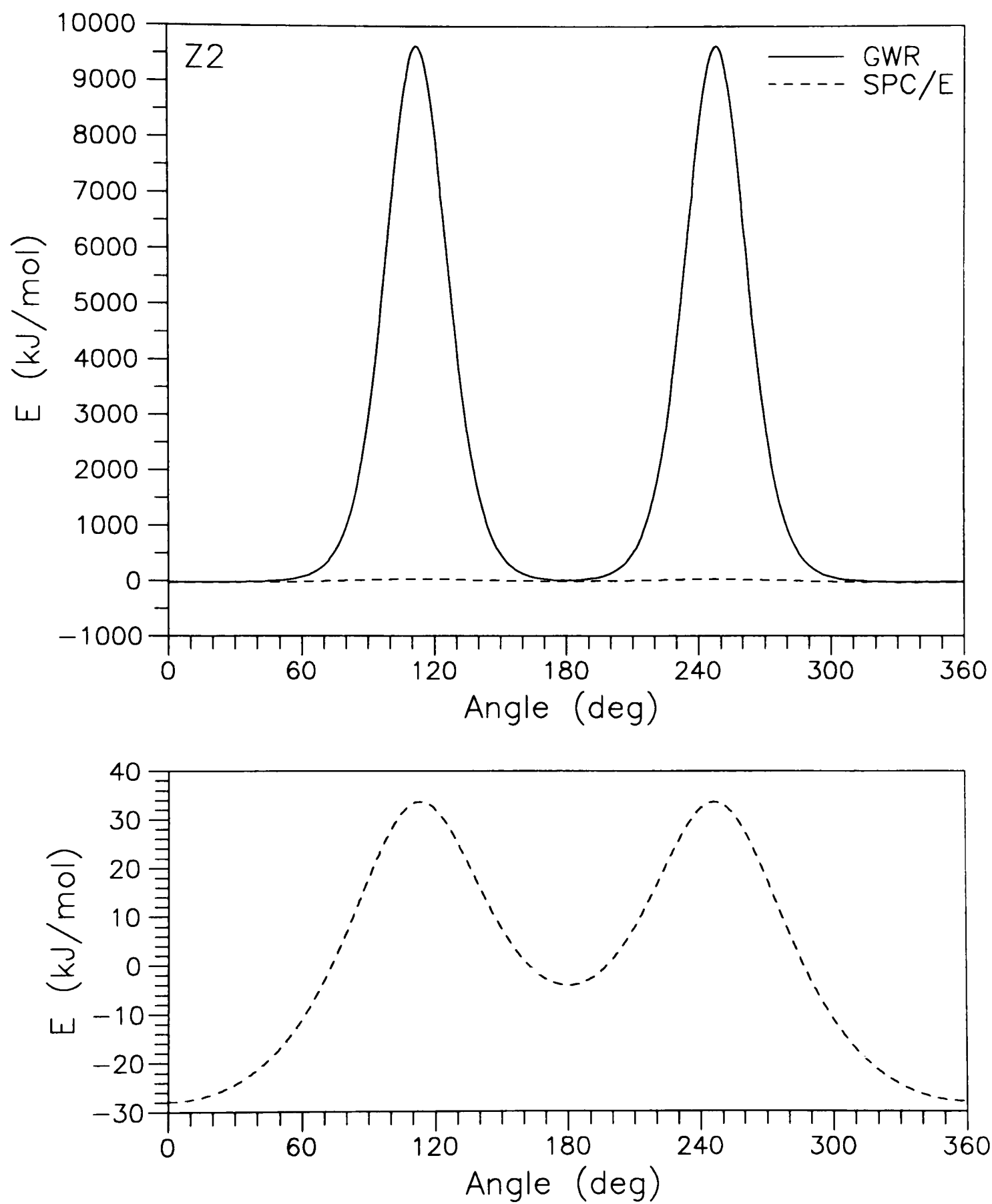


Figure 7.6. The angular dependent potentials of water molecule 2 rotated around z-axis at 2.8 Å, with extended scale (bottom).

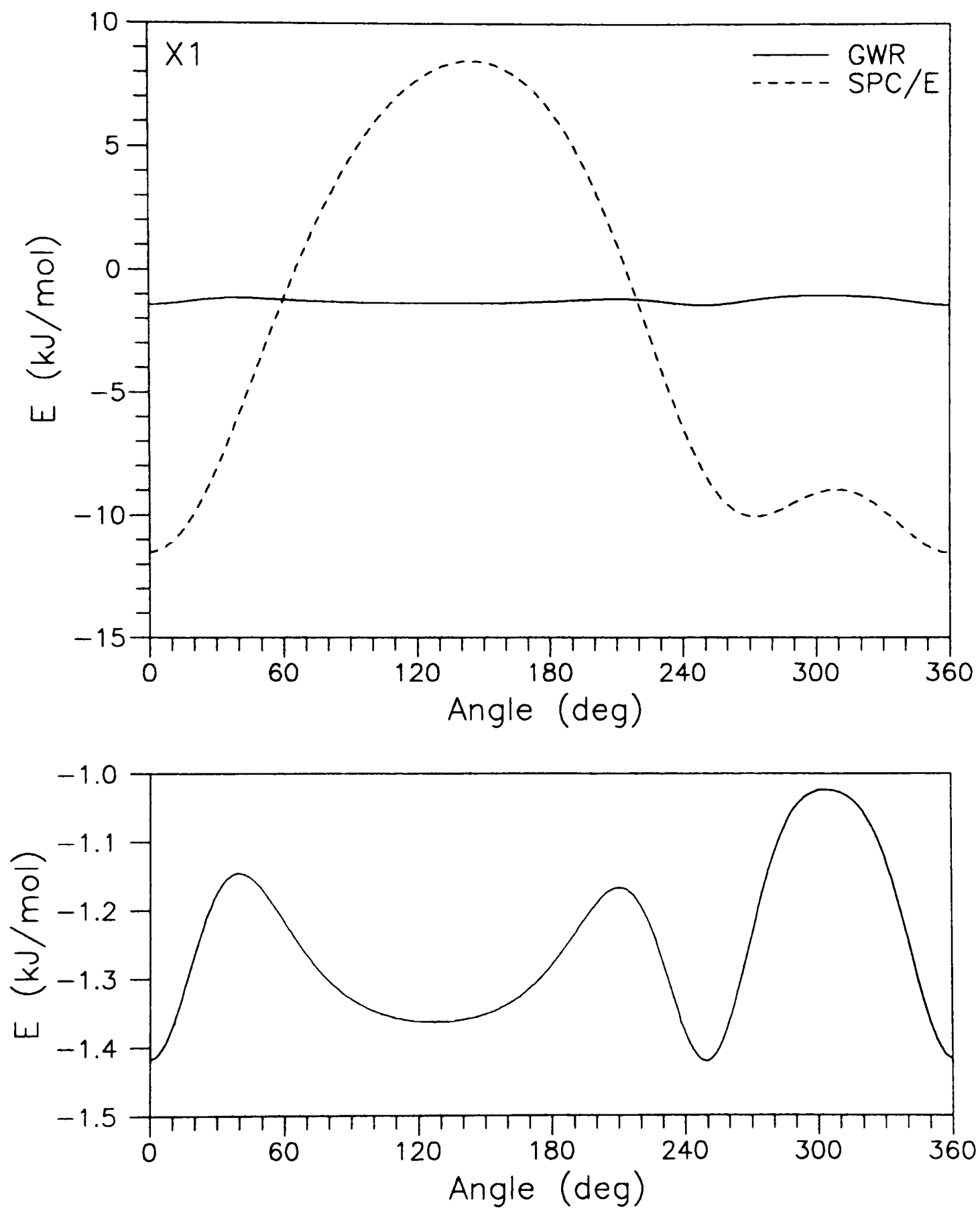


Figure 7.7. The angular dependent potentials of water molecule 1 rotated around x-axis at 3.8 Å, with extended scale (bottom).

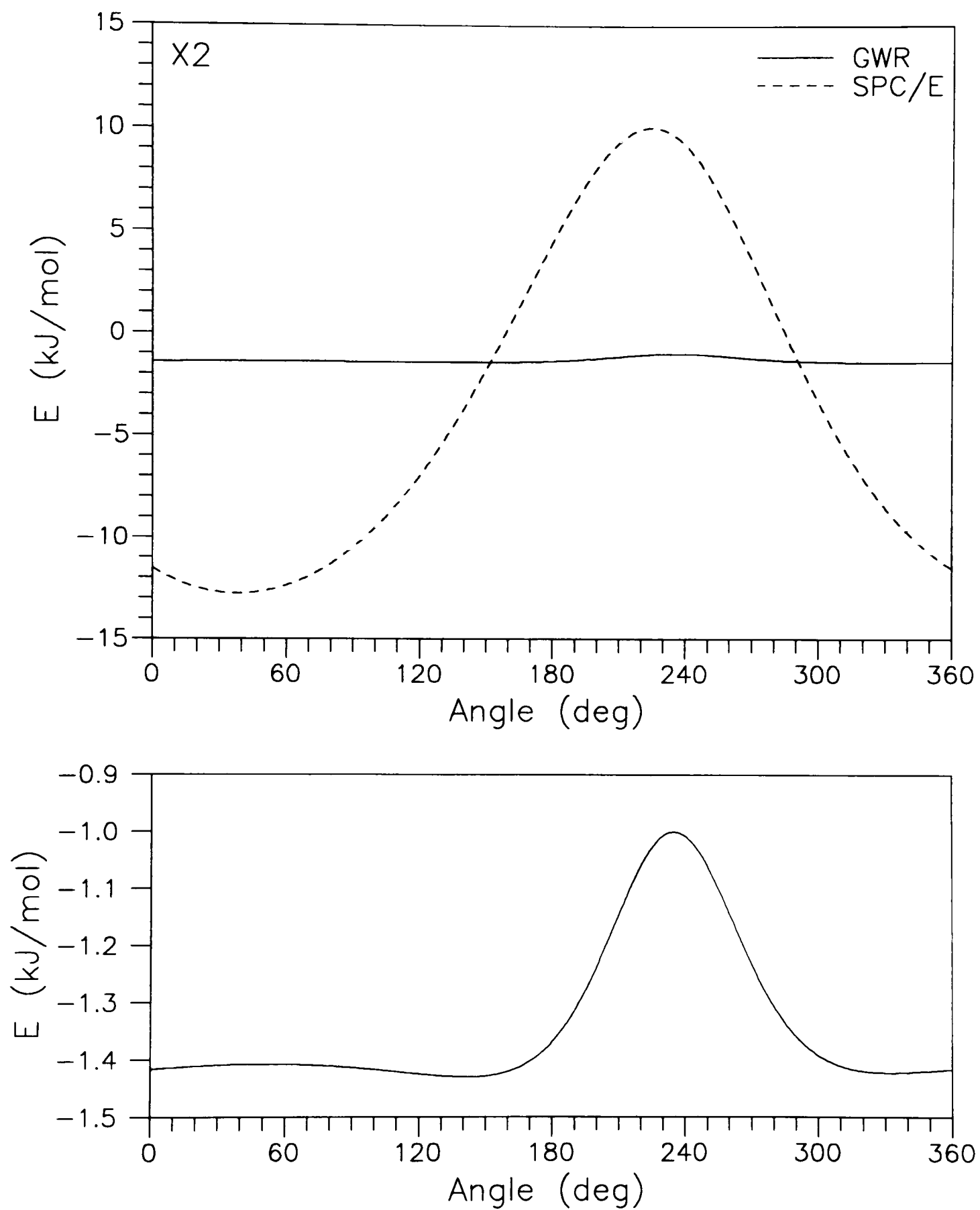


Figure 7.8. The angular dependent potentials of water molecule 2 rotated around x-axis at 3.8 Å, with extended scale (bottom).

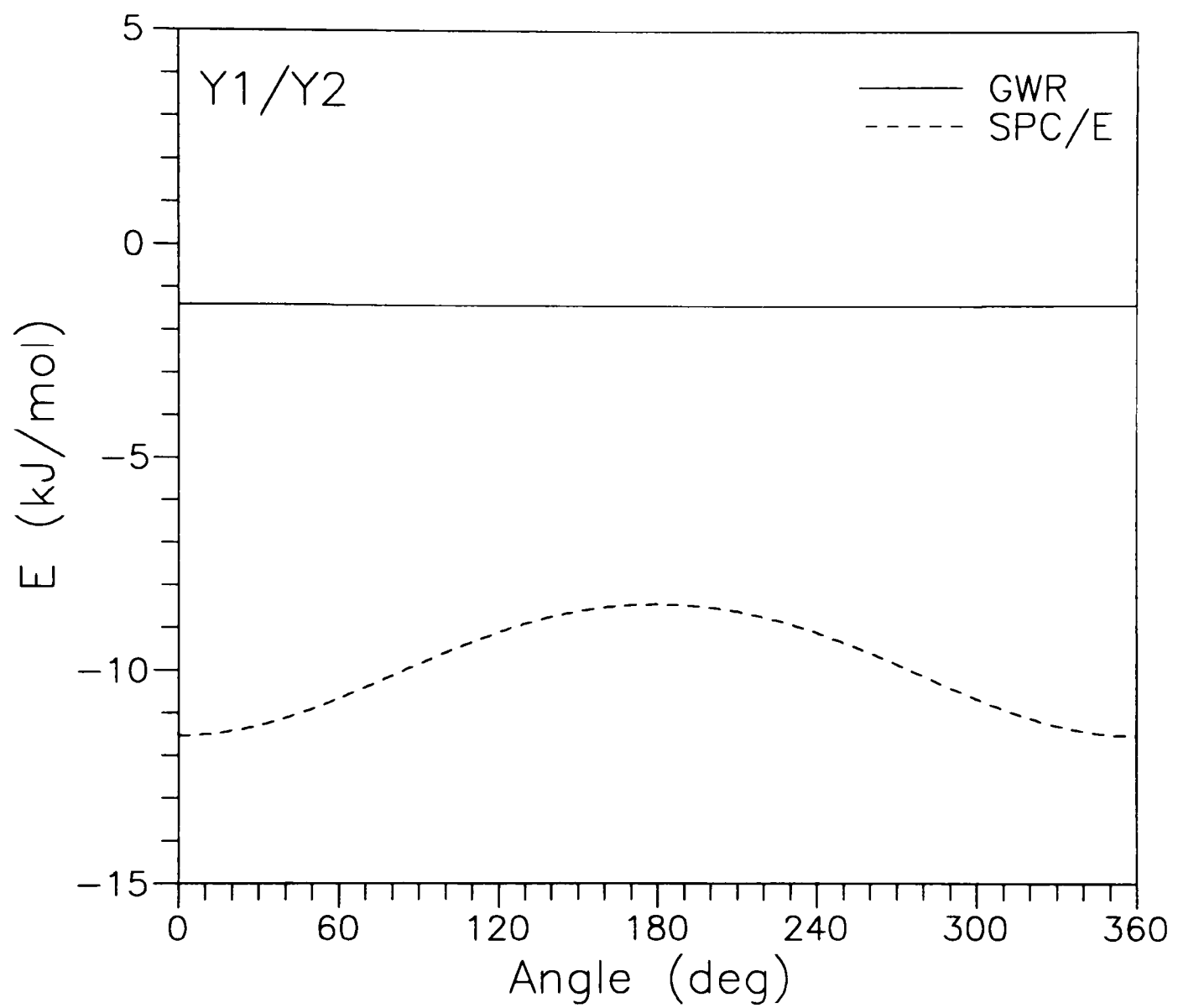


Figure 7.9. The angular dependent potentials of water molecule 1 or 2 rotated around y-axis at 3.8 Å.

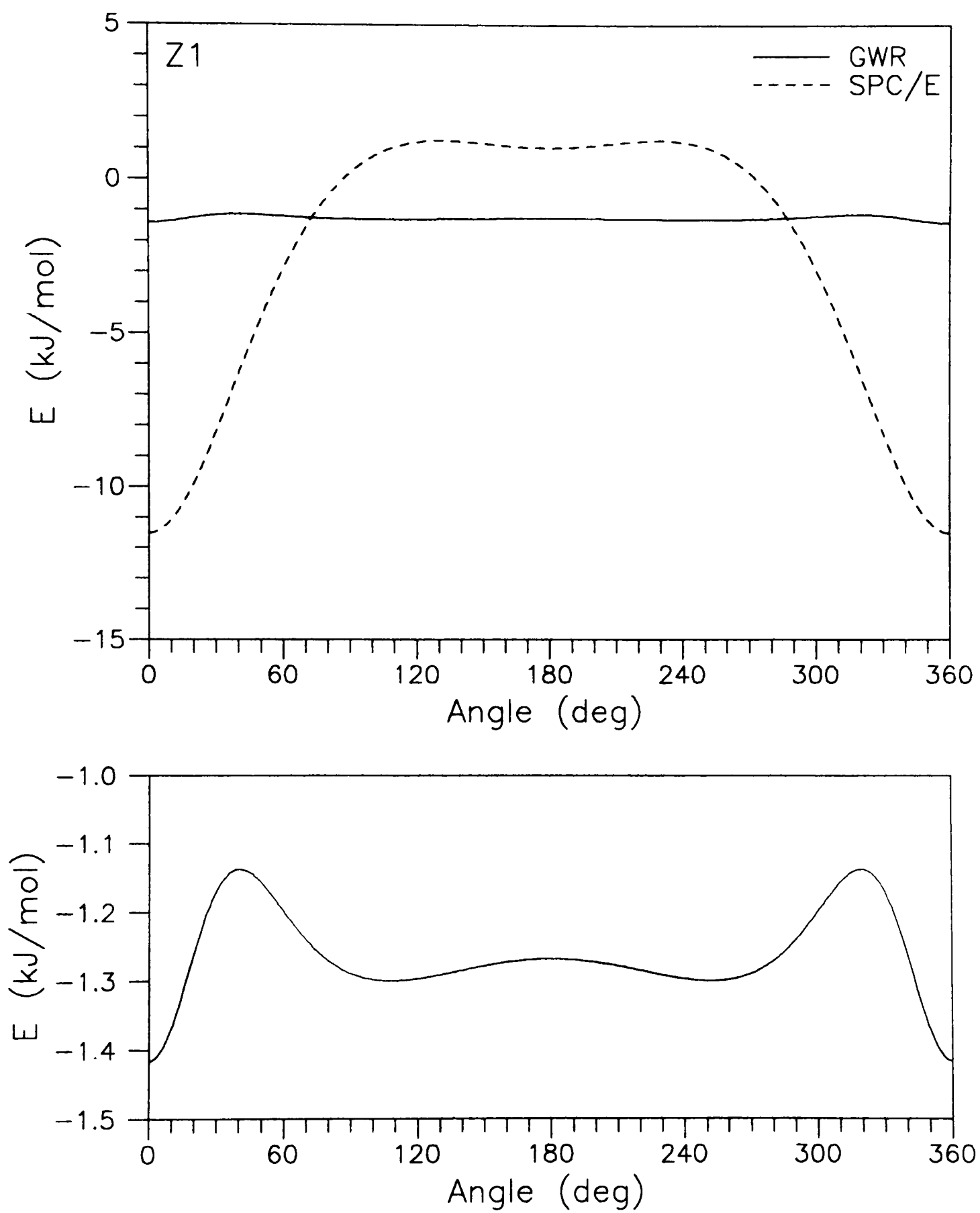


Figure 7.10. The angular dependent potentials of water molecule 1 rotated around z-axis at 3.8 Å, with extended scale (bottom).

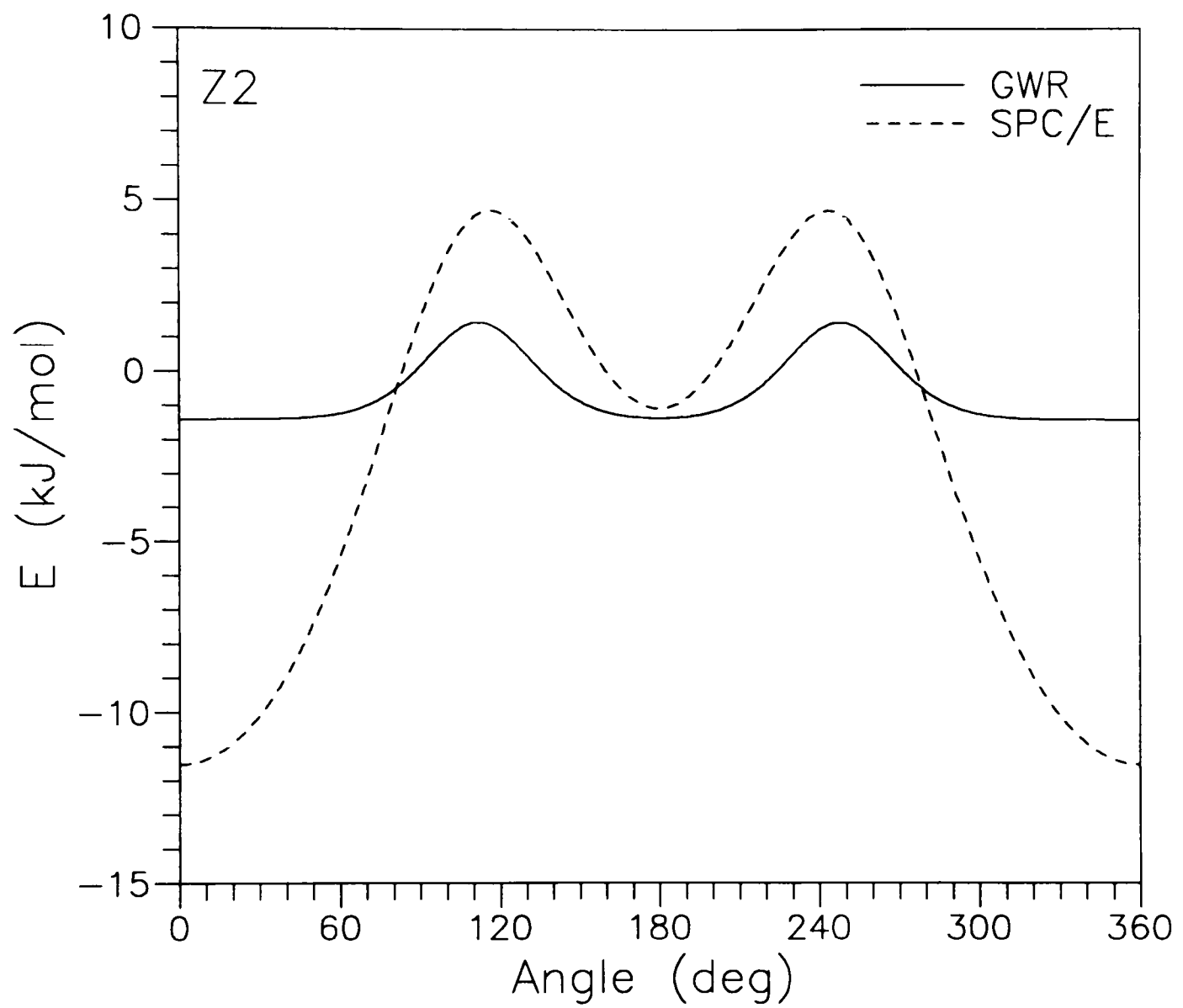


Figure 7.11. The angular dependent potentials of water molecule 2 rotated around z-axis at 3.8 Å.

Figure 7.3 shows the angular dependent potentials of water molecules 1 and 2 which are rotated around the x-axis near the potential minimum of 2.8 Å, respectively. As is the case for other models, the GWR model gives a strong hydrogen-bond interaction along the O—H···O direction. However, unlike all previous models, the H-bond interaction rather sharply disappears for angles away from this direction and for O—H···O distances greater than 2.8 Å. Notice that there is a huge repulsion when hydrogen atoms come close to each other as seen from Figures 7.3 (bottom) and 7.6. This configuration does not occur in any ice form near 2.8 Å.

From Figures 7.7 and 7.10, the shallow minimum at 3.8 Å for a large range of angles should be noted for the GWR potential, but not SPC/E. With the huge potential hill in the SPC/E model, there is no way that the desired outer structure will form.

Away from the H-bond regions of the potential, the water-water potential is supplanted by an O···O attractive interaction with a minimum near 3.8 Å, so that the higher density ice polymorphs and liquid structures can be realistically reproduced. The outer structure from the total potential is thus characterized by a double minimum: open tetrahedral structure with a next-nearest-neighbor O···O distance of 4.5 Å and a bent structure with an O···O non-H-bonded distance at about 3.8 Å.

The source of the 3.8 Å potential minimum in the GWR potential model is the O···O van der Waals interaction, which, as discussed by Kamb [77], is somewhat deeper than that ordinarily expected for the electronic size of the water molecule. Kamb reports a van der Waals stabilization energy, compared with ordinary ice, of 1.7~2.5 kJ/mol for the

second most stable ice form, ice II. This van der Waals interaction thus helps stabilize the bent hydrogen bonded structure. It is to be noted here that, in spite of the fact that half the H-bonds in ice II are strongly bent away from tetrahedral ( $109.45^\circ$ ), some to as small an angle as  $80^\circ$ , the internal energy difference ( $\Delta E$ ) between ordinary ice and ice II is only 0.08 kJ/mol, thirty times less than  $k_B T$  at room temperature!

### 7.2 The NVE MD Simulation

The MD computer simulation is a powerful tool for obtaining information on the molecular-scale behavior of a model system. This can also be helpful at stages of experimental data analysis that are aimed at optimizing a potential function which agrees with observed experimental information. In particular, the availability of a tested intermolecular potential function makes it possible to study the static and dynamic properties of interfacial water at microscopic levels.

Following the early MC calculations carried out by Metropolis et al. [149], the methods and algorithms of MC and MD have rapidly developed and have been applied to a number of models. Originally, MD and MC simulations were restricted to the microcanonical (NVE) ensemble. Later, Andersen [150] showed how to use other ensembles such as canonical (NVT) and isobaric-isoenthalpic (NPH). He proposed a way of introducing adiabatic volume fluctuations into a mixed MC/MD algorithm such that the pressure and temperature become independent state variables. Simultaneously and independently, Evans and Morriss [151,152] developed an MD algorithm for the

isothermal-isobaric (NPT) ensemble. All those methods are fully discussed in the book by Allen and Tildesley [143].

Even though we are ultimately interested in studying the variation of the density of water as a function of temperature  $T$  at a certain pressure  $P$ , we are going to restrict the computer simulation into an NVE ensemble in this study. The main reason is that the proposed potential function needs to be optimized with an algorithm that uses very little computer time. Here we will test the GWR potential function to give the pressure minimum with respect to temperature in the NVE ensemble, which corresponds to the density maximum with respect to temperature in the NPT ensemble.

### 7.2.1 Equations of Motion

To study the dynamics of a system, the simplest method is to use an NVE or microcanonical ensemble, in which the total energy is conserved while the size of the basic cell and the number of particles remain constant. The water molecules are considered as nonlinear rigid molecules with a fixed O...H bond length ( $d_{\text{OH}} = 1.0 \text{ \AA}$ ) and an internal angle  $\angle \text{OHO}$  being the tetrahedral angle ( $109.45^\circ$ ) in this simulation. The most general motion of water molecules is a translation of the center of mass (c.m.) and a rotation about the c.m.

The Hamiltonian of the system [143] may be written by a sum of kinetic and potential energies,

$$H = K + U . \quad (7-4)$$

The total potential energy from Eq. (7-3) is given by

$$U = \sum_i \sum_{j>i} U_{ij}, \quad (7-5)$$

and the total kinetic energy at a given time is written by

$$K = \frac{1}{2} \sum_i \frac{p_i^2}{M} + \frac{1}{2} \sum_i \left( \frac{L_{ix}^2}{I_{xx}} + \frac{L_{iy}^2}{I_{yy}} + \frac{L_{iz}^2}{I_{zz}} \right), \quad (7-6)$$

where  $M$  is the total mass  $m_O + 2m_H$ ,  $I_{xx}$ ,  $I_{yy}$  and  $I_{zz}$  are the three principal moments of inertia of the molecule around its c.m., and  $L_i$  is the angular momentum of each molecule.

Equations of translational motion of the c.m. are

$$\dot{r}_i = \frac{p_i}{M}, \quad (7-7)$$

$$\dot{p}_i = F_i, \quad (7-8)$$

where  $r_i$ , and  $p_i$  are Cartesian coordinates and momenta, and  $F_i$  is the total force acting on a molecule  $i$  due to all others, with a pairwise potential function  $U_{ij}$ ,

$$F_i = - \sum_{j=1}^N \frac{\partial U_{ij}}{\partial r_i}, \quad (7-9)$$

where  $N$  is the number of molecules. In a molecular system, Eq. (7-9) can be rewritten in the form

$$F_i = \sum_{a=1}^{n_a} F_{ia}, \quad (7-10)$$

where  $F_{ia}$  is the force acting on atom  $a$  in the molecule and  $n_a$  is the number of atoms per molecule.

The rotational motions are governed by the vector sum of all the torques about the c.m., which is defined by

$$\tau_i = \sum_a \mathbf{d}_{ia} \times \mathbf{F}_{ia} \quad (7-11)$$

on each molecule. Here  $\mathbf{d}_{ia} = \mathbf{r}_{ia} - \mathbf{r}_i$  is the atomic position relative to the c.m. position of molecule  $i$ .

Usually, the orientation of nonlinear molecules can be described by terms of the Euler angles  $(\phi, \theta, \psi)$ . Since the use of these angles causes singularity in the equations of motion whenever  $\theta$  approaches 0 or  $\pi$ , a quaternion  $\mathbf{Q}$ , as a set of four scalar quantities, suggested by Evans [153], will be used to represent the orientation of a rigid body:

$$\mathbf{Q} = (q_0, q_1, q_2, q_3), \quad (7-12)$$

such that

$$q_0^2 + q_1^2 + q_2^2 + q_3^2 = 1. \quad (7-13)$$

By Goldstein's convention of the Euler angles [154], quaternions can be defined by

$$\begin{aligned} q_0 &= \cos \frac{\theta}{2} \cos \frac{\phi + \psi}{2}, \\ q_1 &= \sin \frac{\theta}{2} \cos \frac{\phi - \psi}{2}, \\ q_2 &= \sin \frac{\theta}{2} \sin \frac{\phi - \psi}{2}, \\ q_3 &= \cos \frac{\theta}{2} \sin \frac{\phi + \psi}{2}. \end{aligned} \quad (7-14)$$

The components of a unit vector  $\mathbf{e}_i^b$  for molecule  $i$  in the body-fixed coordinate system are related by its components  $\mathbf{e}_i^s$  in the space-fixed coordinates,

$$\mathbf{e}_i^b = \mathbf{A} \cdot \mathbf{e}_i^s, \quad (7-15)$$

where  $\mathbf{A}$  is the rotational matrix of quaternions, which describes the rotation of the molecular-fixed vector in the body-fixed coordinates:

$$A = \begin{pmatrix} q_0^2 + q_1^2 - q_2^2 - q_3^2 & 2(q_1q_2 + q_0q_3) & 2(q_1q_3 - q_0q_2) \\ 2(q_1q_2 - q_0q_3) & q_0^2 - q_1^2 + q_2^2 - q_3^2 & 2(q_2q_3 + q_0q_1) \\ 2(q_1q_3 + q_0q_2) & 2(q_2q_3 - q_0q_1) & q_0^2 - q_1^2 - q_2^2 + q_3^2 \end{pmatrix}. \quad (7-16)$$

The atomic positions in the space-fixed system are then given by

$$r_{ia}^s = r_i^s + A \cdot d_a. \quad (7-17)$$

The equations of motion of the quaternions [153] are

$$\begin{pmatrix} \dot{q}_0 \\ \dot{q}_1 \\ \dot{q}_2 \\ \dot{q}_3 \end{pmatrix} = \frac{1}{2} \begin{pmatrix} q_0 & -q_1 & -q_2 & -q_3 \\ q_1 & q_0 & -q_3 & q_2 \\ q_2 & q_3 & q_0 & -q_1 \\ q_3 & -q_2 & q_1 & q_0 \end{pmatrix} \begin{pmatrix} 0 \\ \omega_x^b \\ \omega_y^b \\ \omega_z^b \end{pmatrix}, \quad (7-18)$$

and the equations of angular motion in the body-fixed coordinates are

$$\begin{aligned} \dot{\omega}_x^b &= \frac{\tau_x^b}{I_{xx}} + \left( \frac{I_{yy} - I_{zz}}{I_{xx}} \right) \omega_y^b \omega_z^b, \\ \dot{\omega}_y^b &= \frac{\tau_y^b}{I_{yy}} + \left( \frac{I_{zz} - I_{xx}}{I_{yy}} \right) \omega_z^b \omega_x^b, \\ \dot{\omega}_z^b &= \frac{\tau_z^b}{I_{zz}} + \left( \frac{I_{xx} - I_{yy}}{I_{zz}} \right) \omega_x^b \omega_y^b. \end{aligned} \quad (7-19)$$

Here  $\omega^b$  and  $\dot{\omega}^b$  are the angular velocity and the angular acceleration at a specified axis, respectively.

### 7.2.2 The Gear Predictor-Corrector Algorithm

In the Hamiltonian formulations, the set of ordinary differential equations (7-7), (7-18), and (7-19) can be conveniently integrated by means of the Gear predictor-

corrector algorithm [155] to obtain the trajectories of the molecules. For each molecule we have to solve ten equations. All the equations are mathematically very similar. So we will illustrate the method using the position coordinate  $r_i$  for a molecule  $i$ . See the Ref. [143] for further discussion of this method. Suppose that molecular positions, velocities, accelerations, etc., at a certain time  $t$  are given. Then we can predict those values at time  $t + \delta t$  by Taylor expansion about time  $t$  as follows:

$$\begin{aligned} r_i^p(t + \delta t) &= r_i(t) + \delta t v_i(t) + \frac{1}{2} \delta t^2 a_i(t) + \dots, \\ v_i^p(t + \delta t) &= v_i(t) + \delta t a_i(t) + \dots, \\ a_i^p(t + \delta t) &= a_i(t) + \dots. \end{aligned} \tag{7-20}$$

Knowing the predicted values of  $r_i^p$  enables one to calculate the force at time  $t + \delta t$  from Eq. (7-8), which can be used to calculate the correct acceleration  $a_i^c$ . Then the error in the acceleration is

$$\Delta a_i = a_i^c(t + \delta t) - a_i^p(t + \delta t). \tag{7-21}$$

This can be used to correct the other quantities thus:

$$\begin{aligned} r_i^c(t + \delta t) &= r_i^p(t + \delta t) + c_0 \Delta a_i, \\ v_i^c(t + \delta t) &= v_i^p(t + \delta t) + c_1 \Delta a_i, \\ a_i^c(t + \delta t) &= a_i^p(t + \delta t) + c_2 \Delta a_i. \end{aligned} \tag{7-22}$$

Here  $c_0$ ,  $c_1$ , and  $c_2$  are the Gear coefficients given in the literatures [143,155]. Similar equations may be written down for the components of the angular velocities and quaternions, replaced the force by the torque. In this simulation, the second-order

differential equations of translational motion for the c.m. are solved by a 4-value Gear method and the first-order differential equations of rotational motion for body-fixed angular velocities and quaternions by a 5-value Gear method. Conservation of momentum and energy is extremely useful for checks of the numerical results. For the molecular positions, the periodic boundary conditions (PBC) and the minimum image convention were utilized in the usual way [143].

### 7.2.3 The Initial Conditions

At the start of the simulation, the initial values of the following quantities must be given for each molecule. These may be chosen to be the initial positions and velocities of the c.m., the initial orientations, and the angular velocities of each molecule. The initial linear and angular velocity components can be assigned randomly from the Maxwell-Boltzmann distribution at the given temperature  $T$ . For example, for the x-components one has

$$p(v_x)dv_x = \left( \frac{m}{2\pi k_B T} \right)^{\frac{1}{2}} e^{-mv_x^2/2k_B T} dv_x. \quad (7-23)$$

As usual, the total linear momentum and the total angular momentum must be chosen to be zero initially. They should be monitored during the simulation to ensure that they stay zero at all times.

It is customary to put the particles in a closed-packed configuration initially. To have an integral number of unit cells and to be able to satisfy periodic boundary conditions, it is then necessary to choose the simulation box with a cube of lattice constant

$a$  for simplicity. In our calculation, the starting configurations were a fcc lattice with a density chosen to be approximately  $0.998 \text{ g/cm}^3$  at  $273.15 \text{ K}$  and  $1 \text{ atm}$ . With this, the initial positions of the c.m.'s of the molecules are given by

$$\mathbf{r}_i = \frac{\sum_{a=1}^{n_a} m_a \mathbf{r}_{ia}}{M}. \quad (7-24)$$

The initial orientations of the particle, determined by the angles  $\phi, \theta, \psi$ , may be given from Eq. (7-14) using a random number in the range  $0 \leq \phi, \theta, \psi \leq 2\pi$ .

The initial values of the linear and the angular accelerations may be found from the initial values of the forces and the torques, which themselves may be found from the initial positions and orientations. The initial velocities of the higher derivatives, if needed, may be taken to be zero. A set of reduced units [143], based on the energy and length parameters  $\varepsilon_{00}$  and  $\sigma_{00}$ , is used throughout in this MD simulation and denoted by an asterisk.

#### 7.2.4 Thermodynamic Quantities of Interest

The instantaneous potential energy  $\mathcal{U}$  and kinetic energy  $\mathcal{K}$  can be calculated from Eqs. (7-5) and (7-6), respectively, and then the total energy is, of course,

$$E = \mathcal{K} + \mathcal{U}. \quad (7-25)$$

The ensemble averages are obtained by averaging over a suitable number of time steps after the system has reached equilibrium.

The instantaneous temperature  $\mathcal{T}$  at any given time  $t$  can be defined by

$$\mathcal{T} = \frac{2\mathcal{K}}{3Nk_B}. \quad (7-26)$$

For a molecular system, one needs both the rotational and the translational temperatures. Therefore, it is necessary to scale the linear velocities and the angular velocities by themselves. These individual instantaneous temperatures may be defined in the same way.

The instantaneous pressure  $\mathcal{P}$  may be defined from the virial theorem [143]. We get

$$\mathcal{P} = \rho k_B \mathcal{T} + \frac{\mathcal{W}}{V}, \quad (7-27)$$

where  $\rho$  is the density and  $V$  is the volume of the system.  $\mathcal{W}$  is the internal virial, which is defined by

$$\mathcal{W} = \frac{1}{3} \sum_i \mathbf{r}_i \cdot \mathbf{F}_i = \frac{1}{3} \sum_i \sum_{j>i} \mathbf{r}_{ij} \cdot \mathbf{F}_{ij}, \quad (7-28)$$

where  $\mathbf{r}_{ij} = \mathbf{r}_i - \mathbf{r}_j$  represents the vector between the molecular centers and  $\mathbf{F}_{ij}$  is the force acting on  $i$  due to  $j$ . Using the definition of the pair virial function [143] for a molecular system,

$$w(\mathbf{r}_{ij}) = \sum_a \sum_b \frac{w(\mathbf{r}_{ab})}{r_{ab}^2} (\mathbf{r}_{ab} \cdot \mathbf{r}_{ij}), \quad (7-29)$$

where  $w(\mathbf{r}_{ab}) = -\mathbf{r}_{ab} \cdot \mathbf{F}_{ab}$ , the equation (7-28) can be written in the form

$$\mathcal{W} = -\frac{1}{3} \sum_i \sum_{j>i} w(\mathbf{r}_{ij}). \quad (7-30)$$

It should be noted that in contrast with the case of a spherically symmetric potential, the expression for the virial cannot be simplified further here.

To monitor the system equilibrium, one can record the instantaneous values of energies and temperature or calculate the translational and the rotational order parameter.

At the end of the equilibration phase both of these order parameters should fluctuate around zero with amplitude  $O(N^{-1/2})$ .

The NVE MD simulations were carried out on the system of 108 water molecules interacting with the GWR pair potential, whose interactions were truncated at a value of  $r_c$  approximately equal to half the length  $L$  of the cubic cell. The long-range corrections ( $r > r_c$ ) for energies and pressure were calculated by integration over  $r_c$ , assuming a unit pair radial distribution function. However, we found the values of correction to be very small, nearly zero, so we ignored them in this simulation.

The computer simulation on the GWR potential was carried out using the much less intensive NVE MD method, realizing of course that, though the pressure changes contain similar information as the volume changes in an NPT MD, the pressure is extremely sensitive to the input parameters.

### 7.3 Results and Discussion

An equilibration phase of 15000 time steps was required to "melt" the lattice in an NVE run with intermittent temperature scaling to a high temperature. A consecutive run of another 10000 time steps was needed to get average thermodynamic quantities. The time-step size in the NVE simulations is  $\delta t = 0.5$  fs and the total run duration is then 5 ps for 10000 time steps. After the first NVE run at a given temperature, the next simulations were continued using the previous configurations by decreasing temperature. The results of such simulations were found to be independent of the starting configurations.

The trajectories generated by each simulation have been used to calculate static properties at each temperature. These properties were determined by averaging over 10000 time steps. The atom-atom radial distribution functions (RDFs) are given in Figure 7.12. In these figures, the curves obtained from the NVE MD simulation at 298 K are compared together with the results from the neutron scattering experiments of Soper and Phillips [156]. As can be seen, the qualitative agreement with the experiment results is strikingly good except the first peak of  $g_{\text{OO}}$  and  $g_{\text{OH}}$  functions. The structural properties are quite well defined at the broad first minimum around 3.4 Å which represents the dense second-neighbor distance as characteristic for liquid water. It is certain that more optimization of the GWR potential can give rise to improve the overall RDFs.

The pressure  $P$  as a function of temperature  $T$  is plotted in Figure 7.13. The result shows to get a pressure minimum around 250 K even though the standard deviations among the simulations are too large. This is mainly because the GWR potential function is much stiffer than the SPC/E potential, causing high fluctuation force and virial functions. From these calculations, a pressure minimum has been obtained, but longer run times are required to ensure that equilibrium has been established in these computationally intensive runs.

The final optimization of the potential parameters will of course rely on the full MD, with assessment of the crystal structures and the liquid-state radial distribution function, energy, and density (or pressure). This fully optimized potential should be sufficiently simple to be used as it stands in biological studies. It will be also required to obtain realistic temperature and pressure effects, such as the density maximum. Before

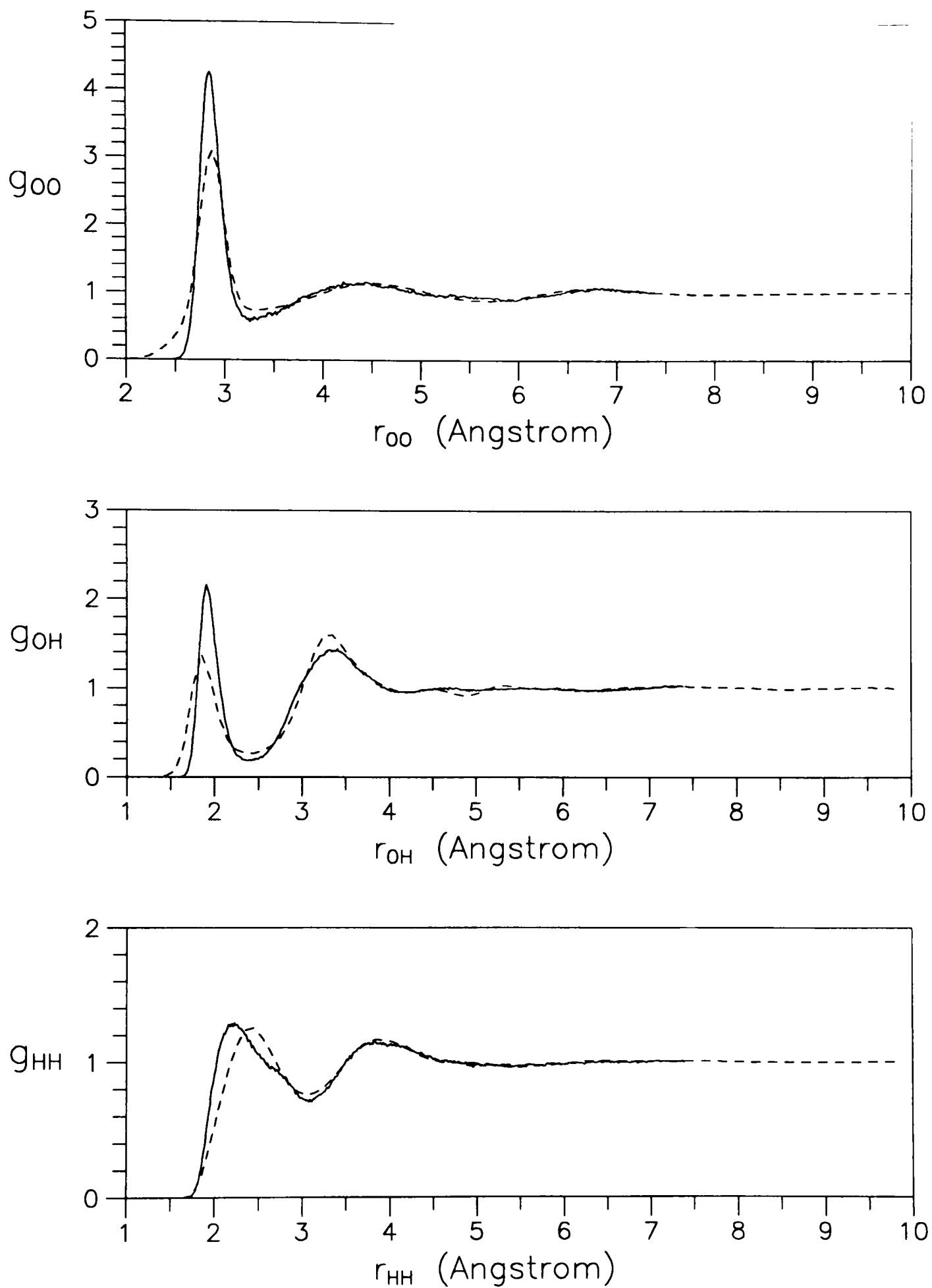


Figure 7.12. The radial distribution functions of liquid water at 298 K. The solid line is obtained from the present simulation and the dashed line from the neutron scattering experiments [156].

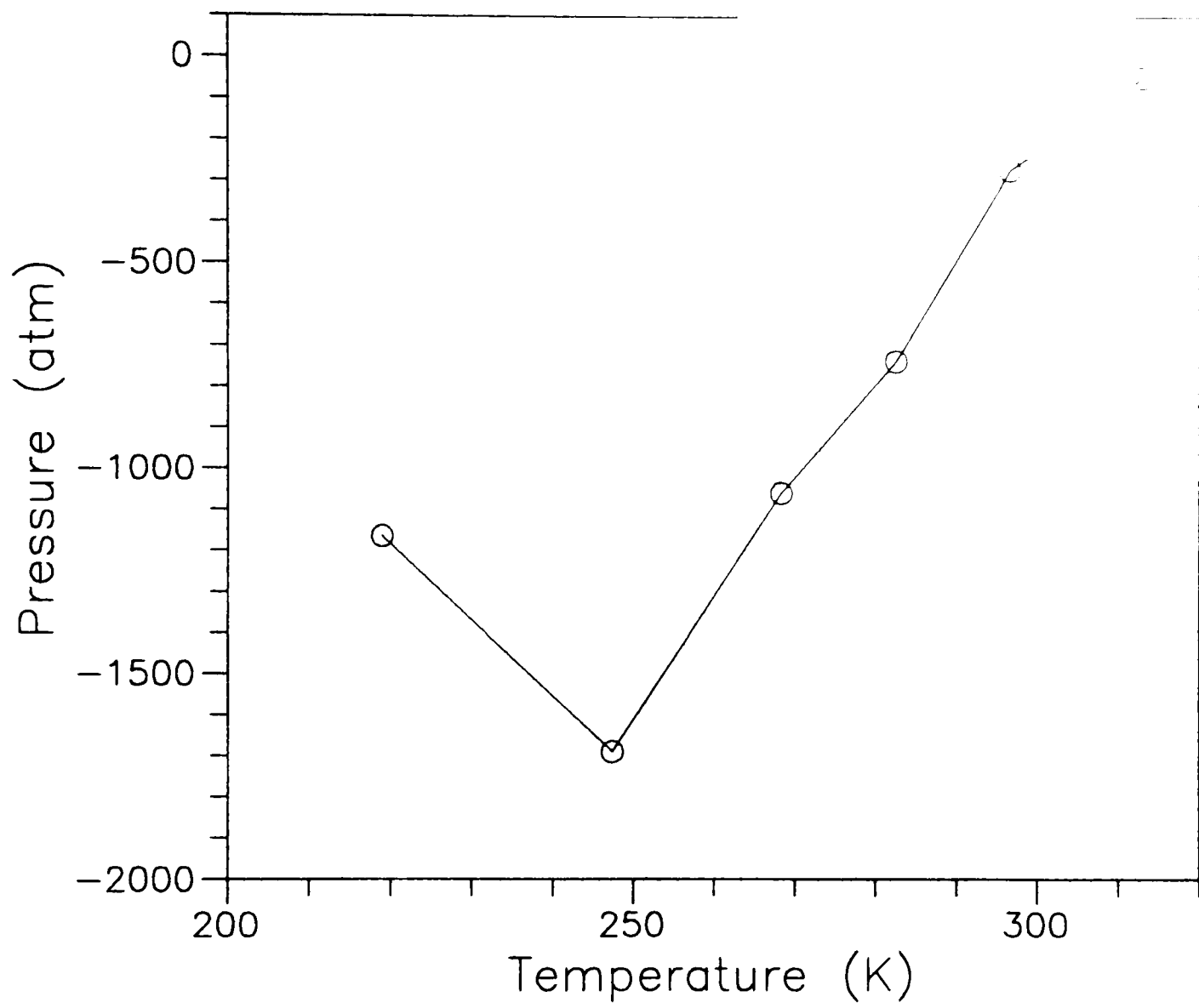


Figure 7.13. The pressure variation as a function of temperature  $T$ .

completing too much work on surfaces and biological systems, further optimization on the proposed simple potential should be carried out and dielectric effects should be added. Following this, many prototypical surfaces in biology, chemistry and physics [1], such as metallic and so-called “hydrophobic” or “hydrophilic” surfaces, can be investigated.

A direct determination of the density at constant pressure and temperature requires use of NPT ensemble methods in MD simulations developed by Evans and Morris [151,152]. However, it is not easy to find the Lagrange multipliers  $\xi$  and  $\lambda$  from the constraint NPT method using the proposed angular dependent potential. This problem together with the designing of the codes for massively parallel processing (MPP) to an NVE and an NPT MD simulations is being studied in our laboratory.

## REFERENCES

- [1] F. Franks, in *Water. A Comprehensive Treatise*, Vol. 2, ed. F. Franks (Plenum Press: New York, 1973), Chapter 1.
- [2] D. Eisenberg and W. Kauzmann, *The Structure and Properties of Water* (Oxford Univ. Press: Oxford, 1969).
- [3] G. W. Robinson, S.-B. Zhu, S. Singh, and M. W. Evans, *Water in Biology, Chemistry, and Physics: Experimental Overviews and Computational Methodologies* (World Scientific Publishing Co.: Singapore, 1996).
- [4] W. Drost-Hansen and J. S. Clegg, *Cell-Associated Water* (Academic Press: New York, 1979).
- [5] H. Hauser, in *Reverse Micelles*, eds. P. L. Luisi and B. E. Straub (Plenum Press: New York, 1984), pp. 37-53.
- [6] F. Franks, in *Water. A Comprehensive Treatise*, Vol. 1, ed. F. Franks (Plenum Press: New York, 1973).
- [7] M. V. Volkenshtein, *Molecules and Life; An Introduction to Molecular Biology* (Plenum Press: New York, 1970).
- [8] D. Vasilescu, J. Jaz, L. Packer and B. Pullman, *Water and Ions in Biomolecular Systems* (Birkhauser Verlag: Basel, 1990).
- [9] L. A. Moran, K. G. Scrimgeour, H. R. Horton, R. S. Ochs, and J. D. Rawn, *Biochemistry* (Neil Patterson Publishers/Prentice-Hall Inc.: Englewood Cliffs, NJ, 1994).
- [10] A. W. Adamson, *Physical Chemistry of Surfaces*, 4th ed. (Wiley-Interscience: New York, 1982).
- [11] T. G. Fillingim, S.-B. Zhu, S. Yao, J. Lee, and G. W. Robinson, *Chem. Phys. Lett.* **161**, 444 (1989).
- [12] P. M. Wiggins, *Microbiol. Rev.* **54**, 432 (1990).
- [13] A. Rahman and F. H. Stillinger, *J. Chem. Phys.* **55**, 3336 (1971).
- [14] P. J. Rossky and S. H. Lee, *Chemica Scripta* **29A**, 93 (1989).

- [15] S.-B. Zhu and G. W. Robinson, *J. Chem. Phys.* **94**, 1403 (1991).
- [16] J. J. Magda, M. Tirrell, and H. T. David, *J. Chem. Phys.* **83**, 1888 (1985).
- [17] M. Matsumoto and Y. Kataoka, *J. Chem. Phys.* **88**, 3233 (1988).
- [18] M. A. Wilson, A. Pohorille, and L. R. Pratt, *J. Chem. Phys.* **88**, 3281 (1988).
- [19] O. A. Karim and A. D. Haymet, *J. Chem. Phys.* **89**, 6889 (1988).
- [20] S.-B. Zhu, T. G. Fillingim, and G. W. Robinson, *J. Phys. Chem.* **95**, 1002 (1991).
- [21] G. N. Patey and G. M. Torrie, *Chemica Scripta* **29A**, 39 (1989).
- [22] S.-B. Zhu and G. W. Robinson, *J. Chem. Phys.* **97**, 4336 (1992).
- [23] C. Y. Lee, J. A. McCammon, and P. J. Rossky, *J. Chem. Phys.* **80**, 4448 (1984).
- [24] S.-B. Zhu, J.-B. Zhu, and G. W. Robinson, *Phys. Rev. A* **44**, 2602 (1991).
- [25] J. A. McCammon and S. C. Harvey, *Dynamics of Proteins and Nucleic acids* (Cambridge University Press: Cambridge, 1987).
- [26] K. J. Packer, in *Progress in Nuclear Magnetic Resonance Spectroscopy*, Vol. 3, eds. J. W. Emsley, J. Feeney, and L. H. Sutcliffe (Pergamon: Oxford, 1967), pp. 87-129.
- [27] H. A. Resing, *Adv. Mol. Relaxation Processes* **3**, 199 (1972).
- [28] J. E. Hansen, E. Pines, and G. R. Fleming, *J. Phys. Chem.* **96**, 6904 (1992).
- [29] H. Savage and A. Wlodawer, *Methods in Enzymology* **127**, 162 (1986).
- [30] E. Westhof, *Ann. Rev. Biophys. Biochem.* **17**, 125 (1988).
- [31] C. H. Cho, M. Chung, J. Lee, T. Nguyen, S. Singh, M. Vedamuthu, S. Yao, J.-B. Zhu, and G. W. Robinson, *J. Phys. Chem.* **99**, 7806 (1995).
- [32] Y. R. Shen, *J. Vac. Sci. Technol. B* **3**, 1464 (1985).
- [33] X. Shi, E. Borguet, A. Tarnovsky, and K. B. Eisenthal, *Chem. Phys.* **205**, 1074 (1996).
- [34] H.-F. Eicke and J. Rehak, *J. Helv. Chim. Acta.* **59**, 2883 (1976).
- [35] A. Maitra, *J. Phys. Chem.* **88**, 5122 (1984).

- [36] M. Kotlarchyk, J. S. Huang, and S.-H. Chen, *J. Phys. Chem.* **89**, 4382 (1985).
- [37] S.-H. Chen and R. Rajagopalan, *Micellar Solutions and Microemulsions* (Springer-Verlag: New York, 1990), pp. 227-249.
- [38] S. H. Chen, S. L. Chang, R. Strey, and P. Thiyagarajan, *J. Phys.: Condens. Matter* **3**, F91 (1991).
- [39] D. Langevin, In *Reverse Micelles*, eds. P. L. Luisi and B. E. Straub (Plenum Press: New York, 1989), pp. 287-303.
- [40] M. P. Pileni, T. Zemb, and C. Petit, *Chem. Phys. Lett.* **118**, 414 (1985).
- [41] N. J. Bridge and P. D. I. Fletcher, *J. Chem. Soc. Faraday Trans. 1* **79**, 2161 (1983).
- [42] M. Wong, J. K. Thomas, and M. Grätzel, *J. Am. Chem. Soc.* **98**, 2391 (1976).
- [43] T. K. Jain, M. Varshney, and A. Maitra, *J. Phys. Chem.* **93**, 7409 (1989).
- [44] E. G. Finer, *J. Chem. Soc., Faraday Trans. II* **69**, 1590 (1973).
- [45] E. G. Finer and A. Darke, *Chem. Phys. Lipids* **12**, 1 (1974).
- [46] D. V. O'Connor and D. Phillips, *Time-Correlated Single Photon Counting* (Academic Press: London, 1984).
- [47] G. W. Robinson, *J. Phys. Chem.* **95**, 10386 (1991).
- [48] T. G. Fillingim, N. Luo, J. Lee, and G. W. Robinson, *J. Phys. Chem.* **94**, 6368 (1990).
- [49] W. A. Tucker and L. H. Nelken, in *Handbook of Chemical Property Estimation Methods*, eds. W. J. Lyman, W. F. Reehl, and D. H. Rosenblatt, (American Chemical Society: Washington, DC, 1990), Chapter 17.
- [50] A. Einstein, *Investigations on the Theory of the Brownian Movement* (Dover: New York, 1956), p.17.
- [51] G. W. Robinson, R. J. Robbins, G. R. Fleming, J. M. Morris, A. E. W. Knight, and R. J. S. Morrison, *J. Am. Chem. Soc.* **100**, 7145 (1978).
- [52] R. A. Moore, J. Lee, and G. W. Robinson, *J. Phys. Chem.* **89**, 3658 (1985).
- [53] E. Pines and G. R. Fleming, *J. Phys. Chem.* **95**, 10448 (1991).

- [54] J. Lee, G. W. Robinson, S. P. Webb, L. A. Philips and J. H. Clark, *J. Am. Chem. Soc.* **108**, 6538 (1986).
- [55] J. Lee, *J. Phys. Chem.* **94**, 258 (1990).
- [56] J. Lee, N. Luo, and G. W. Robinson, Unpublished work.
- [57] G. Weber and D. J. R. Laurence, *Biochem. J.* **56**, 31 (1954).
- [58] L. Brand and J. R. Gohlke, *Annu. Rev. Biochem.* **41**, 843 (1972).
- [59] J. Lee and G. W. Robinson, *J. Am. Chem. Soc.* **107**, 6153 (1985).
- [60] G. W. Robinson, P. J. Thistlethwaite, and J. Lee, *J. Phys. Chem.* **90**, 4224 (1986).
- [61] E. J. Hart and M. Anbar, *The Hydrated Electron* (Wiley-Interscience: New York, 1970).
- [62] J. Hermans, *Molecular Dynamics and Protein Structure* (Polycrystal Book Service: Western Springs, IL, 1985).
- [63] D. L. Beveridge and W. L. Jorgensen, *Ann. N. Y. Acad. Sci.* **482**, 147 (1986).
- [64] W. F. van Gunsteren and P. K. Weiner, *Computer Simulation of Biomolecular Systems* (ESCOM: Leiden, 1989).
- [65] S.-B. Zhu, S. Singh, and G. W. Robinson, *Adv. Chem. Phys.* **85**, 627 (1994).
- [66] W. A. P. Luck, In *Intermolecular Forces*, eds. P. L. Huyskens, W. A. P. Luck, and T. Zeegers-Huyskens (Springer-Verlag: Berlin Heidelberg, 1991), Chapter IX.
- [67] M.-P. Bassez, J. Lee, and G. W. Robinson, *J. Phys. Chem.* **91**, 5818 (1987).
- [68] Y. Maréchal, In *Hydrogen Bond Networks*, NATO ASI Series, C435, eds M. C. Bellisent-Funel and J. Dore (Kluwer: Dordrecht, 1994).
- [69] J. Jonas and A. Jonas, *Annu. Rev. Biophys. Biomol. Structure* **23**, 287 (1994).
- [70] H. J. C. Berendsen, *Natuurkd. Voordr.* **59**, 85 (1981).
- [71] M. C. Gutzwiller, letter to the editor, *Physics Today* **48**, 15 (1995).
- [72] M. Vedamuthu, S. Singh, and G. W. Robinson, *J. Phys. Chem.* **98**, 2222 (1994).

- [73] M. Vedamuthu, S. Singh, and G. W. Robinson, *J. Phys. Chem.* **98**, 8591 (1994).
- [74] M. Vedamuthu, S. Singh, and G. W. Robinson, *J. Phys. Chem.* **99**, 9263 (1995).
- [75] W. C. Röntgen, *Ann. Phys. u. Chem.* **45**, 91 (1892).
- [76] J. D. Bernal and R. H. Fowler, *J. Chem. Phys.* **1**, 515 (1933).
- [77] B. Kamb, in *Structural Chemistry and Molecular Biology*, eds. A. Rich and N. Davidson (W. H. Freeman and Co.: San Francisco, 1968), pp. 507-542.
- [78] S. R. Billeter, P. M. King and W. F. van Gunsteren, *J. Chem. Phys.* **100**, 6692 (1994).
- [79] A. Wallqvist and P.-O. Åstrand, *J. Chem. Phys.* **102**, 6559 (1995).
- [80] A. G. Kalinichev and K. Heinzinger, in *Thermodynamic Data*, ed. S. Saxena (Springer: New York, 1992), Chapter 1.
- [81] M. D. Morse and S. A. Rice, *J. Chem. Phys.* **76**, 650 (1982).
- [82] J. R. Reimers, R. O. Watts, and M. L. Klein, *Chem. Phys.* **64**, 95 (1982).
- [83] S.-B. Zhu and G. W. Robinson, *Proc. Internat. Supercomputing Inst.* **I**, 300 (1988).
- [84] J. S. Rowlinson, *Trans. Faraday Soc.* **47**, 120 (1951).
- [85] P. Cieplak, P. Kollman, and T. P. Lybrand, *J. Chem. Phys.* **92**, 6755 (1990).
- [86] G. D'Arrigo, G. Maisano, F. Mallamace, P. Migliardo, and F. Wanderlingh, *J. Chem. Phys.* **75**, 4264 (1981).
- [87] G. S. Kell, *J. Chem. Eng. Data* **20**, 97 (1975).
- [88] G. S. Kell, *J. Chem. Eng. Data* **12**, 66 (1967).
- [89] M. Goldblatt, *J. Phys. Chem.* **68**, 147 (1964).
- [90] M. Vedamuthu, S. Singh, and G. W. Robinson, *J. Phys. Chem.* in the press.
- [91] T. DeFries and J. Jonas, *J. Chem. Phys.* **66**, 5393 (1977).
- [92] L. Bosio, S.-H. Chen and J. Teixeira, *Phys. Rev. A* **27**, 1468 (1983).
- [93] S.-H. Chen and J. Teixeira, *Adv. Chem. Phys.* **64**, 1 (1986).

- [94] See Table 3.4 in Ref. [2].
- [95] M.-C. Bellissent-Funel and L. Bosio, *J. Chem. Phys.* **102**, 3727 (1995).
- [96] C. H. Cho, S. Singh, and G. W. Robinson, *Phys. Rev. Lett.* **76**, 1651 (1996).
- [97] C. H. Cho, S. Singh, and G. W. Robinson, *Faraday Discuss.* **103**, 19 (1996).
- [98] W. R. Ware, In *Creation and Detection of the Excited State*, ed. A. Lamolla (Dekker: New York, 1971).
- [99] V. J. Koester and R. M. Dowben, *Rev. Sci. Instrum.* **49**, 1186 (1978).
- [100] D. Beelaar, *Rev. Sci. Instrum.* **57**, 1116 (1986).
- [101] H. Kume, K. Koyama, K. Nakatsugawa, S. Suzuki, and D. Fallowitz, *Appl. Opt.* **27**, 1170 (1988).
- [102] S. Cova, A. Lacaita, M. Ghioni, G. Ripamonti, and T. A. Louis, *Rev. Sci. Instrum.* **60**, 1104 (1986).
- [103] F. P. Schäfer, *Dye Lasers* (Springer-Verlag: New York, 1990).
- [104] P. K. Das and C. M. DeCusatis, *Acousto-optic Signal Processing: Fundamentals & Applications* (Artech House: Boston, 1991).
- [105] T. Murao, I. Yamazaki, and K. Yoshihara, *Appl. Opt.* **21**, 2297 (1982).
- [106] I. Yamazaki, N. Tamai, H. Kume, H. Tsuchiya, and K. Oba, *Rev. Sci. Instrum.* **56**, 1187 (1985).
- [107] D. Beelaar, *Rev. Sci. Instrum.* **57**, 1686 (1986).
- [108] D. R. James, D. R. M. Demmer, R. E. Verrall, and R. P. Steer, *Rev. Sci. Instrum.* **54**, 1121 (1983).
- [109] G. R. Haugen, B. W. Wallin, and F. E. Lytle, *Rev. Sci. Instrum.* **50**, 64 (1979).
- [110] A. Grinvald and I. Z. Steinberg, *Anal. Biochem.* **59**, 583 (1974).
- [111] Z. S. Kolber and M. D. Barkley, *Anal. Biochem.* **152**, 6 (1986).
- [112] A. Gafni, R. L. Modlin, and L. Brand, *Biophys. J.* **15**, 263 (1975).

- [113] P. R. Bevington, *Data Reduction and Error Analysis for the Physical Sciences* (McGraw-Hill: New York, 1969).
- [114] A. Grinvald, E. Haas, and I. Z. Steinberg, *Proc. Natl. Acad. Sci. USA* **69**, 2273 (1972).
- [115] A. Grinvald, *Anal. Biochem.* **75**, 260 (1976).
- [116] D. V. O'conner and J. C. Andre, *J. Phys. Chem.* **83**, 1333 (1979).
- [117] W. R. Ware, M. Pratinidhi, and R. K. Bauer, *Rev. Sci. Instrum.* **54**, 1148 (1983).
- [118] L. J. Cline Love and L. A. Shaver, *Anal. Chem.* **48**, 364A (1976).
- [119] E. M. Kosower and H. Kanety, *J. Am. Chem. Soc.* **105**, 6236 (1983).
- [120] K. L. Rowlen, *J. Photochem, Photobio. A: Chem.* **64**, 81 (1992).
- [121] H. -F. Eicke and P. Kvita, in *Reverse Micelles*, eds. P. L. Luisi and B. E. Straub (Plenum Press: New York, 1984), pp. 21-35.
- [122] P. Stenius, in *Reverse Micelles*, eds. P. L. Luisi and B. E. Straub (Plenum Press: New York, 1984), pp. 1-19.
- [123] L. Stryler, *J. Mol. Biol.* **13**, 482 (1965).
- [124] P. J. Sadkowski and G. R. Fleming, *Chem. Phys.* **54**, 79 (1980).
- [125] G. R. Fleming, G. Porter, R. J. Robbins, and J. A. Synowiec, *Chem. Phys. Lett.* **52**, 228 (1977).
- [126] J. E. Enderby, *J. Phys.: Condens. Matter* **3**, F88 (1991).
- [127] D. Toptygin, J. Svobodova, I. Konopasek, and L. Brand, *J. Chem. Phys.* **96**, 7919 (1992).
- [128] D. R. James and W. R. Ware, *Chem. Phys. Lett.* **120**, 455 (1985).
- [129] D. Brown and J. H. R. Clarke, *J. Phys. Chem.* **92**, 2881 (1988).
- [130] A. G. Szabo, *SPIE*, 909, 2 (1988).
- [131] J. Lee, and G. W. Robinson, *J. Phys. Chem.* **89**, 1872(1985).

- [132] R. A. Auerbach, J. A. Synowiec, and G. W. Robinson, in *Picosecond Phenomena*, Springer Series in Chemical Physics, Vol. 4, eds. C. V. Shank, E. P. Ippen, and S. L. Shapiro (Springer: New York, 1978).
- [133] M. Zulauf and H.-F. Eicke, *J. Phys. Chem.* **83**, 480 (1979).
- [134] E. Parzen, *Modern Probability Theory and Its Applications* (Wiley: New York, 1960).
- [135] L. Takacs, *Stochastic Processes: Problems and Solutions* (Methuen: London, 1960).
- [136] J. O. Hirschfelder, C. F. Curtiss, and R. B. Bird, *Molecular Theory of Gases and Liquids* (John Wiley & Sons, Inc.: New York, 1954), pp. 8-13.
- [137] Q. Du, R. Superfine, E. Freysz, and Y. R. Shen, *Phys. Rev. Lett.* **70**, 2313 (1993).
- [138] B. Yang, D. E. Sullivan, B. Tjipto-Margo, and C. G. Gray, *J. Phys.: Condens. Matter* **3**, F109 (1991).
- [139] H. Takahashi, *Proc. Phys.-Math. Soc. Japan* **24**, 60 (1942).
- [140] L. Tonks, *Phys. Rev.* **50**, 955 (1936).
- [141] E. H. Lieb and D. C. Mattis, *Mathematical Physics in One Dimension* (Academic: New York, 1966).
- [142] R. K. Pathria, *Statistical Mechanics* (Pergamon: Oxford, 1980).
- [143] M. P. Allen and D. J. Tildesley, *Computer Simulation of Liquids* (Oxford University Press: Oxford, 1990).
- [144] K. Huang, *Statistical Mechanics* (Wiley: New York, 1987).
- [145] M. Abramowitz and I. A. Stegun, *Handbook of Mathematical Functions* (Dover Publications, Inc.: New York, 1970).
- [146] H. Kanno and C. A. Angell, *J. Chem. Phys.* **73**, 1940 (1980).
- [147] H. J. C. Berendsen, J. R. Grigera and T. P. Straatsma, *J. Phys. Chem.* **91**, 6269 (1987).
- [148] S. S. Xantheas and T. H. Dunning, Jr., *J. Chem. Phys.* **98**, 8037 (1993).

- [149] N. Metropolis, A. W. Rosenbluth, M. N. Rosenbluth, A. H. Teller, and E. Teller, *J. Chem. Phys.* **21**, 1087 (1953).
- [150] H. C. Andersen, *J. Chem. Phys.* **72**, 2384 (1980).
- [151] D. J. Evans and G. P. Morriss, *Chem. Phys.* **77**, 63 (1983).
- [152] D. J. Evans and G. P. Morriss, *Phys. Lett.* **98A**, 433 (1983).
- [153] D. J. Evans, *Mol. Phys.* **34**, 317 (1977).
- [154] H. Goldstein, *Classical Mechanics*, 2nd ed. (Addison-Wesley: Reading, MA, 1980).
- [155] C. W. Gear, *Numerical Initial Value Problems in Ordinary Differential Equations* (Prentice-Hall: Englewood Cliffs, N.J., 1971).
- [156] A. K. Soper and M. G. Phillips, *Chem. Phys.* **107**, 47 (1986).